Sensor Fusion in Autonomous Navigation for Asteroid Observation Missions

M. N. van Oorschot

Master of Science Thesis

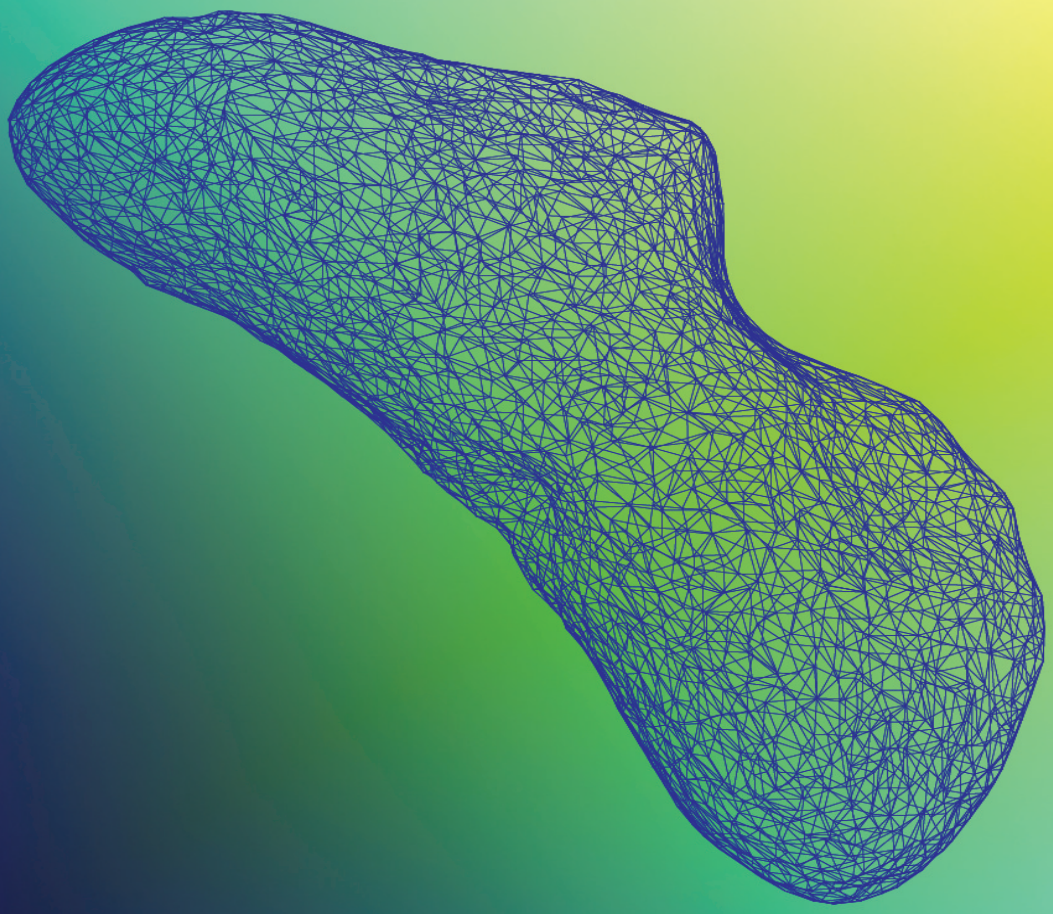

TU Delft Delft University of Technology

Delft Center for Systems and Control

Sensor Fusion in Autonomous Navigation for Asteroid Observation Missions

by

M. N. van Oorschot

For the degrees of Master of Science in Systems and Control, and Aerospace Engineering
at the Delft University of Technology,
to be defended publicly on Thursday June 30, 2022 at 09:30 AM.

Student number:	4439279	
Project duration:	June 23, 2021 – June 30, 2022	
Thesis committee:	Dr. ir. drs. M. Kok	Supervisor
	Dr. ir. B.C. Root	Supervisor
	Dr.ir. E. Mooij	Chair

Faculty of Mechanical, Maritime and Materials Engineering (3mE) & Aerospace Engineering (AE) · Delft University of Technology

Abstract

Spacecraft navigation and control is difficult in deep space operations. Especially around asteroids, the irregular gravity field increases the difficulty of estimating the spacecraft trajectory. Autonomous navigation can increase the safety and accuracy for orbit proximity operations. Furthermore, it eliminates the need for continuous communication with the spacecraft. For the implementation of autonomous navigation in deep space, the onboard guidance navigation & control (GNC) should be able to accurately estimate the attitude and relative position of the spacecraft. By using sensor fusion, information from individual sensors can be combined to increase certainty and accuracy of the state estimation. A sensor fusion model is proposed, comprising an inertial measurement unit (IMU), star tracker and light detection and ranging (LiDAR) as navigation sensors. The aim of this research is to investigate the feasibility and performance applying sensor fusion for the spacecraft state estimation.

A navigation filter is applied to a benchmark scenario that orbits an asteroid at 50 km. In this scenario, asteroid 433 Eros has been selected for its unique shape, which has been mapped during the Near Earth Asteroid Rendezvous (NEAR) mission. A simulation is performed to approximate the dynamics and kinematics of the mission environment. The simulation takes a polyhedron model of the asteroid, a third-body disturbance by the sun, and an additional acceleration due to solar radiation pressure into account. The simulation forms a base for the sensor measurement simulation. As the IMU consists of an accelerometer and a gyroscope, the measurements total to two sets of available data for position as well as attitude estimation. The navigation filter estimates the position, velocity, attitude and gravitational constant of the asteroid, by use of an extended Kalman filter (EKF). The EKF is augmented for the quaternion states to a multiplicative extended Kalman filter. The navigation filter is simulated for a benchmark scenario, as well as for different orbital heights and temporary loss of the star tracker as well as the LiDAR sensor.

As a result, it is concluded that it is feasible with the given sensor set to approximate the position and attitude of a spacecraft in proximity of 433 Eros. For the position, a root-mean-square error (RMSE) of 0.5 m is found at an orbital height of 50 km. Using a time step of 0.1 s for the EKF is recommended after a trade-off between accuracy and computational time. It is concluded that the proposed model for state estimation is sufficiently accurate for position and attitude estimation for the given benchmark scenario. With this navigation filter, we come one step closer to the development of autonomous navigation for asteroid observing spacecraft.

Contents

List of Figures

List of Tables

Glossary

List of Acronyms

IMU	inertial measurement unit
NEAR	Near Earth Asteroid Rendezvous
DSN	deep space network
GNC	guidance navigation & control
LiDAR	light detection and ranging
EKF	extended Kalman filter
MEKF	multiplicative extended Kalman filter
ToF	time-of-flight
NEO	near-Earth objects
MSI	multi-spectral imager
SRP	solar radiation pressure
SLAM	simultaneous localization and mapping
KF	Kalman filter
UKF	unscented Kalman filter
GRS	gamma Ray Spectrometer
PHO	potentially hazardous object
DCM	direction cosine matrix
MMOI	mass moment of inertia
NEA	near Earth asteroid
RMSE	root-mean-square error

List of Symbols

Latin Symbols

$\mathbf{I}$	Mass moment of inertia	kgm^2
$\mathbf{a}$	acceleration vector	m/s^2
$\mathbf{F}$	Force	N
$\mathbf{r}$	position vector	m
$\mathbf{v}$	velocity vector	m/s
d	distance	m
I	Inertia	
m	body mass	kg
m	mass	kg
P	Spacecraft body	
t	time	s
x	Length in x-direction	m
y	Length in y-direction	m
z	Length in z-direction	m

Math Symbols

$\delta\mathbf{q}_{B/I}$	error quaternion	
$\delta\mathbf{z}_{k+1}$	Innovation sequence	
Δt	Time step	s
$\mathbf{\Phi}$	Measurement noise covariance matrix	
$\mathbf{\Theta}_{B/I}$	quaternion error vector	
$\mathbf{a}$	acceleration vector	m/s^2
$\mathbf{F}$	Linearised state function	
$\mathbf{f}()$	State function	
$\mathbf{G}$	Noise transition matrix	
$\mathbf{H}$	Linearised Measurement function	
$\mathbf{h}()$	Measurement function	
$\mathbf{K}$	Kalman gain	
$\mathbf{P}$	Covariance matrix	
$\mathbf{Q}$	Process noise covariance matrix	
$\mathbf{r}$	position vector	m
$\mathbf{u}$	input vector	
$\mathbf{v}$	velocity vector	m/s
$\mathbf{v}_k$	Measurement noise vector	
$\mathbf{w}$	process noise vector	
$\mathbf{X}$	State vector	
$\mathbf{x}$	State vector	

I	Identity matrix	
T	Simulation time	s

Greek Symbols

ϵ	Reflectivity	
ω	Rotation rate vector	rad/s
μ	Gravitational parameter	m^3/s^2
σ	Standard deviation	

Subscripts

0	Initial value
A	Asteroid reference frame
a	Acceleration
acc	Accelerometer
B	Spacecraft reference frame
b	Body
$gyro$	Gyroscope
I	Inertial reference frame
q	Quaternion
sp	Solar panel
x	x-direction
xx	x-axis
y	y-direction
yy	y-axis
z	z-direction
zz	z-axis
IMU	Inertial measurement unit
k	time step k
Li	LiDAR
ST	Star Tracker

Superscripts

$\hat{}$	Estimated
$\tilde{}$	Measured

Notations

ΔV	change in velocity	m/s

Preface

This document is the outcome of the research of my Master of Science graduation thesis. The graduation thesis is part of the double degree programme of the masters Aerospace Engineering and Systems & Control and is presented in a single document.

I would like to thank my supervisors Bart Root and Manon Kok for their assistance. By having you both as my supervisor, I am challenged to think more critically, and make decisions that can be validated from the perspectives of both engineering fields. I see it as best of both worlds.

Furthermore, I would like to thank Arjan Vermeulen, Willem Hoekman, and Max Koster for proofreading my chapters. You all gave a great deal of insightful feedback which I am tremendously grateful for. Having a space engineer, aerospace materials engineer and a (prospective) control engineer review my words, I could not ask for a better review group.

In addition, I would like to thank my family, who all took effort to read my introductory chapter and immersed themselves into the field of aerospace and control engineering.

Delft, University of Technology — M. N. van Oorschot
June 16, 2022

Chapter 1

Introduction

The research performed for this master thesis is centred around the application of sensor fusion within autonomous navigation of asteroid missions. This chapter will start with the discussion of the scientific relevance in Section 1-1. Next, the research question and sub-questions are introduced in Section 1-2. The novelty of the thesis research is briefly discussed in Section 1-3 Then, the overall framework of the thesis report will be explained last, in Section 1-4.

1-1 Scientific Relevance

A great deal of examples of sensor fusion are available in engineering applications: from human motion capture to underwater positioning using topographic maps, or indoor localisation using simultaneous localization and mapping (SLAM) algorithms (Miller et al. (2010),Gustafsson (2012), Bavel (2022)). Especially for positioning and orientation estimation, sensor fusion has been proven successful in obtaining accurate results. Sensor fusion is defined as combining data from sensor sources such that the resulting data can provide more information than the individual data sources (Gustafsson, 2012). By being able to combine sensor data, one should thus be able to handle data more efficiently, or gain more insight on a process. Within space exploration, sensor fusion is crucial for spacecraft autonomy, making human interpretation of trajectory information redundant.

As we are extending the possibilities for space exploration step by step, we encounter the limits of controlling the actions of a spacecraft that is at a distance of a couple of billion kilometres. Often, the deep space environment cannot be fully anticipated during mission design. The less is known about a mission target, the riskier the mission will be. An autonomous spacecraft can account for unforeseen circumstances, and enhances the probability of mission success. According to Jet Propulsion Laboratory (2019), "rather than rely on programmed commands, an [autonomous] spacecraft is aware of its surroundings at all times and capable of determining and executing safe and effective actions". Therefore, using sensor fusion for autonomous navigation in deep space can increase the amount of possible actions performed in deep space.

This is because this method can increase the reliability level of actions considered too risky before. It is therefore desired to incorporating sensor fusion into the navigation system. This should enhance the accuracy and safety of the navigation and control.

One could argue whether autonomous navigation of spacecraft is needed as there are current methods to navigate, track, and command spacecraft. Currently, communication and positioning of deep space spacecraft is performed through the deep space network (DSN). Communication is carried out through electromagnetic radiation signals. All spacecraft are equipped with a transponder to send out to and receive these signals from the Earth-based ground stations (Mudgway, 2013). Bodies naturally emitting electromagnetic radiation such as the Sun, Jupiter, or other celestial bodies can also be detected by the DSN. Where information sent through the signal is used for communication, the signal itself has the purpose of tracking.

An advantage of communication through the DSN is the access to more computational capability provided by the ground stations. On-board computers have a physical limit to their computational capacity and power supply. The ground stations on the other hand, have access to computers with a much larger computational power that can process and estimate data with large precision.

As a spacecraft orbits closer and closer to a small body, having reliable navigation plays a more crucial role. Avoiding collision is a matter of both time, by reacting in a timely manner, and of accuracy, by providing the accurate commands to change the trajectory. The objective for deep space navigation is to ensure reliable navigation, making a trade-off between accuracy and time. The latter is undeniably one of the largest disadvantages of DSN communication: a round-trip to send to and receive a signal from the ground station is at least forty minutes (Santo et al., 1995).

It is challenging to provide a command that should be performed twenty minutes from now with data that is 20 minutes old. Real-time decisions can be provided by the on-board computer, hence the motive for autonomous navigation. In addition, keeping a ground station running for command handling and tracking is expensive (Jet Propulsion Laboratory, 2014), and there is a limited communication window between the ground station and the spacecraft. It is expected that autonomous navigation comprising on-board guidance navigation & control (GNC) and availability to in-situ sensor measurements should be able to give the best performance in terms of orbit control and determination accuracy (Jet Propulsion Laboratory, 2011).

Autonomy of a spacecraft can be implemented in different mission phases and for different mission types. Autonomy in space exploration during landing has been covered in previous theses such as Woicke (2018), demonstrating the SLAM algorithms can be used to successfully avoid hazards on a landing site when performing autonomous moon landing. Indeed, autonomous landing procedures have been an important trend in autonomous spacecraft navigation. Especially missions targeting non-cooperative bodies with irregular gravity fields, such as asteroids and comets, will gain from this technology (Jonsson et al. (2007), Takahashi and Scheeres (2022)).

However, for missions targeting comets, navigation sensors such as star trackers can be lacking, as was experienced during the Rosetta mission. Due to the dust trail of comet 67P/Churyumov-Gerasimenko, the star tracker cameras were unable to estimate the orienta-

tion of the spacecraft (Pineau et al., 2019). Not only the sensor set, but also the control mechanisms are crucial for succesful autonomous operations. Sample retrieval on asteroid Itokawa was attempted during the Hayabusa mission, but could not be performed autonomously due to reaction wheel failure (Hashimoto et al., 2010). A recent attempt for autonomous landing by OSIRIS-REx was successful with a landing on 101955 Bennu in July 2020.[1]

For the implementation of autonomous navigation, proximity operations are often mentioned as mission phases that can benefit the most from it, other than surface exploration. (Nesnas et al. (2021), Chan and Agha-mohammadi (2019), Jet Propulsion Laboratory (2019), Machuca and Sánchez (2021)). In this mission phase, it is important to estimate both the orientation and the position of the vehicle. The spacecraft is approaching the target with little to no prior information about the motion or shape of the body, or with limited and changing information of its appearance (Nesnas et al., 2021). With non-cooperative objects such as asteroids with distinctive surface and shape features, it can be difficult to anticipate the dynamics around the asteroid. What's more, is that for closer orbits, more estimation accuracy and faster response is needed to avoid collisions, with respect to orbits further away. It is therefore necessary to estimate the position and estimation on-board.

Razgus (2016) demonstrated feasibility of estimating the spacecraft position and orientation orbiting Kleopatra using dual quaternions, but concluded that dual quaternions are computationally much more expensive. Irrespective of the asteroid shape, orbital height, and inclination, the conclusion was drawn that dual quaternions and quaternions have almost the same performance, even though the dual quaternion model is '40 to 50 percent more exhaustive in computational time'. Both methods were applied to an extended Kalman filter (EKF), but more filters can be used to tackle state estimation problems.

For navigation or other state estimation problems, Kalman filter (KF) algorithms have proven to reduce computation errors by combining the mathematical model with a set of measurements (Urrea and Agramonte, 2021). However, when the system dynamics are of nonlinear nature, the KF algorithm needs to be augmented. Either an EKF or an unscented Kalman filter (UKF) are commonly implemented. Whereas the EKF performs an analytic linearisation of the system at each point in time, the UKF performs a statistical linearisation at each time point. In theory, an UKF will outperform an EKF for tracking problems (Yang and Li, 2016). Especially for (highly) nonlinear state space systems, the improved performance of the UKF should become apparent. When applying the theory, this is not always evident. Bourgeaux (2020) provided insight that the UKF was more robust in combination with a spherical harmonics model for estimating the gravitational coefficient of an asteroid or small body. However, the difference in efficiency was not concluded as significant between the EKF and the UKF. Furthermore, St-Pierre and Gingras (2004) demonstrated that the computational time of an UKF is about 20 times larger than as for an EKF for position estimation.

The difficulty in navigating around asteroids is mainly due to the aforementioned irregular gravity field. There are several methods that can be used to estimate the gravitational behaviour of a spacecraft in orbit around an asteroid. However, methods such as spherical harmonics are no longer valid once you enter the sphere encompassing the masses of the asteroid (Hesar et al., 2016). As demonstrated by Spee (2022), estimating the position within

[1] https://www.nasa.gov/feature/goddard/2020/osiris-rex-tags-surface-of-asteroid-bennu, accessed May 5, 2022.

the Brillouin sphere can be feasible by implementing a mass concentration gravity model in the EKF. Although Bourgeaux (2020) and Spee (2022) have established a method to accurately estimate spacecraft position and gravitational coefficients in the proximity of an asteroid, it is yet to be determined how to extend this to also approximate the spacecraft orientation.

In addition, a gap between the necessary observations, and which sensors can provide for it, remains. A lot of research can be found, however either on position or on attitude estimation. Therefore, in this thesis the findings on both are combined, as the estimation of the two do rely on each other. Although it is ascertained that the position and orientation relative to the asteroid should be determined, inertial sensors or star trackers could aid in the estimation. Which sensors are necessary and how they will propagate, and under which conditions they can provide reliable and fast enough estimates, has yet to be established. As previously mentioned, it is expected that sensor fusion should help further gain insight in the research gap.

Operating near irregular-shaped celestial bodies is a challenge. Having onboard situational awareness, enables the ability to maneuver in proximity of near Earth asteroid (NEA)'s, maintain unstable orbits and enable closer flyby's (Nesnas et al., 2021). The use of a sensor fusion algorithm in asteroid observation missions should enhance the available information for spacecraft navigation. In doing so, the spacecraft becomes one step closer to operating autonomously during proximity operations.

1-2 Research Question and Objective

Based on the disquisition of the scientific relevance, it is concluded that the desire to investigate the thesis subject can be justified. Subsequently, the research question, reserach objective, and research sub-questions can be presented. Based on the previous section, it is assumed that sensor fusion is used to estimate the position and attitude of the spacecraft. The deep space spacecraft is a probe sent to an asteroid for observation. The research question reads

"How can sensor fusion applied in autonomous navigation for deep space spacecraft contribute to improving safety and accuracy during proximity operations?"

where improving safety and accuracy implies that a stable orbit can be maintained due to proper estimation of the position and attitude. In that case, the on-board software and sensors can account for time-appropriate control manoeuvres to avoid crashing. As the current position error obtained using DSN position estimation is 150 m at 1 AU distance from Earth, the onboard navigation should be able to have a smaller error to improve accuracy.[2]

To provide an answer to the research question, a navigation filter will be designed, simulated, and analysed. For the navigation filter, a baseline mission scenario is determined first. This hypothetical mission is then simulated in a digital environment, which will be referred to as the true state simulation. The sensor measurements are simulated based on the true state simulation, which are used as measurements for the navigation filter. The research objective is therefore to implement the described navigation filter for state estimation, and demonstrate

[2] https://descanso.jpl.nasa.gov/performmetrics/DSN_NavSysAccuracy.html, accessed June 15, 2022

the feasibility of estimating all states with a selected sensor set. Breaking down the research question and research objective leads to the following sub-questions:

1. What sensor set is necessary to estimate position and orientation of the spacecraft?
2. How can the selected sensors be configured and simulated in the navigation system?
3. To what extent can the navigation filter improve the accuracy of the state estimation?
4. What is the role of the estimation frequency in the accuracy performance of the navigation filter?
5. To what extent can the autonomous navigation system improve the response time when orbital correction manoeuvres are required?

1-3 A Novel Navigation Filter Design

In this section, it is presented what is new to this research, especially in comparison to the preceding thesis research by Razgus (2016), Bourgeaux (2020), and Spee (2022) at the space flight department at aerospace engineering.

To begin with, a true state simulation is set up. The true state simulation is completely verified and benchmarked, such that the method is reproducible and can be applied to other mission scenarios, also for different asteroids. From the true state simulation, a lot of information is available about the dynamics and kinematics of the spacecraft and its environment. Previously, it was often assumed that a lot of that information was available for the navigation filter. For instance, the disturbing forces such as the solar radiation pressure (SRP) or third-body influence of the Sun, was readily supplied to the navigation filter. For my thesis, the approach was to limit the available information of the navigation as much as possible and only rely on a few assumptions. For instance, only the gravitational parameter and an expected rotation rate is assumed about the asteroid.

Furthermore, the state space derivation is new. Whereas Spee (2022) and Bourgeaux (2020) only simulate position estimation of the spacecraft orbiting an asteroid, my thesis focuses on estimating both the position and attitude of the spacecraft. Since the attitude of the spacecraft influences how the forces are exerted on the body, both are equally important to estimate. Although the research by Razgus (2016) does estimate the attitude of the spacecraft, the state space estimation is now derived in the inertial reference frame and the dual quaternions are omitted.

The navigation filter architecture as well as the implementation of the sensor simulation, are also different. The measurements of the inertial measurement unit (IMU) sensor will be considered as inputs in the state space update. In addition, the measurements of a star tracker and a light detection and ranging (LiDAR) are simulated and implemented as two separate measurement updates. In comparison to Spee (2022), the measurements of the position are not readily given in the necessary x-, y-, and z-coodinates with added white noise, but the position information as measured by the LiDAR are simulated. What's more, is that the output rate of each sensor is taken into account, such that a more realistic scenario is given on the availability of measurements needed for state estimation.

As we assume as little information to be known beforehand, it is also not assumed that the spacecraft navigation is in possession of a full surface map of 433 Eros. Also, no mascon models (Spee, 2022), or spherical harmonic coefficients (Bourgeaux, 2020), for estimating the asteroid gravity, are implemented into the navigation filter.

In short, we try to estimate as much as possible with as little information as possible given prior to the system. Hence, the influence of the simulated measurement should become more apparent and give more insight into which sensor set is necessary to achieve position and attitude estimation. The most novel features are navigation filter architecture and the sensor measurement simulation models. Before debating whether complete error state KF algorithms or gravitational field estimation algorithms are necessary, it is necessary to demonstrate the feasibility of this system first. By doing so, the navigation filter can be extended on in future research.

1-4 Report Framework

The deep space spacecraft characteristics and the mission environment can of course change from case to case. Therefore, the current mission heritage of deep space missions targeting small bodies will be consulted. To start with, the mission heritage preceding the research is discussed in Chapter 2. Here, we dive deeper into the scientific relevance of asteroid research and discuss a previous small-body observation mission. Based on the findings, a set of requirements and characteristics of our hypothetical spacecraft can be determined. Having the general mission design established, a decision is made what interaction will take place between the spacecraft and its environment. The assumed kinematic and dynamic behaviour of the spacecraft and its environment is discussed in Chapter 3. Thus, the context of the sensor fusion application is defined in these chapters. The context of the sensor fusion application is thus defined in Chapter 2 and Chapter 3.

Next, a switch to the digital world takes place. All the previously assumed dynamics, kinematics and body characteristics are to be converted to a simulation environment. The environment can then be used for the propagation of various test cases. Chapter 4 will discuss how the environment is simulated, and how the propagation of the state of the spacecraft will be computed. In Chapter 5, the simulation environment is extended to the simulation of the observed state of the spacecraft. The available sensors and their outputs are presented, followed by the simulation of said outputs. How the sensor output simulation is then used for the spacecraft state estimation in a navigation filter is discussed in Chapter 6.

Having all components of the simulation model ready, the mission scenarios can be simulated of which the results are presented in Chapter 7. The interpretations of the results are given in Chapter 8. Next, what conclusions can be drawn from the results, and what can be advised to be included to future research are both discussed in the last part, Chapter 9.

Chapter 2

Mission Heritage

In this chapter, the scientific relevance to the thesis research is further elaborated upon, by looking into the mission heritage. To begin with, the motivation to investigate asteroids and what importance asteroid observation data can have is discussed. A target asteroid is selected, followed by a report of the observation mission that was dispatched to investigate it. Based on the example mission and the previously established research questions, an initial mission design is presented that forms the base for the spacecraft simulation during the research.

2-1 Asteroids

Asteroids are, according to Britt et al. (2014), defined as "small, naturally formed solid bodies that orbit the Sun, are airless, and show no detectable outflow of gas or dust." This last feature is what immediately distinguishes them from comets, which usually have a tail or coma of gas and dust trailing after them (Lissauer and de Pater, 2013). Often, asteroids are referred to as minor planets, as they orbit the Sun. However, they do not posses enough mass to overcome rigid-body forces with their own gravity in order to become spheroid. This results in asteroids with irregular shapes, which is one of their remarkable features.

2-1-1 Scientific Importance

There are multiple arguments for the importance of researching asteroids. To begin with, several asteroids have been classified as a potentially hazardous object (PHO). Asteroids orbiting the Sun with a perihelion less than 1.3 AU are categorised as near-Earth objects (NEO). Of these asteroids, any asteroid that is within a 0.05 AU distance from earth with a diameter of at least 120 metre is then classified as a PHO, as they are likely to survive travel through Earth's atmosphere and induce large damages upon impact (Harris et al., 2014). Multiple asteroid deflecting solutions have been proposed[1] while continuing to detect any

[1] https://news.mit.edu/2020/how-deflect-asteroid-mission-0219, accessed May 5, 2022.

hazardous objects coming Earth's way (Lyzhoft and Wie (2019),Vermeulen (2022)). Asteroid deflection research is beyond the scope of this thesis, as it is focused on asteroid observation.

The first discovery of an asteroid dates back all the way to 1801, when 1 Ceres was discovered by Giuseppe Piazzi (Serio et al., 2002). Since then, more than 400,000 asteroids have been discovered in the main asteroid belt. [2] Asteroids were gradually formed over time, and can range from a few metres to a few kilometres in size. To form an asteroid, small agglomerates gently collided, creating fluffy aggregates (Dymock, 2010). These aggregates in turn then grew to bodies of centimetre width, then to a metre, and so on. Their interiors are very old and could not only aid confirming hypotheses on the formation of the asteroid itself, but also on the age and formation of the solar system. It is believed that due to intense collisional evolution, only a few asteroids possess their primordial surface and mass, where others have reaccredited pieces of mass or have fragmented into smaller bodies (Britt et al., 2014). Due to their gradual formation, asteroids can appear to be loosely bound bodies with fractures and internal voids. Hence, it is not uncommon that asteroids have a porous interior.

The key information that asteroids provide, about the formation environment of the currently known planets, can be extracted from observation results. The material of asteroids is diverse, consisting of, but not limited to, stone, iron, carbon and ice. Most knowledge about asteroids is derived from ground-based telescopic data, where composition information can be derived from spectroscopy. Based on the albedo, asteroids can be classified as carbonaceous (0.04-0.06 albedo), siliceous (0.14-0.17 albedo) or other types.

Carbonaceous and siliceous asteroids are most common, as they currently make up 40% and 17% of the total discovered asteroid population respectively. Carbonaceous asteroids appear to have undergone no heating, as they are further out in the solar system (>2.7 AU), and are considered the primitive, low-temperature condensate objects (Lissauer and de Pater, 2013). Siliceous asteroids are considered a more complex class of asteroids due to their wide range of mineralogy, from which different formation scenarios can be considered (Britt et al., 2014).

Performing deep-space observation has many important advantages as compared to observations from Earth. While it is possible to obtain a great deal of information on asteroids using telescopic data, critical science questions can only be answered with observations from up close. Observing asteroids by means of fly-by's or in-proximity orbits allows for determination of many more characteristics and observing for a longer period of time. Having the adequate payload on-board, one can determine the gravity field, magnetic field, composition, surface characterisation, volume and mass, with more accuracy than from a position on or near Earth.

An orbit closer by a target object will usually result in more accurate observations from the scientific payload, better imaging, and more insight into the gravity field of the asteroid. This is, however, more difficult than orbits further away outside the Brillouin sphere (Hesar et al., 2016). What's more, is that the porous interior can complicate computation of the spacecraft dynamics due to gravitational force. Consequently, asteroids pose as a good target object to research autonomous navigation of the spacecraft: stable orbiting for close-by observation is more complex compared to spheroid-shaped celestial bodies with known density distribution.

[2] https://airandspace.si.edu/exhibitions/exploring-the-planets/online/solar-system/asteroids/, accessed May 5 2022

2-1-2 Target Asteroid: 433 Eros

For the research context, asteroid 433 Eros has been selected as the target. Proximity operations around 433 Eros pose as a great test case. Enough data is available about the gravitational field from the Near Earth Asteroid Rendezvous (NEAR)-Shoemaker mission to simulate a spacecraft orbiting the asteroid (Chanut et al. (2014), McAdams et al. (2000)). The history of the NEAR-Shoemaker mission will be discussed in Section 2-2.

433 Eros has been classified as a primitive undifferentiated silicate asteroid of the Amor type within the NEO group, as it is orbit crossing with Mars. However, due to its larger perihelion and semi-major axis than other NEO, it can come as close to Earth as 0.15 AU.[3] It is even believed that it would be possible 433 Eros can hit the Earth in the coming 10^6 to 10^8 years, as its orbit can gradually change from Mars-crossing to Earth-crossing (Michel et al., 1996).

As previously stated, (siliceous) asteroids can contain a wide range of materials and can be of different densities throughout their interior. Based on the data resulting from the NEAR-Shoemaker mission, it was concluded that there is an offset of 52 meters between the geometric centre and the centre of mass of 433 Eros (Thomas et al., 2002). This offset is thus likely occurring because of porosity or irregularities in material density present in the asteroid. Considering a diameter of about 17 km, it is still very close to each other, and 433 Eros is likely to have a homogeneous density distribution (Miller et al., 2002). Furthermore, it was concluded that the asteroid is lacking a magnetic field (Siddiqi, 2018) which would impose absence of any metallic iron or other magnetic minerals.

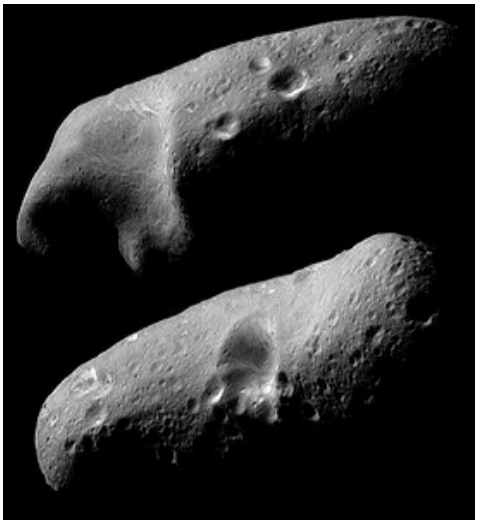

(a) Mosaic of two images of 433 Eros taken by NEAR-Shoemaker on February 14.[4]

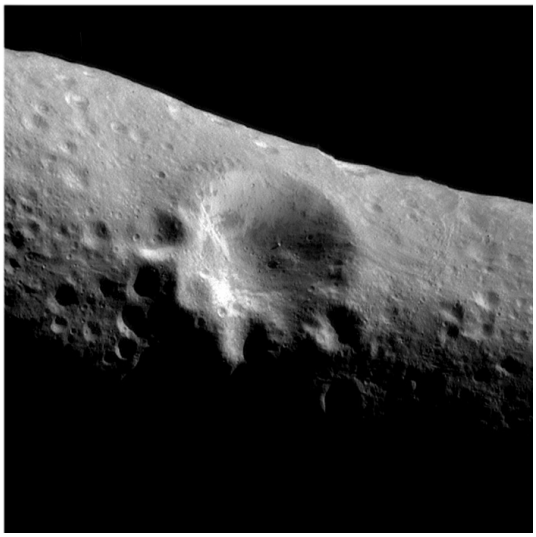

(b) Image of Psyche crater on 433 Eros taken by NEAR-Shoemaker on February 14.[5]

As can be seen from Figure 2-1a, the surface features of 433 Eros are highly diverse, consisting of sinuous or linear depressions, scarps and riches. The largest depression found on 433 Eros'

[3] https://ssd.jpl.nasa.gov/sbdb.cgi?sstr=2000433#content, accessed March 10,2021.

[4] https://nssdc.gsfc.nasa.gov/imgcat/html/object_page/nea_0126712790_mos.html, accessed May 5, 2022.

[5] https://nssdc.gsfc.nasa.gov/imgcat/html/object_page/nea_0127531846_mos.html, accessed May 5, 2022.

surface is the 5.3 km wide crater Psyche, visible in Figure 2-1b. The unique shaping of the asteroid induces irregular gravitational forces to be experienced by an orbiting spacecraft. This poses as a good example of future asteroid observation missions, where irregularity of the usually assumed constant μ, the gravitational parameter, has to be accounted for during navigation. The exact characteristics of 433 Eros can be found below in Table 2-1. These parameters can be used for the dynamics of the spacecraft environment in Chapter 3 and the simulation of the asteroid in the algorithm described in Chapter 4.

Table 2-1: Characteristics of Mission Objective 433 Eros (Miller et al. (2002)).[6,7]

Parameter	Value [Unit]
Volume	2503±25 [km^3]
Bulk density	2.670.03± [g/cm^3]
Mass	6.6904±0.03 $\cdot 10^{15}$ [kg]
Diameter	16.84±0.06 [km]
Rotation period	5.27025547 [h]
Geometric albedo	0.25±0.06 [-]
Point mass μ	4.3838006364736 $\cdot 10^5$ [m^3 s^{-2}]
Moments of Inertia	**Value [Unit]**
I_{xx}	17.09 [km^2]
I_{yy}	71.79 [km^2]
I_{zz}	74.49 [km^2]

2-2 NEAR-Shoemaker Mission

Since 433 Eros has been selected as the target asteroid, the most relevant mission to base the research context on is the NEAR-shoemaker mission. The mission was novel for its time: a spacecraft had never performed a fly-by, orbit insertion and a landing on a small body before. The main objective was to characterise 433 Eros' general physical properties such as inertial mass distribution and morphology, as well as determining any presence of mineral components or a magnetic field. The secondary objective was the observation and mapping of C-type asteroid 253 Mathilde.

The spacecraft was launched on February 17, 1996, with a launch mass of 805 kg and a ΔV budget of 1420 m/s. On its trajectory towards 433 Eros, the fly-by of 253 Mathilde was performed on June 27, 1997 (McAdams et al., 2000). Although the spacecraft was scheduled for a rendez-vous on 20 December 1998, a spacecraft anomaly caused a delay in the operation. Control of the spacecraft was recovered just in time to perform a high-speed fly-by at 3,900 km from the asteroid (Williams, 2002). The rescheduled rendez-vous took place on February 14, 2000, and one year later the spacecraft performed a successful landing on February 12, 2001 (Cheng, 2002).

The largest challenge of the proximity operations around, and landing on 433 Eros, was the highly irregular gravity field. The gravity field was difficult to approximate beforehand. The

[6] https://ssd.jpl.nasa.gov/tools/sbdb_lookup.html#/?sstr=eros, accessed May 9,2022.
[7] https://newton.spacedys.com/neodys/index.php?pc=1.1.1&n=433, accessed May 9 2022.

Figure 2-2: Artists rendition of the NEAR-Shoemaker spacecraft and 433 Eros.[8]

predictions of the spacecraft dynamics were performed using the radiometric data sent to the ground stations, causing slow convergence of the gravity field determination. To overcome the issue, optical landmark tracking was used, which was also a novel approach for deep space missions (Williams, 2002). In the beginning of the proximity operations around 433 Eros, the spacecraft was in a 50 km radius orbit. On July 13, 2000, the spacecraft moved into a lower orbit at a 35 km radius for ten days, coming as close as 19 km to the asteroids surface. Next, a close fly-by of 5.3 km from the surface was performed on October 26 (Cheng, 2002). At the end of 2000, the spacecraft descended again to a 35 km orbit to initiate another set of close flyby's of 5 or 6 km to the surface (Siddiqi, 2018). Through these operations, the rotation, pole, and gravity of 433 Eros could be determined with more accuracy. Not only the asteroids features were determined, but also the effect of perturbing forces such as the solar gravity gradient. Techniques such as optical navigation, landmark tracking, and laser radar data analysis contributed to these findings (McAdams et al., 2000).

Table 2-2: Power and Mass budget instruments NEAR mission (Santo et al., 1995).

Instrument	**Mass [kg]**	**Power [W]**
Multi-Spectral Imager	7.8	13.9
NEAR Imaging Spectrograph	14.2	20.0
X-Ray/Gamma-Ray Spectrograph	27.3	31.3
Magnetometer	1.6	1.5
Laser Rangefinder	5.1	26.8
Star Tracker	2.7	9.9
Inertial Measurement Unit	5.3	21.4
Digital Sun Sensors (5)	1.9	0.3

[8] https://civspace.jhuapl.edu/destinations/missions/near, accessed March 12, 2021.

New insights were found during the operation of NEAR, using the instruments found in Table 2-2. Based on the findings of the gamma Ray Spectrometer (GRS), the composition of 433 Eros appears similar to chondrites that can be found on Earth (Cheng, 2002). Furthermore, it could be concluded that there is no magnetic field around the asteroid, based on the findings by the magnetometer. With the help of the multi-spectral imager (MSI) and the NEAR Imaging Spectrograph, over 70% of the surface of the asteroid could be mapped (Siddiqi (2018)). The images showed a surface with some interesting features: ridges and grooves can extend a couple of kilometres across the surface, of which the longest is 18 km (Cheng, 2002). This could conclude that the asteroid is not a rubble pile bound over time by gravity, but is a more consolidated body (Thomas et al., 2002). The findings by NEAR will be used in Subsection 3-4-1 to model the asteroid's gravity field.

2-3 Mission & Spacecraft Design

Before diving into the research, some constraints on the research direction have to be established. Based on the NEAR mission, there is not only a lot of information about the target asteroid available, but also on the design of a successful asteroid observation mission. Therefore, the needs and constraints that can be derived from the example mission are explained here, of which the mission design requirements can be found in Appendix A.

The research will focus on simulations of the asteroid observation phase. As discussed in Section 1-1, both the orientation and the position of the spacecraft need to be identified during the (autonomous) proximity operations around an asteroid. The orientation and position are considered to be relative to the asteroid. It is assumed that, similar to the example mission, the initial orbit around the asteroid will have a radius of 50 km.

Although the main body of NEAR is defined as an octagonal prism with panel lengths of 1.7 m, a simplified cuboid design for the spacecraft simulation will be used.[9] For the solar panels, four 1.2 by 1.8 m panels are positioned at the top panel of the spacecraft in windmill configuration.[10] To keep the mission design simple, it is assumed that power is available to all systems necessary in the observation phase. The mission context will not focus on power generation and Sun pointing in order to do so.

On the contrary, the navigation architecture does lie within the scope of the research. The guidance navigation & control (GNC) system was designed to have 3-axis attitude control, with a pointing stability of 1.7 millirad and a pointing accuracy of 50 microradians (Santo et al., 1995). A redundant set of four reaction wheels was incorporated. These were complemented with eleven smaller monopropellant thrusters and one larger bipropellant thruster Lee and Santo (1996). The common control procedures were handled by just the reaction wheels. In order to maintain control over the vehicle, momentum dump was carried out by the thrusters from time to time. This was detected automatically by the GNC system. Although the control operations are the next step for autonomous navigation of the spacecraft, they are not defined for the mission context. As the research focuses on the estimation of the position and orientation relative to the asteroid, the control of the spacecraft is beyond the scope.

[9] https://nssdc.gsfc.nasa.gov/planetary/near.html accessed May 9 2022
[10] https://nssdc.gsfc.nasa.gov/nmc/spacecraft/display.action?id=1996-008A, accessed May 9 2022

For the inertial sensors, redundancy was incorporated by integrating a 4-axis pyramid shape configuration of 4 inertial measurement unit (IMU)'s, each consisting of an accelerometer and a gyroscope (Strikwerda et al., 1998). The sensor redundancy is not yet taken into account. It is assumed that all sensors can provide measurements throughout the orbit that is simulated. Therefore, it is also assumed that the navigation system will arrive at the destination without any failure. Of course, a lot of information is known about the available sensor types that were onboard of the NEAR spacecraft. The final sensor selection is presented in Chapter 5.

To summarise, the following assumptions are made about the mission design:

1. The interplanetary travel to 433 Eros will be successful without damaging any of the navigation sensors.
2. Power is available to all necessary subsystems during the simulated orbit trajectory.
3. The spacecraft will orbit 433 Eros at 50 km radius.
4. The navigation sensors will provide measurements for the full duration of the simulated orbit trajectory.
5. The spacecraft shall have the same mass as the NEAR spacecraft.
6. The spacecraft shall have a simplified version of the dimensions of the NEAR spacecraft in the form of a panel model.
7. The navigation system will at least estimate the position and orientation of the spacecraft relative to the asteroid.

Now that a set of assumptions for the mission context has been set up, the base for the mission has been laid out. This brings us to the next chapter: defining the mission environment and presenting the dynamic and kinematic equations that come into play.

Chapter 3

Dynamics and Kinematics of the Spacecraft and its Environment

Within this chapter, a dynamic model for the spacecraft, including its kinematics, and the environment is proposed. The model and the assumptions made serve as a base for the algorithm that simulates the propagation of the spacecraft and the asteroid. A list of the main assumptions and constraints summarising the model can be found below.

1. There are three reference frames considered: the inertial, asteroid and spacecraft reference frame, denoted by subscript I, A, and B respectively.
2. Propagation of the dynamics is computed using the Cartesian coordinates in the inertial frame.
3. The asteroid's orbit around the Sun is not considered in the simulation.
4. The asteroid has a constant rotation about the z-axis of the inertial frame.
5. The gravitational force of the asteroid exerted on the spacecraft is computed using a polyhedron model of the asteroid.
6. The gravitational acceleration of the spacecraft due to the asteroid is computed in the asteroid reference frame, and converted to the inertial reference frame each time step. Hence, the total acceleration of the spacecraft is computed in the inertial reference frame.
7. Disturbance forces due to the gravity of the Sun and the solar radiation pressure (SRP) are simulated.
8. Forces due to gravity gradient torque are omitted.
9. Propagation of attitude of the spacecraft and the asteroid are computed using unit quaternions.

Based on the assumptions and constraints listed, the next chapter will present the design of the algorithm and the simulation of the asteroid and the spacecraft. The assumptions made above are explained in more detail in this chapter. To start with, the used coordinate systems are presented in Section 3-1, then frames of reference are discussed in Section 3-2, followed by the rotations and reference frame transformations in Section 3-3. Next, the dynamics and kinematics are presented Section 3-4 and Section 3-5 respectively.

3-1 Coordinate Systems in Mission Environment

For the reproducibility of the research, the coordinate systems used in the research are presented. There are three coordinate systems considered throughout the research, of which the most common is the Cartesian coordinate system, which will not be explained. As the Kepler and spherical coordinate system are not necessarily common in the control engineering field, these will be discussed in Subsection 3-1-1 and Subsection 3-1-2, respectively.

3-1-1 Kepler Coordinate System

Within a Kepler coordinate system, orbital elements are used to identify a specific orbit. Kepler coordinates can be very useful in mission design as they characterise the propagation throughout one orbital period and the current position of the satellite in the orbit.

Below in Figure 3-1, the coordinate system can be seen from a two-dimensional view in the xy-plane. Here, F is the focal point around which the orbit propagates, where F' is the point mirrored around the centre point C. Point A is defined as the pericentre, and A' as the apocentre.

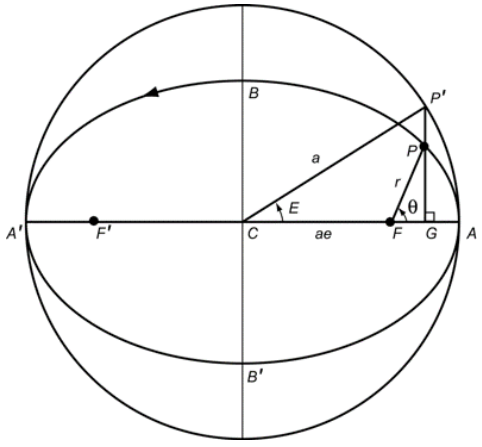

Figure 3-1: Kepler orbit and parameters in 2D view, taken from Wakker (2015).

The first orbital elements to discuss are the semi-major axis, a, and the eccentricity, e, of the orbit. The semi-major axis is defined as the half of the distance between the pericentre and the apocentre, indicated with point C. The eccentricity denotes the circularity of the orbit, which for stable orbits has a range of $[0,1\rangle$. For example, an eccentricity of 0 defines a perfect circular orbit. In that case, the points F and C coincide and the trajectory is followed as seen in point P'.

For any eccentricity between 0 and 1, the orbit is elliptical, and follows the trajectory of point P. The radius of the orbit, r, is not equal to the semi-major axis anymore, and can be computed using

$$r_i = \frac{a(1-e^2)}{1+e\cos(\theta_i)}, \tag{3-1}$$

where θ_i, the true anomaly, is the angle between the horizontal of the focal point and pericentre, and the line connecting the focal point to position P. For a given point in the orbit, the velocity in direction of the orbital path can be computed using

$$V_i^2 = \mu\left(\frac{2}{r_i} - \frac{1}{a}\right), \tag{3-2}$$

where μ is the gravitational parameter of the body in point F.

In order to define orbital elements in a three dimensions, three angles are added to define the position, as can be seen in Figure 3-2. The inclination, i, defines the tilt between a reference plane and the plane of the orbit. The angle of the X-axis of the reference frame and the point where the ascending node crosses the reference plane is defined as Ω. ω then defines the angle between the right ascending node and the pericentre on the orbital plane.

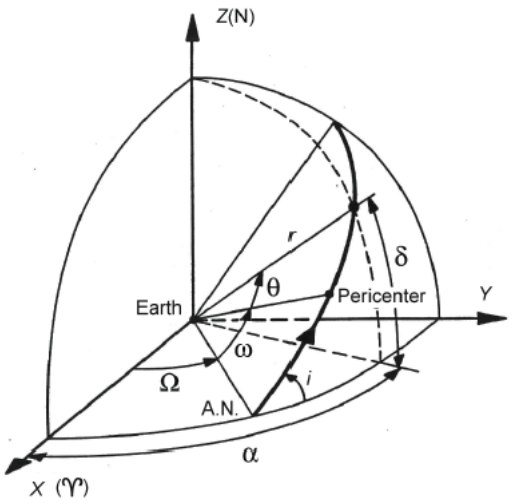

Figure 3-2: Definition of the orbital elements i, Ω, ω , and the position of a satellite from Wakker (2015).

To convert the Kepler coordinates to Cartesian coordinates, the position is computed using

$$\begin{pmatrix} x_i \\ y_i \\ z_i \end{pmatrix} = \begin{pmatrix} l_1 & l_2 \\ m_1 & m_2 \\ n_1 & n_2 \end{pmatrix} \begin{pmatrix} \xi_i \\ \eta_i \end{pmatrix}, \tag{3-3}$$

where

$$\begin{aligned} l_1 &= \cos(\Omega)\cos(\omega) - \sin(\Omega)\sin(\omega)\cos(i), \\ l_2 &= -\cos(\Omega)\sin(\omega) - \sin(\Omega)\cos(\omega)\cos(i), \\ m_1 &= \sin(\Omega)\cos(\omega) + \cos(\Omega)\sin(\omega)\cos(i), \\ m_2 &= -\sin(\Omega)\sin(\omega) + \cos(\Omega)\cos(\omega)\cos(i), \\ n_1 &= \sin(\omega)\sin(i), \\ n_2 &= \cos(\omega)\sin(i), \end{aligned} \tag{3-4}$$

and

$$\begin{pmatrix} \xi_i \\ \eta_i \end{pmatrix} = \begin{pmatrix} r_i & \cos(\theta_i) \\ r_i & \sin(\theta_i) \end{pmatrix}. \tag{3-5}$$

A more detailed description of the relations between the Kepler and Cartesian coordinate system can be found in Appendix B.

3-1-2 Spherical Coordinate System

This coordinate system defines a point on a sphere. Using three parameters, the coordinate on the sphere is determined. To begin with, ρ defines the radius of the sphere, also known as the range from the origin to the coordinate. The elevation, ϵ, is the angle between the xy-plane and the coordinate on the sphere. The azimuth, ϕ is then the angle between the x-axis and the orthogonal projection on the xy-plane, as can be seen in Figure 3-3.

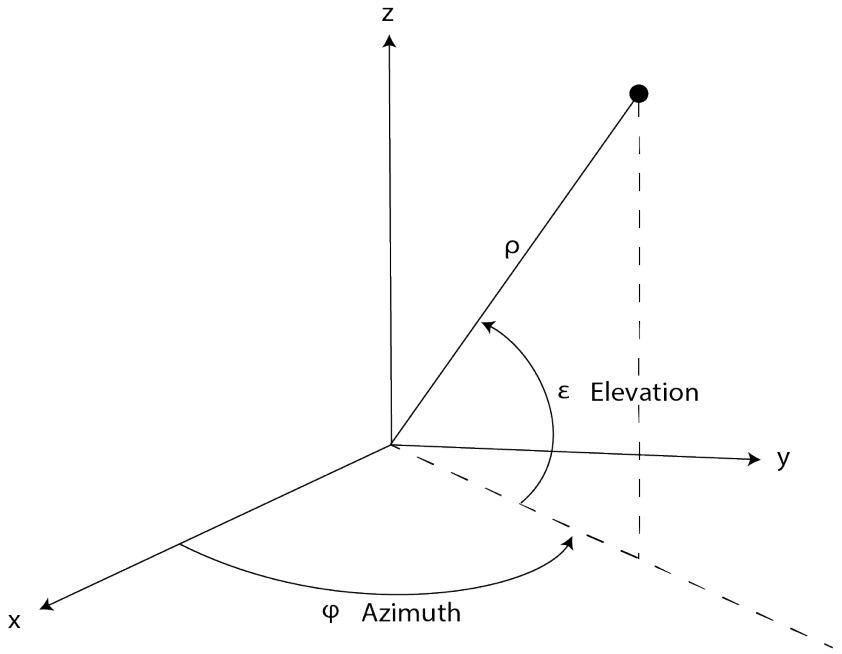

Figure 3-3: Spherical coordinate representation.

To convert from the spherical coordinate system to the Cartesian coordinate system, the relations are defined as

$$\begin{aligned} x &= \rho\cos(\epsilon)\cos(\phi), \\ y &= \rho\sin(\epsilon)\cos(\phi), \\ z &= \rho\sin(\phi). \end{aligned} \tag{3-6}$$

From Cartesian to spherical coordinates, the range can be calculated as

$$\rho = \sqrt{x^2 + y^2 + z^2}, \tag{3-7}$$

and the angles can be computed using

$$\begin{aligned} \epsilon &= \arctan\left(\frac{y}{x}\right), \\ \phi &= \arctan\left(\frac{z}{\sqrt{x^2 + y^2}}\right). \end{aligned} \tag{3-8}$$

3-2 Reference Frames

In this section the reference frames used throughout dynamic equations are presented. The three main frames are presented, which are all used either during the simulation of the spacecraft or the navigation filter.

3-2-1 Inertial Reference Frame

In this research, the inertial reference frame is considered to coincide with the centre of volume of the asteroid. The inertial frame is considered to be a non-rotating frame, and is depicted below in Figure 3-4.

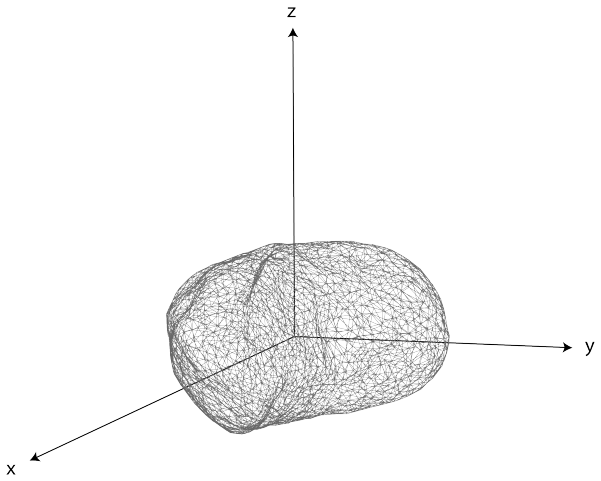

Figure 3-4: Inertial reference frame representation.

From here onward, the inertial reference frame is denoted with the subscript I.

3-2-2 Asteroid Reference Frame

Initially, the origin of the asteroid reference frame is the same as the inertial frame. However, as a constant rotation about its z-axis is present, the asteroid is rotating about the inertial frame. Therefore, the x- and y-axis of the asteroid frame do not coincide with the inertial frame. As can be seen in Figure 3-5, the rotation of the asteroid reference frame about the z-axis is denoted with rotation rate $\omega^A_{A/I}$. As can bee sin The asteroid reference frame is

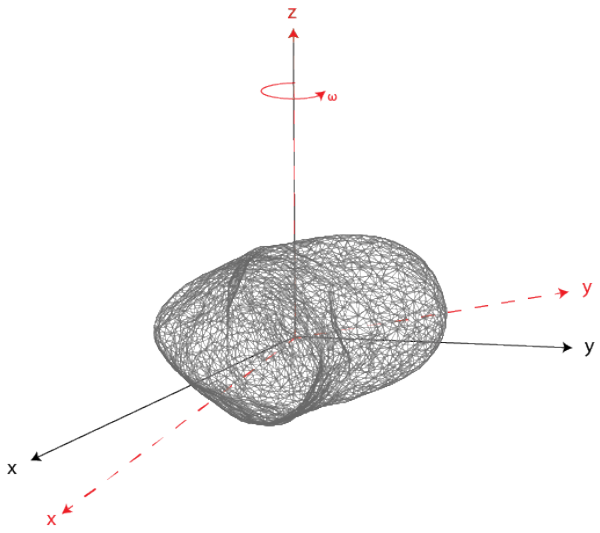

Figure 3-5: Asteroid reference frame representation; asteroid reference frame represented in dashed red lines, the inertial frame in solid black lines.

denoted with the subscript A.

3-2-3 Spacecraft Body Reference Frame

The last reference frame is the spacecraft body frame, which is placed in the geometric centre of the main body of the spacecraft, coinciding with the axes of the principal moments of inertia. In Figure 3-6, a visualisation of the spacecraft and the spacecraft body reference frame can be seen. The z-axis extends through the bottom of the spacecraft, and is defined right handed. It can be seen that the spacecraft is symmetric about both the x- and y-axis.

The spacecraft body reference frame is denoted with the subscript B. Throughout the simulation model of the position and velocity of the spacecraft, a point mass in the origin of the spacecraft reference frame is considered. Where relevant, the geometry of the spacecraft is of course taken into account, such as for the derivation of the SRP in Subsection 3-4-2.

3-3 Orientation Representation

In this section, the concepts of reference frame transformation, Euler angles, and quaternions are presented. These concepts are all used throughout the research to describe the orientation of the reference frames with respect to each other. Bold faced symbols refer to vector quantities.

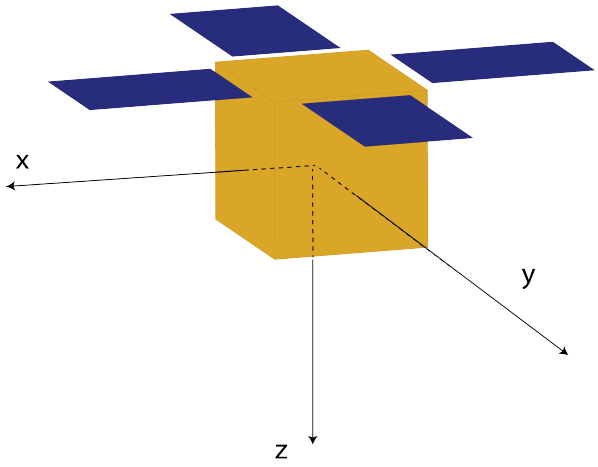

Figure 3-6: Spacecraft reference frame representation.

3-3-1 Reference Frame Transformations

Now that all reference frames have been defined, we need to be able to switch between them. This can be done by using direction cosine matrix (DCM) multiplication. Consider the two reference frames A and I which were previously presented. The transformation from A to I is then denoted as

$$\mathbf{R}_I = C_{I/A}\mathbf{R}_A, \tag{3-9}$$

where $\mathbf{R}$ represents a position vector, and $C_{I/A}$ is a DCM from frame A to frame I. The DCM is orthonormal (Markley and Crassidis, 2014) and thus has the properties

$$\begin{aligned} &C = -C, \\ &C_{B/I} = C_{I/B}^T, \\ &C_{I/B}C_{I/B}^T = C_{I/B}^T C_{I/B} = I, \end{aligned} \tag{3-10}$$

where I is the identity matrix. It is possible to multiply multiple rotation matrices such that

$$C_{B/I} = C_{B/A}C_{A/I}. \tag{3-11}$$

3-3-2 Orientation Using Euler Angles

A common method to express orientation is using Euler angles to represent the spacecraft attitude. Rotating a reference frame using Euler angles is performed in three steps: one transformation for each rotation about another axis. For two given reference frames with a coinciding origin, the rotation of angle θ_z about the z-axis is described as

$$\begin{bmatrix} x_2 \\ y_2 \\ z_2 \end{bmatrix} = \begin{bmatrix} \cos(\theta_z) & \sin(\theta_z) & 0 \\ -\sin(\theta_z) & \cos(\theta_z) & 0 \\ 0 & 0 & 1 \end{bmatrix} \begin{bmatrix} x_1 \\ y_1 \\ z_1 \end{bmatrix}, \tag{3-12}$$

where x_1,y_1,z_1 are the coordinates of point P in reference frame 1, and x_2,y_2,z_2 are its coordinates in frame 2. Similarly, if the rotation of angle θ_y is about the y-axis, the coordinates are computed using

$$\begin{bmatrix} x_2 \\ y_2 \\ z_2 \end{bmatrix} = \begin{bmatrix} \cos(\theta_y) & 0 & -\sin(\theta_y) \\ 0 & 1 & 0 \\ \sin(\theta_y) & 0 & \cos(\theta_y) \end{bmatrix} \begin{bmatrix} x_1 \\ y_1 \\ z_1 \end{bmatrix}, \tag{3-13}$$

and for a rotation of angle θ_x about the x-axis as

$$\begin{bmatrix} x_2 \\ y_2 \\ z_2 \end{bmatrix} = \begin{bmatrix} 1 & 0 & 0 \\ 0 & \cos(\theta_x) & \sin(\theta_x) \\ 0 & -\sin(\theta_x) & \cos(\theta_x) \end{bmatrix} \begin{bmatrix} x_1 \\ y_1 \\ z_1 \end{bmatrix}. \tag{3-14}$$

If X, Y, and Z denote the rotation matrices about the respective axes, the multiplication of all three results in a DCM. Here, the order is significant, as another order can result in a different orientation. By default, the rotation sequence XYZ is taken, such that the order of multiplications is

$$P_2 = [\mathrm{ZYX}]P_1, \tag{3-15}$$

where the rotation about the x-axis is carried out first. The total rotation angle from one frame to another about the Euler axis is depicted in Figure 3-7

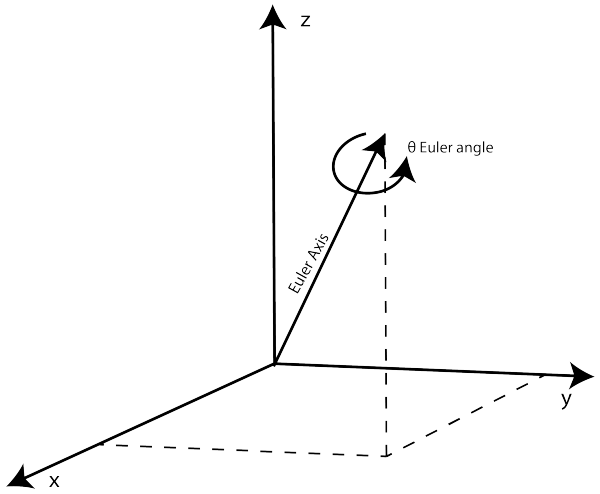

Figure 3-7: Euler angle and Axis in an inertial reference frame.

An advantage to the Euler angle representation is the intuitive visualisation of rotations and the simplicity of using only three angles to express the orientation. Unfortunately, the expression comes with disadvantages when applied to spacecraft control. Within navigation filter problems, the dynamic models now rely on three separate multiplications for the rotational sequences, which are computationally expensive when they have to be computed each time step. Moreover, any orientation can be expressed with different combinations of rotation sequences, meaning they are never unique. In addition, wrapping can occur for rotations larger than π rad, which can become a problem when using Euler states in a navigation filter.

Furthermore, the rotational sequences contain a singularity where the model is not applicable anymore (Guha, 2015). These usually occur when the middle rotation takes a particular value, which is often equal to $\frac{\pi}{2}$. Where the singularity only causes a mathematical apparent loss, of a degree of freedom, for gimbal lock there is a physical loss of a degree of freedom (Yang, 2012). When using an inertial measurement unit (IMU) for spacecraft navigation, the rotations of the gimbals of the gyroscope can cause two gimbals to become coplanar. It is not possible to stabilise the platform with control torques, and proper orientation estimation is not possible with the two remaining degrees of freedom (Hemingway and O'Reilly, 2018).

3-3-3 Orientation Using Quaternions

Due to the disadvantages of using Euler angles for attitude representation, another method to express orientation is needed. Here, it is chosen to use quaternions instead. Following the Euler's rotational theorem, a quaternion can also be defined by a rotation angle and a rotational axis (Groÿekatthöfer and Yoon, 2012), as could be seen in Figure 3-7. As there are different ways to notate quaternion representation, this section discusses the notation we used in the algorithm, with the accompanying equations. The quaternion here is defined as

$$\mathbf{q} = \begin{bmatrix} \|\mathbf{e}\| \sin\left(\frac{\theta}{2}\right) \\ \cos\left(\frac{\theta}{2}\right) \end{bmatrix}, \tag{3-16}$$

where $\|\mathbf{e}\|$ is the vector of the Euler axis, and θ is the Euler angle. The quaternion can also be notated as the sum of the vector and the scalar part where

$$\mathbf{q} = iq_1 + jq_2 + kq_3 + q_4, \tag{3-17}$$

and

$$i^2 = j^2 = k^2 = ijk = -1. \tag{3-18}$$

The quaternion can thus be expressed as a vector where the directional part is equal to

$$\mathbf{q}_{1:3} = \begin{bmatrix} q_1 \\ q_2 \\ q_3 \end{bmatrix}, \tag{3-19}$$

and is combined with a scalar part such that the complete quaternion is equal to

$$\mathbf{q} = \begin{bmatrix} \mathbf{q}_{1:3} \\ q_4 \end{bmatrix}. \tag{3-20}$$

Taken from the notation by Yang (2012), the conjugate, norm, and inverse form of a quaternion are

$$\mathbf{q}^* = \begin{bmatrix} -\mathbf{q}_{1:3} \\ q_4 \end{bmatrix}, \tag{3-21}$$

$$\|\mathbf{q}\| = \sqrt{q_1^2 + q_2^2 + q_3^2 + q_4^2}, \tag{3-22}$$

$$\mathbf{q}^{-1} = \frac{\mathbf{q}^*}{\|\mathbf{q}\|}. \tag{3-23}$$

There are two possible products of two quaternions. As they only differ in the convention of the sign of the cross product of the vector part of the quaternion, they are equal to each other such that

$$\mathbf{q}_i \otimes \mathbf{q}_j = \mathbf{q}_j \odot \mathbf{q}_i. \tag{3-24}$$

where the products are defined as

$$[\boldsymbol{q}\otimes] = \begin{bmatrix} \boldsymbol{q}_4 I_3 - [\boldsymbol{q}_{1:3}\times] & \boldsymbol{q}_{1:3} \\ -\boldsymbol{q}_{1:3}^T & q_4 \end{bmatrix}, [\boldsymbol{q}\odot] = \begin{bmatrix} \boldsymbol{q}_4 I_3 + [\boldsymbol{q}_{1:3}\times] & \boldsymbol{q}_{1:3} \\ -\boldsymbol{q}_{1:3}^T & q_4 \end{bmatrix}, \tag{3-25}$$

where I_3 is a 3 by 3 identity matrix. The general cross product is defined as

$$[\boldsymbol{a}\times] = \begin{bmatrix} 0 & -a_3 & a_2 \\ a_3 & 0 & -a_1 \\ -a_2 & a_1 & 0 \end{bmatrix}. \tag{3-26}$$

For a unit quaternion, the norm is always equal to 1. Unit quaternions can be used to define the attitude of a rigid body. When using unit quaternions to express orientation or rotations, the singularity, wrapping, and gimbal lock issues of the Euler angles are avoided. For unit quaternions, it holds that

$$\|\mathbf{q}\| = 1, \tag{3-27}$$

which gives

$$\mathbf{q}^{-1} = \mathbf{q}^*. \tag{3-28}$$

Expressing a quaternion as a rotation matrix gives

$$\begin{aligned} C(\boldsymbol{q}) &= \left(q_4^2 - \|\boldsymbol{q}_{1:3}\|^2\right) I_3 + 2\boldsymbol{q}_{1:3}\boldsymbol{q}_{1:3}^T - 2q_4 \left[\boldsymbol{q}_{1:3}\times\right] \\ &= \begin{bmatrix} q_1^2 - q_2^2 - q_3^2 + q_4^2 & 2\left(q_1q_2 + q_3q_4\right) & 2\left(q_1q_3 - q_2q_4\right) \\ 2\left(q_1q_2 - q_3q_4\right) & -q_1^2 + q_2^2 - q_3^2 + q_4^2 & 2\left(q_2q_3 + q_1q_4\right) \\ 2\left(q_1q_3 + q_2q_4\right) & 2\left(q_2q_3 - q_1q_4\right) & -q_1^2 - q_2^2 + q_3^2 + q_4^2 \end{bmatrix}. \end{aligned} \tag{3-29}$$

The reverse operation from a transformation matrix to a unit quaternion is defined as

$$\mathbf{q}(C) = \frac{1}{2} \begin{pmatrix} \operatorname{sign}\left(C_{32} - C_{23}\right)\sqrt{1 + C_{11} - C_{22} - C_{22}} \\ \operatorname{sign}\left(C_{13} - C_{31}\right)\sqrt{1 - C_{11} + C_{22} - C_{22}}) \\ \operatorname{sign}\left(C_{21} - C_{12}\right)\sqrt{1 - C_{11} - C_{22} + C_{22}}) \\ \sqrt{1 + C_{11} + C_{22} + C_{33}} \end{pmatrix}. \tag{3-30}$$

Whereas quaternions are computationally inexpensive (Yang, 2012), and is not dependent on rotational sequences like Euler angles, problems occur when linearising quaternions in a state space model. As demonstrated by Zhou and Colgren (2005), a linearised quaternion state space model can be obtained, but unfortunately is uncontrollable. This would mean that for attitude estimation using Kalman filtering, it is not possible to obtain convergence for the state estimation. Fortunately, Yang (2012) demonstrated that using only the vector elements of the quaternion, full controllability of the attitude and convergence of the attitude estimation can be obtained. As shown by Ding and Gao (2020), using an multiplicative extended Kalman filter (MEKF), full estimation of the attitude is possible. The methodology of the general Kalman filter (KF), the quaternion error state, and the MEKF will be presented in Section 6-2.

3-4 Position Dynamics

This section covers the equations used for the propagation of the position of the spacecraft relative to the asteroid body. As the inertial reference frame is coinciding with the asteroid frame and is only deviating due to a rotation about the z-axis, the propagation of the asteroid in its orbit around the Sun is not considered.

The general equations of a body having an acceleration due to a force exterted on the body are described by

$$\frac{d\mathbf{r}}{dt} = \mathbf{v}, \tag{3-31}$$

$$\frac{d\mathbf{v}}{dt} = \frac{\mathbf{F}}{m} = \mathbf{a}, \tag{3-32}$$

where $\mathbf{r}$,$\mathbf{v}$ and $\mathbf{a}$ are the vectors for position, velocity and acceleration respectively. Parameter m is the body mass, t is the time and $\mathbf{F}$ are the forces exerted on the body.

According to Wakker (2015), one can formulate a two-body problem as

$$\frac{d^2\mathbf{r}_{21}}{dt^2} = -G\frac{m_2 + m_1}{\mathbf{r}_{21}^3}\mathbf{r}_{21} = \mathbf{a}, \tag{3-33}$$

where $\mathbf{r}_{21}$ is the position vector of P_1 to P_2, G is the gravitational constant, and m_1 and m_2 are the masses of the bodies in P_1 and P_2 respectively. Taking into account that P_2 is positioned in the origin of a non-rotating reference frame and that

$$\mathbf{r}_{21} = \mathbf{r}_1 - \mathbf{r}_2, \tag{3-34}$$

and

$$\mathbf{r}_1 = -\frac{m_2}{m_1}\mathbf{r}_2, \tag{3-35}$$

the force acting on a body situated at P_1 is then

$$\mathbf{F}_1 = -G\frac{m_1 m_2}{\mathbf{r}_{21}^3}\mathbf{r}_{21}. \tag{3-36}$$

3-4-1 Asteroid Modelling and Dynamics

It is assumed that the asteroid, and thus the asteroid reference frame, is rotating about its z-axis at a constant rotation rate. Therefore,

$$\dot{\boldsymbol{\omega}}_{A/I}^{A} = 0. \tag{3-37}$$

Given that the rotation of 433 Eros is 1639.38922 ± 0.0002 degrees per day (Miller et al., 2002), the rotation rate of the asteroid frame about the inertial frame expressed in the asteroid frame is equal to,

$$\boldsymbol{\omega}_{A/I}^{A} = \begin{bmatrix} 0 \\ 0 \\ 3.311659701405230 \cdot 10^{-4} \end{bmatrix} \text{rad/s}. \tag{3-38}$$

The gravitational force of the asteroid on the spacecraft can be defined as a force exerted by a point mass, using

$$\mathbf{a}_g = -\frac{\mu}{r^3}\mathbf{r}. \tag{3-39}$$

where $\mathbf{a}_g$ is the acceleration due to gravitational force of the asteroid, μ is the gravitational parameter of the asteroid, $\mathbf{r}$ is the distance between the two point masses.

Although Bourgeaux (2020) demonstrated stable orbit approximation using spherical harmonics, this method is not applicable for gravity field estimation within the Brillouin sphere. The Brillouin sphere can be defined as the smallest possible sphere circumscribing a body in the three dimensional space. Using a constant density polyhedron model of 433 Eros, Chanut et al. (2014) was able to demonstrate propagation of stable orbits below the 36 km sphere circumscribing the asteroid. This is the most straightforward approximation for an asteroid with a highly irregular shape, especially when orbiting close to or within the Brillouin sphere (Hesar et al., 2016). Spee (2022) verified that the polyhedron gravity model is a high-precision and non-diverging gravity field model, also when assuming constant density.

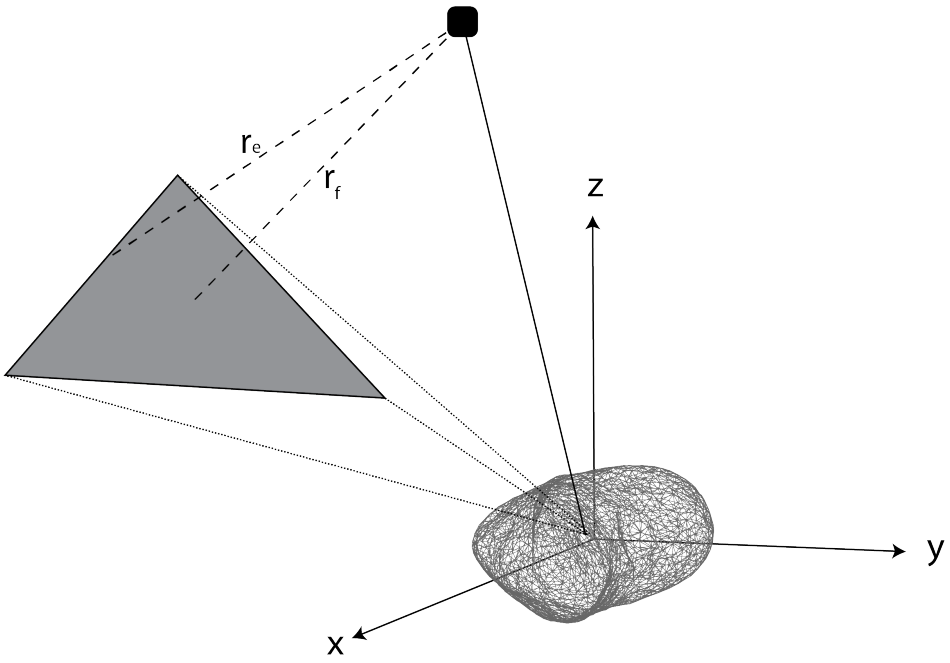

Figure 3-8: Visualisation of Polyhedron.

The polyhedron model approximates the surface of an object by multiple triangles, which are all connected by edges, as seen in Figure 3-8. Here, an arbitrary triangle of the surface model of the asteroid is taken and enlarged. The distances are considered with respect to an arbitrary point in the asteroid reference frame. Based on the total volume that is encompassed by the polyhedron shape, the gravitational force of the body can be computed. The gravity potential as derived by Werner and Scheeres (1996) is defined as

$$U = \frac{1}{2}G\sigma \sum_{e\in \text{ edges}} \mathbf{r}_e^T \mathbf{E}_e \mathbf{r}_e L_e - \frac{1}{2}G\sigma \sum_{f\in \text{ faces}} \mathbf{r}_f^T \mathbf{E}_f \mathbf{r}_f \omega_f \tag{3-40}$$

where G is the gravitational constant, σ is the mean density, $\mathbf{r}_e$ and $\mathbf{r}_f$ are the distances from a field point to an edge and to a face respectively.

L_e is dimensionless and equal to

$$L_e \equiv \int_e \frac{1}{r}\,\mathrm{d}s = \int_{P_i}^{P_j} \frac{1}{r}\,\mathrm{d}s = \ln\left(\frac{r_i + r_j + e_{ij}}{r_i + r_j - e_{ij}}\right). \tag{3-41}$$

where r_i and r_j are the absolute values of the vectors from the origin to the corners of the polyhedron, $\mathbf{r}_i$ and $\mathbf{r}_j$ respectively. This can be seen in Figure 3-9, where P_i and P_j are vertices with distance e_{ij}.

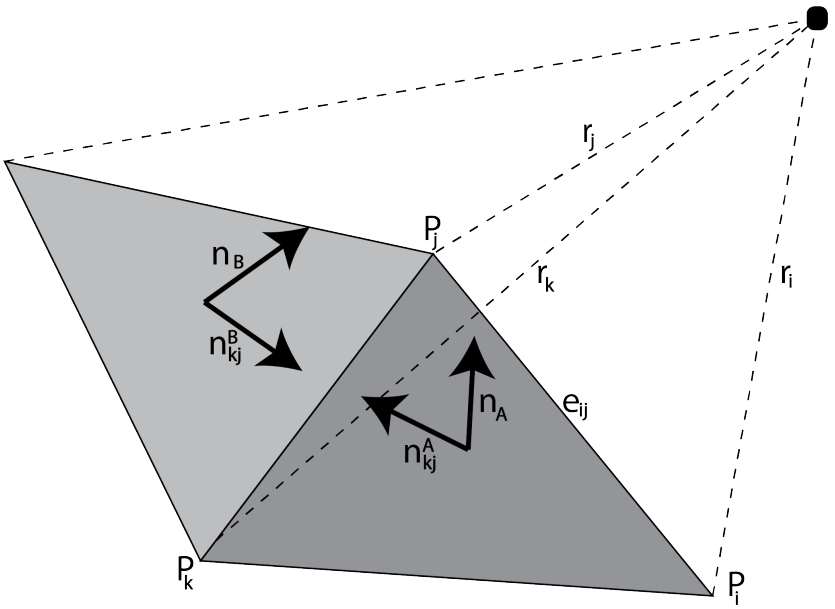

Figure 3-9: Visualisation of Polyhedron triangles.

Next, ω_f is also dimensionless, and defined as

$$\omega_f = \iint_{\text{triangle}} \frac{\Delta z}{r^3}\,\mathrm{d}S = 2\arctan\left(\frac{\mathbf{r}_i^T\mathbf{r}_j \times \mathbf{r}_k}{r_i r_j r_k + r_i\left(\mathbf{r}_j^T\mathbf{r}_k\right) + r_j\left(\mathbf{r}_k^T\mathbf{r}_i\right) + r_k\left(\mathbf{r}_i^T\mathbf{r}_j\right)}\right), \tag{3-42}$$

where r_k is the absolute value of vector $\mathbf{r}_k$, which is the third vector from the origin to a corner of the polyhedron. Next, $\mathbf{E}_e$ is defined as

$$\mathbf{E}_e = \mathbf{n}_A(\mathbf{n}_{kj}^A)^T + \mathbf{n}_B(\mathbf{n}_{kj}^B)^T, \tag{3-43}$$

where the superscripts A and B refer to faces A and B respectively, where surface A and B are connected to each other by one edge. Then, $\mathbf{n_A}$ is the normal vector, $\mathbf{n_e}$ is the edge vector and face dyad $\mathbf{E}_f$ for face A is equal to $\mathbf{n}_A(\mathbf{n}_A)^T$. By computing the potential for each surface triangle and summing them, a detailed gravity potential and acceleration can be generated, taking into account all surface features of the asteroid.

3-4-2 Disturbance Force Modelling

The resulting orbit due to the gravitational force of 433 Eros is considered the initial orbit. Any other forces taken into account that are exerted on the spacecraft are then considered disturbance forces, as they can cause the orbit to become (more) unstable. To begin with, a perturbation due to the mass of the Sun is considered, as well as one due to the effects of SRP. Any atmospheric drag is not considered as there is no atmosphere present around any asteroid (Lissauer and de Pater, 2013), including 433 Eros. Razgus (2016) incorporated a model for the gravity gradient torque as a disturbing force in addition to the SRP and the gravitational force exerted by the Sun. However, the model had a large computational error when verifying the model for the gravity gradient torque, which could only be improved using computationally exhaustive operations. Furthermore, the torque values ranged in the order of 10^{-4} to 10^{-3} Nm.

Whereas the spacecraft considered by Razgus (2016) had two large solar panels extending from the sides of the main body, the current considered spacecraft is symmetric about the x- and y-axis and has much shorter solar panels. It is expected that the other simulated disturbance forces have more effect on the propagation of the spacecraft, such that the gravity gradient torque is omitted. For the same reason, any disturbances due to gravitational forces by other celestial bodies have been neglected. By doing so, the performance of the navigation filter will appear better than it actually is. It is possible to consider the gravitational forces exerted by the planets in the solar system. However, we don't assume to have a visual on celestial bodies in the solar system other than 433 Eros and the Sun, and sensors such as accelerometers can only measure non-gravitational forces. Therefore, it is not possible to provide measurements that supply information on the additional gravitational forces exerted on the spacecraft. In a scenario where the planets would be simulated for the spacecraft environment, it is thus only possible for the navigation filter to use an approximation in the time update to estimate the additional gravitational forces. These approximations cannot be corrected with a measurement update. By omitting the simulation of other celestial bodies and their gravitational force exerted on the spacecraft, the true state model is simplified and we don't have to account for other disturbance forces. However, this means we have to take the performance of the navigation filter with a grain of salt, as we can expect that the accuracy of the state estimation will decrease when more disturbance forces are simulated.

Third Body Perturbation

The Sun is considered as the third body, P_3, in addition to the previously mentioned two-body problem. For a three-body problem, the equation of motion becomes

$$\frac{d^2\mathbf{r}_1}{dt^2} = G\frac{m_2}{r_{12}^3}\mathbf{r}_{12} + G\frac{m_3}{r_{13}^3}\mathbf{r}_{13}, \tag{3-44}$$

which, if expressed with the gravitational parameters, becomes

$$\frac{d^2\mathbf{r}_1}{dt^2} = \frac{\mu_2}{r_{12}^3}\mathbf{r}_{12} + \frac{\mu_3}{r_{13}^3}\mathbf{r}_{13}. \tag{3-45}$$

Solar Radiation Pressure

There are multiple methods for approximating SRP effects on the dynamics and kinematics of a spacecraft, such as the cannonball, the (multi-body) flat-plate, or the N-plate model. As demonstrated by Jean et al. (2019), the cannonball model 'does not take into consideration the attitude of the spacecraft in its calculation' and is therefore not suitable for approximating the effects on both the position and attitude by the SRP. Although a multi-body flat plate model can take into account different reflectivity properties by considering multiple panels to make up the exterior of the spacecraft, it does not take different masses of the panels into account. The N-plate model does take different panel masses into account, resulting in different results from the multi-body flat plate model. According to Jean et al. (2019), these differences become more apparent with more complex attitude kinematics, without noticeable increase in computational effort. Therefore, the N-plate model is chosen to approximate the SRP effect on the spacecraft. Using this model, the effect of the chosen spacecraft design and its mass distribution on the resulting SRP force and acceleration are taken into account.

According to Montenbruck and Gill (2000), the perturbing force exerted on a spacecraft due to SRP can be expressed as

$$\boldsymbol{F}_{SRP} = -P_{\odot}\cos(\theta)A\left((1-\epsilon)\boldsymbol{e}_{\odot} + 2\epsilon\cos(\theta)\boldsymbol{n}\right) \tag{3-46}$$

where $\cos(\theta)A$ is the cross-section of the bundle of light that illuminates a surface of size A. $(1-\epsilon)\boldsymbol{e}_{\odot}$ represents the term due to absorption of the light where ϵ is the emissivity of the illuminated surface and $\boldsymbol{e}_{\odot}$ is a unit vector pointing directly to the Sun. The remaining term, $2\epsilon\cos(\theta)\boldsymbol{n}$, is due to reflected Sunlight, where the momentum of the light is doubled compared to absorbed light. $\boldsymbol{n}$ is the unit vector indicating the orientation of the illuminated surface. The solar pressure constant, $P_{\odot}$, is equal to

$$P_{\odot} = \frac{\Phi}{c} \approx 4.56 \cdot 10^{-6}\mathrm{N/m}^2 \tag{3-47}$$

where Φ is the solar flux at a distance 1 AU from the Sun and c is the speed of light. Taking into account that the solar flux changes proportional to the square of the distance to the Sun and that the spacecraft consists of multiple illuminated surface with their own mass, area, orientation and reflectivity, the equation for the resulting acceleration due to SRP is equal to

$$\boldsymbol{a}_{SRP} = -P_{\odot}\frac{1AU^2}{r_{\odot}^2}\sum_{i=1}^{N}\cos(\theta_i)\frac{A_i}{m_i}\left((1-\epsilon)\boldsymbol{e}_{\odot,i} + 2\epsilon\cos(\theta_i)\boldsymbol{n}_i\right) \tag{3-48}$$

where $r_{\odot}$ is the absolute distance from the spacecraft to the Sun, and i denotes the ith of N panels of the spacecraft. Any effects on the acceleration due to eclipse or shadow effects have been neglected.

The torque due to the SRP can be computed using

$$\boldsymbol{\tau}_{SRP} = \sum_{i=1}^{N}\mathbf{r}_i \times \mathbf{F}_{i,SRP} \tag{3-49}$$

where $\mathbf{r}_i$ is the distance from the middle of a panel to the origin of the spacecraft reference frame and $\mathbf{F}_{i,SRP}$ is the force exerted on each panel.

3-5 Spacecraft Kinematics

The propagation of the kinematics of the spacecraft will be expressed using quaternions. For a given attitude, the propagation is defined as

$$\dot{\mathbf{q}}_{B/I}(t) = \frac{1}{2}\boldsymbol{\omega}^B_{B/I}(t) \otimes \mathbf{q}_{B/I}(t) = \frac{1}{2}\Omega(\boldsymbol{\omega}(t)^B_{B/I})\mathbf{q}(t), \tag{3-50}$$

where function $\Omega(\boldsymbol{\omega})$ is defined as

$$\Omega(\boldsymbol{\omega}) = \begin{bmatrix} -[\boldsymbol{\omega}\times] & \boldsymbol{\omega} \\ -\boldsymbol{\omega}^T & 0 \end{bmatrix} = \begin{bmatrix} 0 & \omega_3 & -\omega_2 & \omega_1 \\ -\omega_3 & 0 & \omega_1 & \omega_2 \\ \omega_2 & -\omega_1 & 0 & \omega_3 \\ -\omega_1 & -\omega_2 & -\omega_3 & 0 \end{bmatrix}. \tag{3-51}$$

Based on the relations described by Wie (2008), the relation between the angular momentum, torque and rotation of the spacecraft is

$$\dot{\mathbf{H}}_B + \boldsymbol{\omega}^B_{B/I} \times \mathbf{H}_B = \mathbf{T}_B. \tag{3-52}$$

The relation between the rotation, rotation rate, and torque is then defined as

$$\dot{\boldsymbol{\omega}}^B_{B/I} = I^{-1}(-\boldsymbol{\omega}^B_{B/I} \times (I\boldsymbol{\omega}^B_{B/I}) + \mathbf{T}_B. \tag{3-53}$$

Chapter 4

Design and Simulation of True State Propagation

In this chapter, the previously described dynamics and kinematics will be translated to a simulation model of the spacecraft and its environment. The general architecture of the software model will be presented in Section 4-1. The methods to obtain the true state for the navigation problem will be described, simulated and verified. To begin with, the spacecraft model is presented in Section 4-2, and the environment model in Section 4-3. After, the benchmark scenario of the simulation is presented in Section 4-4, which allows for verification of the simulation model in Section 4-5.

4-1 Algorithm Architecture

The algorithm to model and compute polyhedron gravitational acceleration was derived by Werner and Scheeres (1997), and duplicated by Razgus (2016) in a Simulink environment. An overview of the architecture can be found in Figure 4-1. The initialisation blocks are rounded rectangles, the essential outputs needed for the state estimation are denoted as ellipses, and the function blocks are presented as ordinary rectangles. The position and velocity can be directly derived from the computed by integrating the resulting acceleration for each time step.

It can be seen that SRP and gravitational forces exerted by the Sun (point mass) and 433 Eros (polyhedron model) will be included to propagate the dynamics and kinematics of the spacecraft. Furthermore, the relation of the kinematic to the dynamic equations has been clarified.

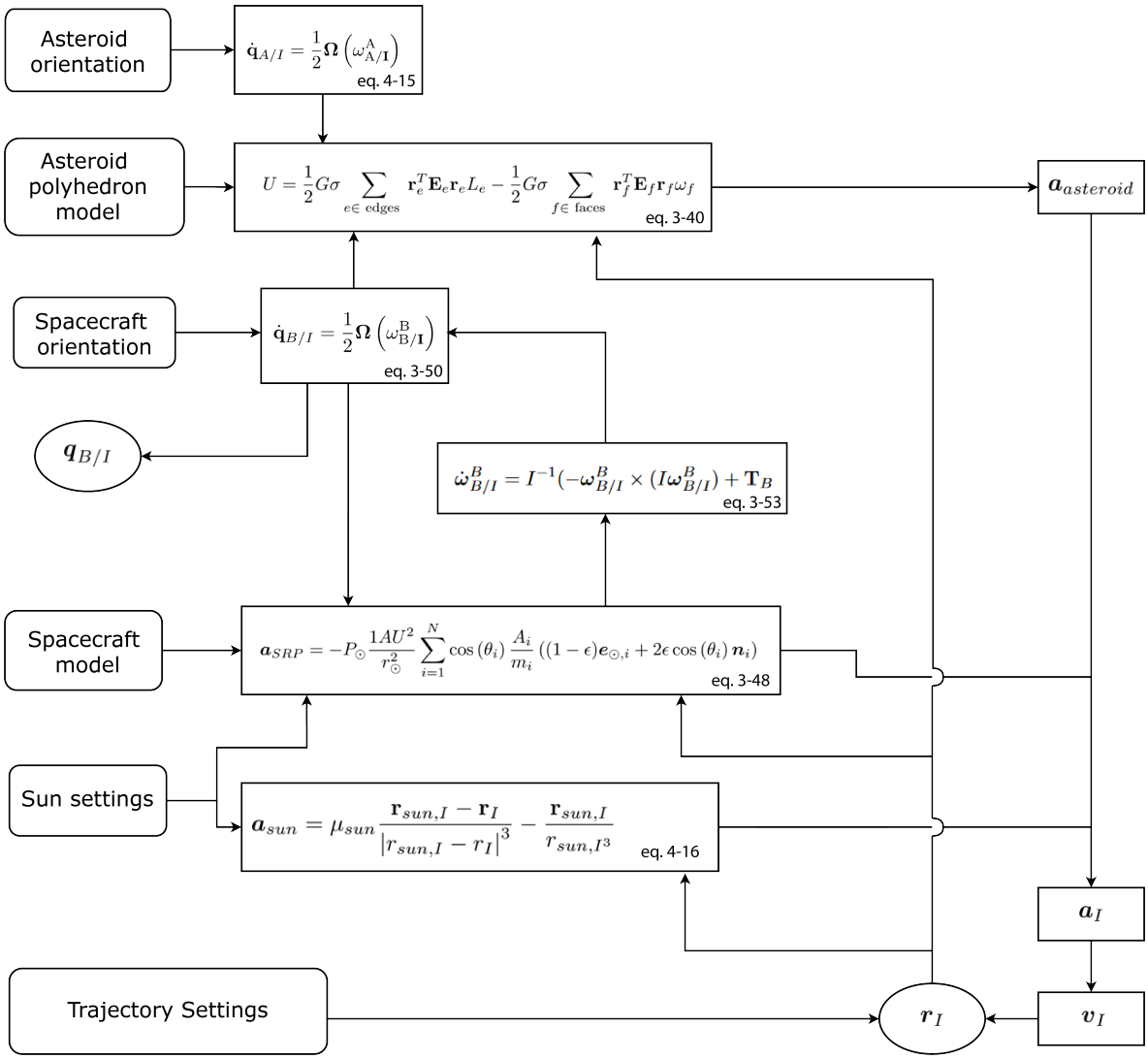

Figure 4-1: Architecture of true state simulation.

4-2 Spacecraft Model Initialisation

Before computing the dynamics and kinematics of the spacecraft and the asteroid, the characteristics of the spacecraft need to be initialised. A visualisation of the body is displayed in Figure 4-2. The solar panels have been mounted on the top of the spacecraft body in a windmill configuration, with their short sides attached to the main body.

The initialisation of the spacecraft body has been done using the properties of the Near Earth Asteroid Rendezvous (NEAR) spacecraft described by Santo et al. (1995). An overview of the dimensional and mass properties of the spacecraft can be found in Table 4-1 and Table 4-2 respectively. Here, the subscript b denotes the spacecraft body, and the subscript sp denotes the characteristic of one solar panel.

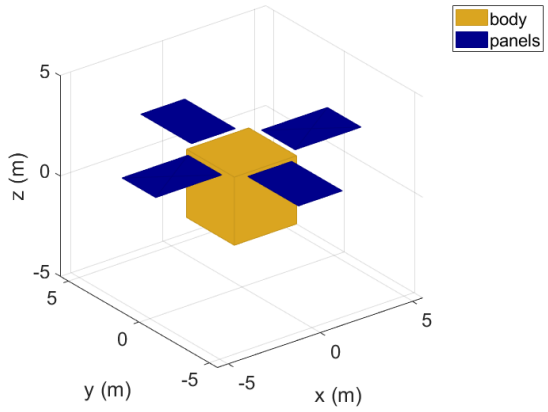

Figure 4-2: Spacecraft Model.

Table 4-1: Sizing properties based on the NEAR-shoemaker design (Santo et al., 1995).

Dimension	Value [m]
l_b	1.7
w_b	1.7
h_b	1.7
l_{sp}	1.8
w_{sp}	1.2

Table 4-2: Mass properties based on the NEAR-shoemaker design (Santo et al., 1995).

Mass	Value [kg]
m_{total}	487
m_b	302.6
m_{sp}	46.1

4-2-1 Mass Moment of Inertia

Next to the mass and dimensional properties of the spacecraft, the mass moment of inertia (MMOI) needs to be determined. The MMOI is needed in order to compute torques induced on the spacecraft, as can be seen in Subsection 4-3-2. As the spacecraft body centre is coinciding with the origin of the spacecraft reference frame B, the MMOI computation is straightforward using

$$\mathbf{I}_{\mathrm{b}} = \begin{bmatrix} \frac{1}{12} m_b \left(w_b^2 + h_b^2\right) & 0 & 0 \\ 0 & \frac{1}{12} m_b \left(l_b^2 + h_b^2\right) & 0 \\ 0 & 0 & \frac{1}{12} m_b \left(w_b^2 + l_b^2\right) \end{bmatrix}, \tag{4-1}$$

where m_b is the mass of the spacecraft body, x_b, y_b, and z_b are the dimensions of the body in the x-, y-, and z-direction respectively.

The computation for the solar panels is performed slightly different. Using cut-out theory, consider one long solar panel extending from two panels placed opposite from each other on the spacecraft. By first computing the MMOI for the long panel and then subtracting the MMOI of the 'inner' part between the actual panels, the MMOI can be computed without the need for parallel axes additions. Assuming homogeneous weight distribution, the masses of the extended solar panel and the middle part can be computed as

$$m_{cutout} = \frac{m_{sp}}{l_{sp} w_{sp}} l_{sp} l_b = 43.5389\text{kg}, \tag{4-2}$$

$$m_{longpanel} = m_{cutout} + 2 * m_{sp} = 135.7389\text{kg}, \tag{4-3}$$

where m_{cutout} is the middle part that extends over the top of the spacecraft body and $m_{longpanel}$, with dimensions 1.2m×1.7m and 1.2m×5.3m respectively. The distance from the actual x- and y-axis from the plane of the solar panels, denoted as d_x and d_y, are then equal to

$$d_x = \frac{l_b}{2} = 0.85\text{m}, \tag{4-4}$$

$$d_y = \frac{w_b}{2} = 0.85\text{m}. \tag{4-5}$$

The long panel mass moments of inertia are then computed as

$$I_{longpanel,x} = \frac{m_{sp}}{6}(l_{sp}^2) + 2m_{sp}d_y^2 + \frac{m_{sp}}{12}(2w_{sp} + w_b)^2 + m_{longpanel}d_y^2, \tag{4-6}$$

$$I_{longpanel,y} = \frac{m_{sp}}{6}(l_{sp}^2) + 2m_{sp}d_x^2 + \frac{m_{longpanel}}{12}(2w_{sp} + l_b)^2 + m_{longpanel}d_x^2, \tag{4-7}$$

$$I_{longpanel,z} = \frac{m_{longpanel}}{6}((2w_{sp} + w_b)^2 + l_{sp}^2), \tag{4-8}$$

and for the cutout of the panel as

$$I_{cutout,x} = \frac{m_{cutout}}{12}(w_b)^2 + m_{cutout}d_y^2, \tag{4-9}$$

$$I_{cutout,y} = \frac{m_{cutout}}{12}(l_b)^2 + m_{cutout}d_x^2, \tag{4-10}$$

$$I_{cutout,z} = \frac{m_{cutout}}{6}(w_b^2 + l_{sp}^2). \tag{4-11}$$

In total, the MMOI of the solar panels can be computed by subtracting the cutout MMOI from the MMOI of the long panel by

$$\mathbf{I}_{sp} = \mathbf{I}_{longpanel} - \mathbf{I}_{cutout} = \begin{bmatrix} 451.5495 & 0 & 0 \\ 0 & 451.5495 & 0 \\ 0 & 0 & 636.6410 \end{bmatrix}, \tag{4-12}$$

after which it can be added to the MMOI of the main body, which gives

$$\mathbf{I} = \mathbf{I}_b + \mathbf{I}_s = \begin{bmatrix} 597.3018 & 0 & 0 \\ 0 & 597.3018 & 0 \\ 0 & 0 & 782.3933 \end{bmatrix}. \tag{4-13}$$

An overview of all MMOI values is found in Table 4-3.

Table 4-3: Mass Moment of Inertia Spacecraft.

Main body		
$I_{b,x}$	145.7523	kg m^2
$I_{b,y}$	145.7523	kg m^2
$I_{b,z}$	145.7523	kg m^2
Solar panels		
$I_{sp,x}$	451.5495	kg m^2
$I_{sp,y}$	451.5495	kg m^2
$I_{sp,z}$	636.6410	kg m^2
Total		
$I_{x,total}$	597.3018	kg m^2
$I_{y,total}$	597.3018	kg m^2
$I_{z,total}$	782.3933	kg m^2

4-2-2 Reflectivity Model

Since the exterior of the spacecraft consists of different parts, the reflectivity is different per panel. What's more, is that not every panel is illuminated by the Sun at the same instant. In order to configure which parts of the spacecraft are in direct Sunlight, a reflectivity model is set up. Recall Equation 3-48 where the SRP acceleration is dependent on the incoming angle of the Sunlight onto on of the spacecraft panels. Therefore, the normal vector $\boldsymbol{n}_i$ is computed beforehand for each panel with respect to the spacecraft reference frame. The normal vector and the reflectivity per panel are presented in Table 4-4. Note that for the solar panels, a front and a back panel are considered as they have a different reflectivity characteristic.

Table 4-4: Spacecraft reflectivity properties (Montenbruck and Gill, 2000).

Panel	Normal vector $\boldsymbol{n}_i$	reflectivity	Panel	Value	reflectivity
1	$[0\ 0\ 1]^T$	0.5	8	$[0\ 0\ 1]^T$	0.21
2	$[0\ 0\ -1]^T$	0.5	9	$[0\ 0\ -1]^T$	0.5
3	$[-1\ 0\ 0]^T$	0.5	10	$[0\ 0\ 1]^T$	0.21
4	$[0\ -1\ 0]^T$	0.5	11	$[0\ 0\ -1]^T$	0.5
5	$[1\ 0\ 0]^T$	0.5	12	$[0\ 0\ 1]^T$	0.21
6	$[0\ 1\ 0]^T$	0.5	13	$[0\ 0\ -1]^T$	0.5
7	$[0\ 0\ -1]^T$	0.5	14	$[0\ 0\ 1]^T$	0.21

4-3 Environment Model Initialisation

The benchmark scenario describes the half of an orbital revolution of the spacecraft around the asteroid, if seen from the inertial reference frame. As orbit of the spacecraft has an orbital height of 50 km, the orbital period is roughly 106098.6 seconds, which for simplicity will be rounded to 106100 seconds, or 29.5 hours. For the benchmark scenario, this translates to 53050 seconds. Half an orbit has been selected to save simulation time, as it is expected that half an orbit can provide the same insights as gained during a full orbit. Thus, the research questions can still be answered to the same extent but with less simulation time.

4-3-1 Asteroid Model Set-up

The primary object in the simulation environment of the spacecraft is the asteroid 433 Eros. The asteroid is initialised using the properties visible in Table 4-5.

Table 4-5: Physical characteristics for 433 Eros, taken from Santo et al. (1995), Miller et al. (2002).

Parameter	Value	Unit
Mass	$6.5684 \cdot 10^{15}$	kg
ρ	2621.2	kg/m^3
Volume	$2.5059 \cdot 10^{12}$	m^3
Area	$1.1273 \cdot 10^{9}$	m^2
μ	$4.3838 \cdot 10^{5}$	m^3/s^2

Next, the model for the polyhedron gravity computation is presented and verified. After, the asteroid kinematics with respect to the inertial frame are described.

Polyhedron Model

As previously described in Subsection 3-4-1, the gravity of the asteroid will be estimated using a polyhedron model. The polyhedron model from 433 Eros is based on the data model by Gaskell (2008). Whereas the model from Gaskell (2008) has a total of 49152 faces to characterise the surface, a simplified model of 5144 is used in order to reduce computational effort. In Figure 4-3, a 3D view as well as all the views in the three different planes of the simplified 433 Eros model can be seen.

The volume of the simplified model is 0.02% less than the volume of the original model, however the computational efforts are reduced as ten times less faces are generated. As the position of the spacecraft with respect to each face and vertex is computed each time step, the current simulation time for the simulation of half an orbit already extends to a couple of hours. Hence, a full model simulation cannot be realised within the time scope of the research.

Asteroid Kinematics

The orbit of the asteroid around the Sun is not taken into account, as the benchmark scenario described in Section 4-4 has duration of less than 15 hours, and is therefore considered negligible. Any other influence of the Sun on the asteroid is therefore also omitted from the model.

Although a slight wobble was determined in the rotation rate of the asteroid per day (Miller et al., 2002), these offsets were never greater than 0.00015 deg over the course of a day. Therefore, the asteroid is assumed to have a constant rotation about its z-axis. Hence, within the attitude of the asteroid, as well as the asteroid reference frame, is initialised as

$$\mathbf{q}_{A/I} = \begin{bmatrix} 0 \\ 0 \\ 0 \\ 1 \end{bmatrix}, \tag{4-14}$$

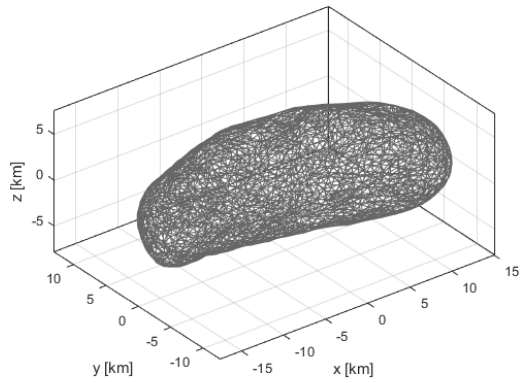

(a) 3D view of 433 Eros model.

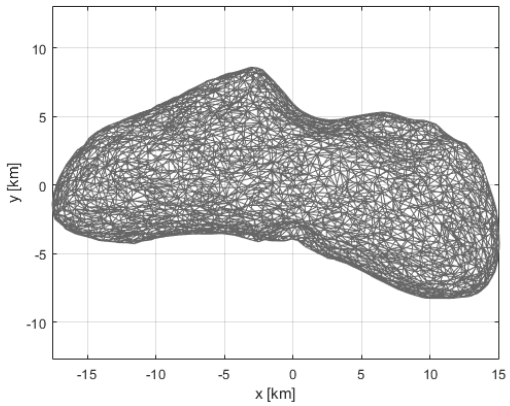

(b) xy-plane view of 433 Eros model.

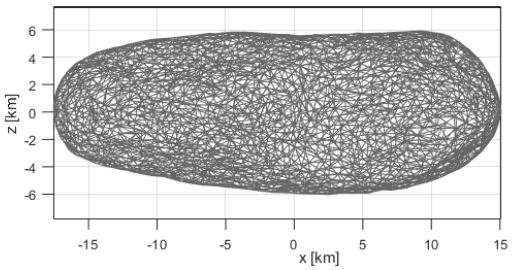

(c) xz-plane view of 433 Eros model.

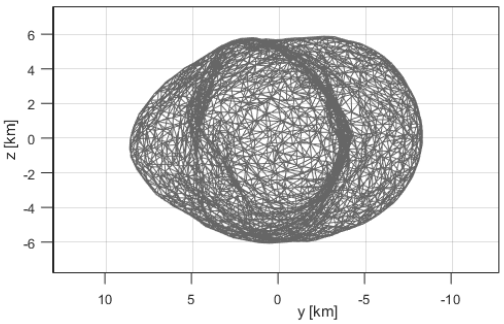

(d) yz-plane view of 433 Eros model.

Figure 4-3: Different views of a simplified Polyhedron model approximation of the exterior of 433 Eros in inertial reference frame, based on the model provided by Gaskell (2008).

and the rotation of frame A with respect to frame I is equal to the rotation rate as defined in Equation 3-38. The attitude is then propagated using

$$\dot{\mathbf{q}}_{A/I} = \frac{1}{2}\Omega(\omega^A_{AI}). \tag{4-15}$$

4-3-2 Disturbance Force Computation

As the simulated disturbance forces on the spacecraft orbit are caused by the Sun, its properties are first presented, after which the models for the third body perturbation and the SRP force are presented.

In Table 4-6, the parameters of the Sun have been listed, and a distance from the Sun to the inertial frame is determined.

Table 4-6: Parameters Sun Simulation.

Parameter	Value	Unit
G	$6.67408 \cdot 10^{-11}$	m^2/kg^2
Flux at 1 AU	1361	W/m^2
Position (inertial frame)	$\begin{bmatrix} 1.40592984439860 \\ 1.364241144552538 \\ 1.028981919188861 \end{bmatrix} \cdot 10^{11}$	m
Absolute distance to inertial frame	$2.2128 \cdot 10^{11}$	m
Flux (at origin inertial frame)	622.0347	W/m^2
Mass	$1.988 \cdot 10^{30}$	kg
μ_{Sun}	$1.3268 \cdot 10^{20}$	m^3/s^2

Third Body Perturbation Model

Implementation of the third body disturbance by the Sun is relatively straightforward, using Equation 3-45, expressed in the algorithm as

$$\mathbf{a}_{Sun} = \mu_{Sun} \frac{\mathbf{r}_{Sun,I} - \mathbf{r}_I}{|r_{Sun,I} - r_I|^3} - \frac{\mathbf{r}_{Sun,I}}{|r_{Sun,I^3}|}, \tag{4-16}$$

where $|r_{Sun,I} - r_I|$ is the absolute value of the distance between the position of the Sun and the position of the spacecraft in the inertial reference frame.

Solar Radiation Pressure Model

To start with, the position of the Sun with respect to the spacecraft reference frame is computed using

$$\mathbf{r}_B^S = C(\mathbf{q}_{B/I})\mathbf{r}_I^S, \tag{4-17}$$

such that the unit vector per spacecraft panel pointing to the Sun, $e_{\odot,i}$, can be computed as well. Combined with the unit vector normal to each spacecraft panel,$\mathbf{n}_i$, the relation

$$\cos(\theta_i) = \mathbf{n}_i^T e_{\odot,i}, \tag{4-18}$$

is obtained. As the mass and area of each panel is also known, Equation 3-48 can be readily used to complete the computation. As the force is computed with respect to the asteroid reference frame and the propagation of the states is performed in the inertial frame, the acceleration is expressed in the inertial frame

$$\mathbf{a}_{srp,I} = C((\mathbf{q}_{B/I})^{-1})\mathbf{a}_{srp,B}. \tag{4-19}$$

4-3-3 Orbit Initialisation

As the spacecraft is assumed to be in orbit at 50 km from the asteroid in the benchmark scenario, the spacecraft reference frame initial position is set at 50 km in the x-direction. By assuming that the sensor(s) for asteroid observation are positioned at the bottom side of the

spacecraft, the spacecraft reference frame is initialised with the z-axis pointed at the inertial reference frame origin. The configuration can be seen in Figure 4-4, where the main body, solar panels, and the three axes are all visible. The z-axis is pointing nadir, the x- and y-axis are in line with the solar panels, which is the result of a 90 degree rotation about the y-axis. The y-axis is tangent to the orbital path of the satellite. The configuration with respect to the asteroid is shown in Section 4-4.

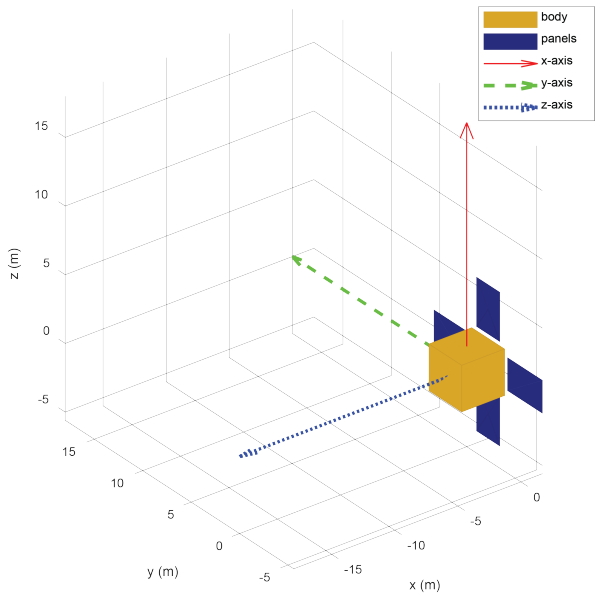

Figure 4-4: Spacecraft configuration in the inertial frame.

Based on the Keplerian orbital elements in the top part of Table 4-7, the orbital dynamics can be derived. Below, the properties of the orbit initialisation are listed, defined in the inertial reference frame. As the spacecraft body frame is tilted such that the x-axis is pointing upwards, a constant angular rate of the spacecraft about the x-axis is introduced, to maintain a visual on the asteroid during the orbit.

Thus, the orbit is starting in the hypothetical pericentre, when looking at the angles of the Kepler coordinates. However, as the eccentricity is 0, the orbit is circular and thus the starting point is arbitrary to the Kepler annotation.

4-4 Simulation Benchmark Scenario

In this section, the results of the benchmark simulation are presented and pose as a starting point for the simulation of the sensor set of the spacecraft in the next chapter. Thus, the benchmark can be viewed as the true simulation which the sensor fusion algorithm should be able to measure during the mission scenario. The trajectory of the spacecraft is propagated for half an orbit, with a duration of 53050 s and a time step of 0.01 s. For the benchmark simulation,

- the SRP effect from the Sun is included;

Table 4-7: Initialisation parameters for simulation of half orbital period at 50 km orbit around 433 Eros.

Parameter	Value	Unit
a	50	[km]
e	0	[-]
i	0	[deg]
Right ascension of the ascending node	0	[deg]
Argument of perigee	0	[deg]
Position x-axis	50.000	[km]
Position y-axis	0	[km]
Position z-axis	0	[km]
Velocity x-axis	0	[m/s]
Velocity y-axis	2.9610136	[m/s]
Velocity z-axis	0	[m/s]
Angular rate ω_{BI}^{B} x-axis	$5.9220\times\ 10^{-5}$	[rad/s]
Angular rate ω_{BI}^{B} y-axis	0	[rad/s]
Angular rate ω_{BI}^{B} z-axis	0	[rad/s]
Quaternion attitude q_{BI}	$\begin{bmatrix}0 & -0.7071 & 0 & 0.7071\end{bmatrix}^T$	[-]
Euler angles BI	$\begin{bmatrix}0 & -1.5707963 & 0\end{bmatrix}^T$	[rad]

- the third body perturbation of the Sun is included;
- the asteroid was implemented as a polyhedron.

A visualisation of the mission scenario can be seen in Figure 4-5. Added to the position plot are plots of the spacecraft and its reference frame, enlarged by 200 times, at five time stamps during the simulation: at the start, at 25%, 50%, 75%, and 100%. It can be seen that the spacecraft follows the trajectory of half an orbit. Initially, the spacecraft was set to have a constant rotation about the x-axis in order to align the z-axis and the y-axis of the spacecraft reference frame with the radial and tangential of the orbit respectively. However, it can be seen that the spacecraft rotation is not constant about the z-axis. This is due to a combination of the disturbance forces and the different influence of the polyhedron model gravity compared to an orbit trajectory around a point mass. Additional figures on the propagation of the benchmark scenario can be found in Appendix C.

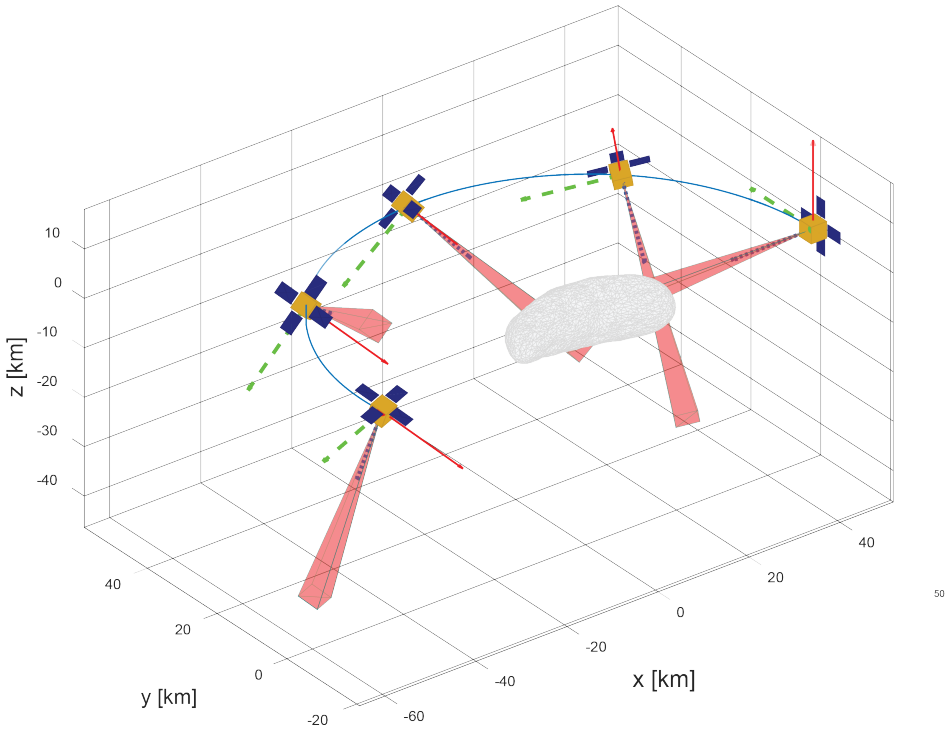

Figure 4-5: Position for half orbit at 50 km counterclockwise around 433 Eros, and attitude of spacecraft (enlarged to 200x actual size) at 0%, 25%, 50%, 75%, and 100% of simulation time, in the inertial reference frame.

4-5 Benchmark Verification

This section is introduced to verify the true state simulation of the propagation of the position, velocity, and attitude of the spacecraft. The verification is done in multiple steps. To start with, the model without any disturbance forces or the asteroid polyhedron model is verified. By running the true state simulation with an Euler integration method (ode1) in Simulink, the same results should be obtained as for running the same equations in a discrete time state space model in the inertial reference frame. After, the asteroid polyhedron model and the different disturbance forces are verified.

4-5-1 Asteroid Point-Mass Model

For the verification of the dynamics of the true state simulation, assuming a point-mass model for 433 Eros, a state space model is considered for comparison. In this state space model, the position, velocity, acceleration and attitude of the spacecraft in the inertial frame are the propagated states using only a state space update. Where the acceleration in the true state simulation is computed in the asteroid reference frame and then transformed to the inertial reference frame, the acceleration computed for the verification model is directly computed in the inertial reference frame. All other equations used in both models should be identical and therefore their outcomes should be the same. In order to verify that this is indeed the case, the models are both run on different time step sizes, ranging from 100 s to 0.01 s. Especially

for the small step sizes, it should be expected that only errors caused by machine precision residuals should be observed.

During this simulation,

- the SRP effect from the Sun was **not** included;
- the third body perturbation of the Sun was **not** included;
- the asteroid model is approximated as a **point mass**.

Although the true state simulation model was largely based on an environment model described by Razgus (2016), some alterations were made. For a point mass gravity assumption, computing the acceleration in the asteroid reference frame and converting the results to the inertial reference frame should give the same results as directly computing the acceleration in the inertial reference frame. However, during verification it was found that the true state simulation and the verification model gave a different result for the position estimation in the inertial frame. This meant that the reference frame transformation was not correctly implemented. Therefore, the rotation matrices between the asteroid reference frame and the spacecraft reference frame as presented by Razgus (2016) were revised, such that both models gave the same outcome for a point mass assumption for the asteroid.

The resulting model was then again verified with respect to the state space propagation. It was observed that the error difference for the position, velocity and orientation estimates were in the order of 10^{-11}, 10^{-15}, and 10^{-16} respectively. Thus, any errors between the outputs of the two models are likely due to the limitations of the finite precision arithmetic. Although these errors are usually of a higher order, the position is based on the integration of the acceleration for the true state simulation, for which the errors were in the order of 10^{-19}. Nonetheless, errors of these orders as displayed in Figure C-2 and Figure C-3 are negligible for the true state simulation.

4-5-2 Asteroid Polyhedron Model

For the implementation of the polyhedron model, the generation of the asteroid model shape was first verified. The model, as seen in Figure 4-3, could be verified with respect to same homogeneous density model that was computed and verified by Spee (2022). In Figure 4-6, the gravity field has been plotted for the xy-plane.

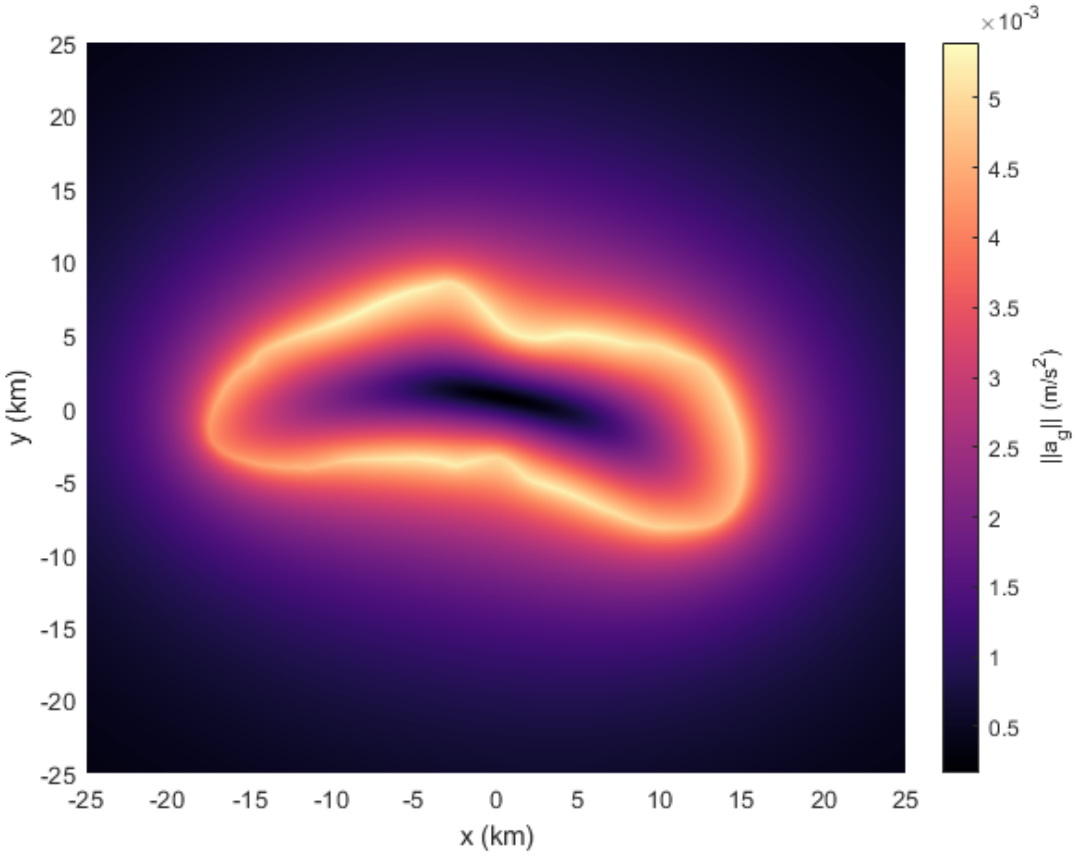

Figure 4-6: Polyhedron gravity field of 433 Eros in the xy-plane.

From this figure, the same properties of the gravity field could be found as for the gravity field for the homogeneous mass density model of Spee (2022). This concludes that the gravity field model is verified.

4-5-3 Third Body Disturbance

By adjusting the model settings from Subsection 4-5-1 to now include the third body disturbance, and adding the equivalent formula to the state space update, the disturbance can be verified. In Figure 4-7a, the initial offset between the two models can be seen. As there is no influence on the attitude by introducing the third body disturbance, it is not shown. For the implementation of the third body disturbance in the state space propagation model, the offsets for the position can be seen in Figure 4-7b.

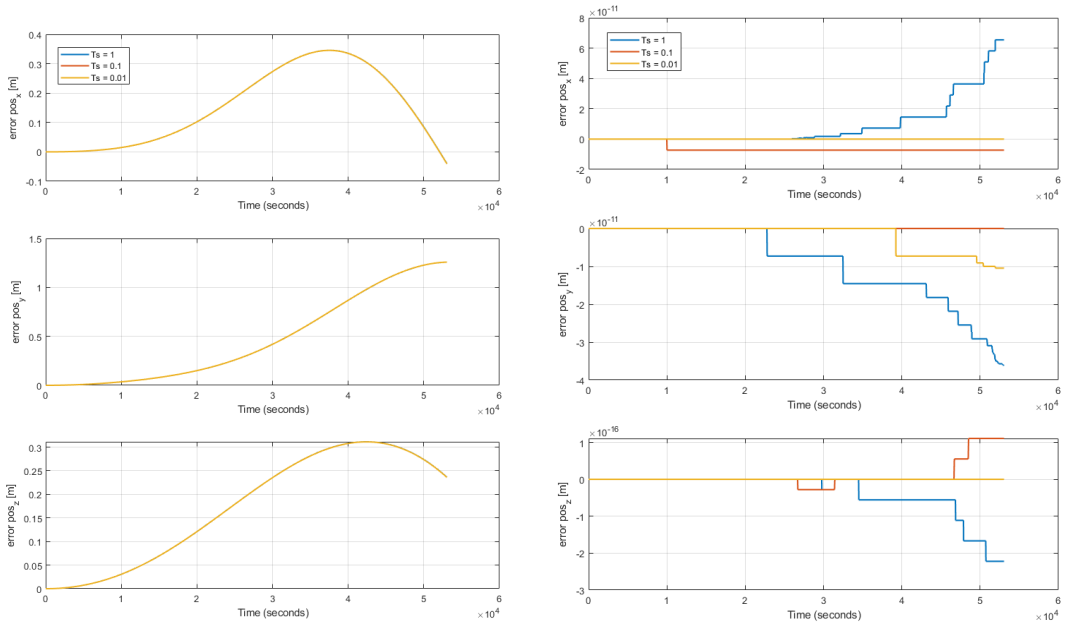

(a) Position error between true state simulation with third body disturbance and state space update, for time steps 1s, 0.1s, 0.01 in the inertial frame.

(b) Position error between true state simulation and state space update, both with third body disturbance, for time steps 1s, 0.1s, 0.01 in the inertial frame.

Figure 4-7: Errors between true state simulation and state space update, with and without third body modelling.

In Figure 4-7a it is seen that the third body perturbation causes an offset from the true state simulation with only an asteroid point-mass approximation. The deviation is in the order of a meter over half an orbit. A new state space model is set up for verification, which includes a point mass approximation of 433 Eros as well as the Sun. As seen in Figure 4-7b it can be seen in that the errors between the two models are again negligibly small.

4-5-4 Solar Radiation Pressure

The acceleration due to the SRP cannot be directly implemented in a state space system. However, it is possible to verify the propagation of the acceleration. The variation equations due to SRP given by Wakker (2015) are equal to

$$\begin{aligned} |\Delta i|_{\max} &= \frac{a_{srp}}{n_0^2 r_0} \sin(\alpha_0), \\ |\Delta \Omega|_{\max} &= 2\frac{a_{srp}}{n_0^2 r_0} \sin(\alpha_0), \end{aligned} \tag{4-20}$$

where a_{srp} is the acceleration due to the SRP, n_0 is the mean notion in orbit, r_0 is the orbit radius, and α_0 is the angle between the orbital direction vector of the Sun.

It could be deduced from the verification by Razgus (2016), that the deviations of the inclination angle, i and the right ascension of the ascending node, Ω, display constant sinusoidal behaviour, for a constant distance to the Sun. For the verification, a point mass with the same

gravitational constant as 433 Eros is taken. The Sun is initialised with the same absolute distance to the point mass as described in Table 4-6, but positioned along the z-axis of the inertial frame. The spacecraft orbit is initialised with a radius of 35 km and the inclination at zero, such that the angle between the orbital plane and the Sun vector is equal to 90 deg. The spacecraft is initialised with its solar panels pointing in the direction of the z-axis of the inertial frame.

It should be observed that for the equatorial orbit, a constant sinusoidal offset for the variation equations is visible. For an equatorial orbit, where the $\alpha = 90$ deg, the variations of i and Ω have been plotted in the top figure of Figure 4-8. It can be seen that the period of the sinusoidals coincide with the periods of the rotation terms of the quaternion. These have been plotted in the lower figure of Figure 4-8. As the other terms of the quaternion do not change over the course of the trajectory, they have been omitted from the plot.

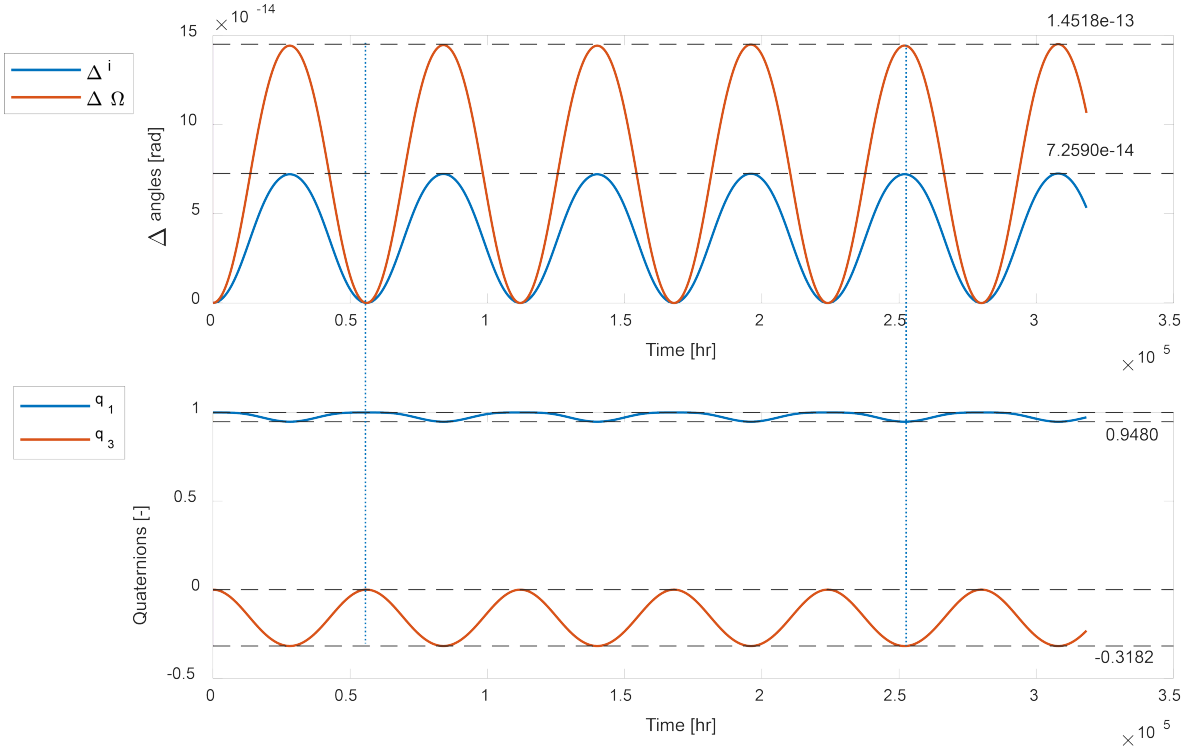

Figure 4-8: Variation equations and propagation of the quaternion terms q_1 and q_3 of the spacecraft orientation, for simulation of the solar radiation pressure.

When the orientation of the spacecraft shifts, the angle of the incoming solar rays change accordingly. Hence, the SRP acceleration changes. It can be concluded that for the simulated scenario, with the Sun position in the middle of the orbit, the SRP causes a constant rotation of the attitude. This is in line with the expected outcome and thus the solar radiation pressure model is verified.

Chapter 5

Dynamic Model Spacecraft Navigation

In this chapter, the state space model derivation is given, which is needed for the navigation filter in Chapter 6. In addition, the simulation of the sensor measurements are discussed as well.

For the proximity operations around 433 Eros it is required to use a navigation system that estimates both attitude and position. Therefore, a sensor selection is required that can provide measurements from which information can be derived about both position and orientation. It is desired that only essential sensors are included, making the system reliable and accurate enough, but not overflowing with redundant or unnecessary information. By selecting at least two measurements that can provide either information about the position or attitude, the output of the sensor fusion model is never based on one source of information. In doing so, it should be possible to account for errors within the sensor models. Therefore, a star tracker, inertial measurement unit (IMU) and a light detection and ranging (LiDAR) sensor are selected for the sensor fusion model. All of these sensors have been successfully implemented in previous spacecraft design for navigation in proximity of an asteroid (Heyler and Harch (2002),Daly et al. (2017)).

A magnetometer cannot be used for attitude estimation as no magnetic field is present. Gyroscopes can provide three-axis attitude estimation, although 'gyroscope values are not reliable for long-duration experiments' (Poulose et al., 2019). Inertial measurements need calibration provided by other sensors, which a star tracker can account for. Star trackers can provide three-axis attitude estimation as well, making them a good candidate as the second sensor to provide orientation measurements.

For guidance navigation & control (GNC), gyroscopes are usually integrated into an IMU. An IMU can also be used for the estimation of non-conservative accelerations of the spacecraft, such as the SRP. Using LiDAR, the accelerometer of the IMU can be calibrated as well. The accelerometer can only provide measurements relative to the assumed initial position and acceleration of the spacecraft. Using the measurements of the LiDAR, any offset to the initial position can be accounted for. A disadvantage of LiDAR is the high power consumption and relative high mass for a navigation sensor. Although a power budget of 60 to 70 Watt is

relatively high compared to other sensors, it should be able to fit within the power budgets of recent spacecraft designs that visited asteroids, such as OSIRIS-REx (Daly et al., 2017).

In general, navigation cameras are attractive sensors as they are passive with low power and mass requirements and have few complex parts, as compared to LiDAR. However, for LiDAR, the illumination of the asteroid does not have to be taken into account, which the measurements of a navigation camera is highly dependent on. For continuous estimation of the position, using LiDAR is therefore preferred.

The main features of the state space model presented in this chapter are listed below.

1. The state space model propagates the position, velocity, attitude error of the spacecraft with respect to the inertial reference frame.
2. Additionally, the asteroid gravitational parameter is propagated as well.
3. The non-gravitational acceleration and rotation rate measurements of the IMU are considered as input for the state space update.
4. The IMU measurements are simulated using Equation 5-17
5. The star tracker measurements are simulated using Equation 5-21
6. The LiDAR measurements are simulated using Equation 5-22

The derivation of this state space model is presented in Section 5-1. In the previous chapter, the true state simulation for the navigation problem has been presented. Given the true state simulation, the sensor measurements for the navigation filter can be simulated as well. In Section 5-2 until Section 5-4, all sensors are described, and their measurement simulation is presented.

5-1 State Space Model Derivation

In this section, the derivation of the state space model, which is used in the navigation filter, is given. The navigation filter will be presented in Chapter 6. We start with the selecting which states are propagated in the state space model. First and foremost, the attitude, velocity, and position need to be estimated. The states that are considered for the initial state space model are

$$\mathbf{x} = \begin{pmatrix} \mathbf{r}_I \\ \mathbf{v}_I \\ \boldsymbol{\Theta}_{B/I} \\ \mu \end{pmatrix}, \tag{5-1}$$

where $\mathbf{r}_I$ is the position vector in inertial frame, $\mathbf{v}_I$ is the velocity vector in inertial frame, $\boldsymbol{\Theta}_{B/I}$ is the quaternion error vector between the spacecraft and inertial frame and μ is the asteroid gravitational parameter. It is optional to be merged with the navigation filter of Spee (2022), which is why μ has been included as well. By expressing the state space equations in the inertial reference frame, the equations are kept as simple as possible. Hence, we don't have to take centrifugal or Coriolis forces into account.

For the position estimation, both the position and velocity vector are parameters in the state space model. As the derivative of velocity is partially dependent on position, the model is more straightforward to implement. Furthermore, the propagation of the velocity provides a direct coupling with the kinematics of the spacecraft, which will be presented shortly.

As discussed in Subsection 3-3-3, it is advantageous to use quaternions for attitude representation rather than Euler angles. Theses such as Razgus (2016) and Ballester (2018) investigated the advantage of implementing dual quaternions. Implementation of dual quaternions was expected to provide coupling between rotational and translational motion in the state space model. However, Razgus (2016) concluded that 'the dual quaternion filter and the quaternion-vector filter have identical performances in the steady-state'. Similarly, as shown by the implementation by Ballester (2018), a controller for circular orbit proximity operations achieves the same accuracy as for a normal quaternion in the state space model, but with 15% more computational time.

Hence, a quaternion-vector is considered. Using quaternions, the lowest-dimensional representation is used that is free from singularities (Wie, 2008). However, the quaternion is limited by its normalisation constraint, which cannot be assured when propagated in the state space model. In order to omit the issues arising when applying quaternions in a state space model as described by Zhou and Colgren (2005), the quaternion errors are propagated instead. With the quaternion error vector, the error quaternion $\delta\mathbf{q}_{B/I}$ can be computed as

$$\delta\mathbf{q}_{B/I} = \exp\left(\frac{\boldsymbol{\Theta}_{B/I}}{2}\right) \approx \begin{pmatrix} \frac{\boldsymbol{\Theta}_{B/I}}{2} \\ 1 \end{pmatrix}. \tag{5-2}$$

The error quaternion can be added to the attitude quaternion for each time step using

$$\mathbf{q}_{B/I,k+1} = \mathbf{q}_{B/I,k} \otimes \delta\mathbf{q}^*_{B/I,k}. \tag{5-3}$$

5-1-1 Nonlinear time continuous state space

The state transition matrix in continuous time can generally be described by

$$\dot{\mathbf{x}} = \mathbf{f}(\mathbf{x}, \mathbf{u}) + \mathbf{w} \quad \mathbf{w} \sim \mathcal{N}(0, \mathbf{Q}) \tag{5-4}$$

where $\mathbf{w}$ is the process noise vector with covariance $\mathbf{Q}$. In this case, $\mathbf{f}(\mathbf{x}, \mathbf{u})$ is equal to

$$\mathbf{f}(\mathbf{x}, \mathbf{u}) = \begin{pmatrix} \mathbf{v}_I \\ -\frac{\mu}{r_I^3}\mathbf{r}_I + C_{I/B}\tilde{\mathbf{a}}_B \\ -[\tilde{\boldsymbol{\omega}}^B_{B/I}]_\times \boldsymbol{\Theta}_{B/I} \\ 0 \end{pmatrix}, \tag{5-5}$$

where

$$\mathbf{u} = \begin{pmatrix} \tilde{\mathbf{a}}_B \\ \tilde{\boldsymbol{\omega}}^B_{B/I} \end{pmatrix}. \tag{5-6}$$

Outside of the state space propagation, the complete quaternion is propagated using

$$\dot{\mathbf{q}}_{B/I} = \frac{1}{2}\mathbf{\Omega}(\tilde{\boldsymbol{\omega}}^{\mathbf{B}}_{\mathbf{B/I}}). \tag{5-7}$$

after which the propagated error quaternion is added using Equation 5-2 and Equation 5-3. In Equation 5-7, $\mathbf{\Omega}(\omega)$ is defined as

$$\mathbf{\Omega}(\boldsymbol{\omega}) = \begin{pmatrix} 0 & -\omega_x & -\omega_y & -\omega_z \\ \omega_x & 0 & \omega_z & -\omega_y \\ \omega_y & -\omega_z & 0 & \omega_x \\ \omega_z & \omega_y & -\omega_x & 0 \end{pmatrix}. \tag{5-8}$$

Different from Bourgeaux (2020), which 'assumed that the solar radiation pressure (SRP) was estimated earlier in the mission and therefore a small error, the value with the SRP was given to the estimation filter', there is no SRP term given to the navigation filter. As the true state simulated SRP is not constant throughout the trajectory, it cannot be considered a constant that can be added. Instead, it is assumed that the acceleration due to SRP is taken into account from the accelerometer measurements. Both $\tilde{\boldsymbol{\omega}}^B_{B/I}$ and $\tilde{\mathbf{a}}_B$ are considered direct sensor outputs of the IMU sensor. Although the outputs of the IMU are considered measurements, they are considered as noisy inputs within the state space equations. For the navigation filter presented in Chapter 6, the noisy input can be accounted for by adding a term for their measurement noise in the process noise matrix (Ma et al., 2019).

5-1-2 Discrete-time Nonlinear Model

In order to use the state space system in a simulation, the time-discrete version of the model is needed. This is generally defined as

$$\mathbf{x_{k+1}} = \mathbf{x}_k + \mathbf{f}(\mathbf{x}_k, \mathbf{u}_k)\Delta t + \mathbf{w}_k \quad \mathbf{w}_k \sim \mathcal{N}(0, \mathbf{Q}) \tag{5-9}$$

where Δt is the time step between moment k and $k+1$, and where $\mathbf{w}_k$ is the process noise vector with covariance $\mathbf{Q}$ at time step k. Using Equation 5-5, the dynamic model becomes

$$\mathbf{x_{k+1}} = \mathbf{x}_k + \begin{pmatrix} \mathbf{v}_{I,k} \\ -\frac{\mu}{r^3_{I,k}}\mathbf{r}_{I,k} + C_{I/B,k}\tilde{\mathbf{a}}_{B,k} \\ -[\tilde{\boldsymbol{\omega}}^B_{B/I,k}]_\times \mathbf{\Theta}_{B/I,k} \\ 0 \end{pmatrix} \Delta t + \mathbf{w}_k. \tag{5-10}$$

The quaternion is now computed using

$$\mathbf{q}_{B/I,k+1} = \mathbf{q}_{B/I,k} + \frac{\Delta t}{2}\mathbf{\Omega}(\tilde{\boldsymbol{\omega}}^B_{B/I,k}), \tag{5-11}$$

after which the quaternion is normalised to preserve the unit quaternion properties.

5-1-3 Discrete-time Linear Model

In order to describe a linear time-discrete version of the state space system, the time update can be defined as

$$\mathbf{x_{k+1}} = (I + \mathbf{F}_k \Delta t)\mathbf{x}_k + \mathbf{w}_k \quad \mathbf{w}_k \sim \mathcal{N}(0, \mathbf{Q}) \tag{5-12}$$

where $\mathbf{F}_k$ is the derivative matrix of $\mathbf{f}(\mathbf{x}_k, \mathbf{u}_k)$ around $\mathbf{x}_k$ at point k. First, $\mathbf{F}$ is computed by first deriving all partial derivatives of $\mathbf{f}(\mathbf{x}, \mathbf{u})$ with respect to $\mathbf{x}$ such that

$$\mathbf{F} = \begin{bmatrix} \frac{\partial \mathbf{f}_1}{\partial \mathbf{x}_1} & \frac{\partial \mathbf{f}_1}{\partial \mathbf{x}_2} & \dots & \frac{\partial \mathbf{f}_1}{\partial \mathbf{x}_n} \\ \frac{\partial \mathbf{f}_2}{\partial \mathbf{x}_1} & \frac{\partial \mathbf{f}_2}{\partial \mathbf{x}_2} & \dots & \frac{\partial \mathbf{f}_2}{\partial \mathbf{x}_n} \\ \vdots & \vdots & \dots & \vdots \\ \frac{\partial \mathbf{f}_m}{\partial \mathbf{x}_1} & \frac{\partial \mathbf{f}_m}{\partial \mathbf{x}_2} & \dots & \frac{\partial \mathbf{f}_m}{\partial \mathbf{x}_n} \end{bmatrix}, \tag{5-13}$$

where m is the amount of rows in $\mathbf{f}(\mathbf{x}, \mathbf{u})$ and n is the amount of parameters in the state space vector.

The matrix for $\mathbf{F}_k$ derived from Equation 5-10 is then equal to

$$\mathbf{F}_k = \begin{bmatrix} \mathbf{0}_{3\times3} & \mathbf{I}_{3\times3} & \mathbf{0}_{3\times3} & \mathbf{0}_{3\times1} \\ \frac{\partial \dot{\mathbf{v}}_{I,k}}{\partial \boldsymbol{r}_{I,k}} & \mathbf{0}_{3\times3} & [\tilde{\boldsymbol{\omega}}^B_{B/I,k}]_\times \tilde{\mathbf{a}}_k & \frac{\partial \dot{\mathbf{v}}_{I,k}}{\partial \mu_k} \\ \mathbf{0}_{3\times3} & \mathbf{0}_{3\times3} & [\tilde{\boldsymbol{\omega}}^B_{B/I,k}]_\times & \mathbf{0}_{3\times1} \\ \mathbf{0}_{1\times3} & \mathbf{0}_{1\times3} & \mathbf{0}_{1\times3} & \mathbf{0}_{1\times1} \end{bmatrix}. \tag{5-14}$$

Here, $\frac{\partial \dot{\mathbf{v}}_{I,k}}{\partial \boldsymbol{r}_{I,k}}$ is defined as

$$\frac{\partial \dot{\mathbf{v}}_{I,k}}{\partial \boldsymbol{r}_{I,k}} = \frac{\mu}{r^5_{I,k}} \begin{bmatrix} 3r^2_{I,x} - r^2_{I,k} & 3r_{I,x,k}r_{I,y,k} & 3r_{I,x,k}r_{I,z,k} \\ 3r_{I,y,k}r_{I,x,k} & 3r^2_{I,y,k} - r^2_{I,k} & 3r_{I,y,k}r_{I,z,k} \\ 3r_{I,z,k}r_{I,x,k} & 3r_{I,z,k}r_{I,y,k} & 3r^2_{I,z,k} - r^2_{I,k} \end{bmatrix}. \tag{5-15}$$

Next, $\frac{\partial \dot{\mathbf{v}}_{I,k}}{\partial \mu_k}$ is equal to

$$\frac{\partial \dot{\mathbf{v}}_{I,k}}{\partial \mu_k} = -\frac{1}{r^3_{I,k}} \begin{bmatrix} r_{I,x,k} \\ r_{I,y,k} \\ r_{I,z,k} \end{bmatrix}. \tag{5-16}$$

5-2 Inertial Measurement Unit Model

Whereas previous theses only assumed either a gyroscope measurement (Razgus, 2016) or the non-gravitational forces readily available (Bourgeaux, 2020), an IMU has been chosen to be incorporated into the sensor set. The IMU consists of both a gyroscopes and an accelerometer, meaning that two outputs will be modelled.

It is demonstrated by Rawashdeh and James E. Lumpp (2012), Lam and Crassidis (2007), and Clerc et al. (2009) that an IMU can be integrated in sensor fusion models for spacecraft

attitude estimation. However, I was not able to find (published) literature where the integration of an IMU into a system that estimates both position and attitude for in spacecraft navigation is demonstrated. The main advantage of the additional access to the accelerometer data is the fact that only the non-gravitational forces can be measured. Rather than measurements that provide (relative) position information, there is a distinction between the orbital mechanics in the state space system, and the disturbance forces acting on the spacecraft. This can be insightful not only for estimating the SRP as will be done for this research, but also the impact of thruster firing.

Furthermore, any non-gravitational force exerted on the spacecraft body is measured in the spacecraft reference frame. In our case, the state estimation of the state space system is expressed in the inertial frame. Therefore, the gyroscope data is necessary to express the accelerations in the inertial reference frame as could be seen in Section 5-1. Since Razgus (2016) did not incorporate a measurement or constant for the SRP in his state space model, the aforementioned link from the attitude and position equations is missing. They had to resort to express the state space system in the asteroid reference frame to ensure coupling of the attitude and position states. For the asteroid reference frame, the state space equations and their linearisations become more complicated as the Coriolis and centrifugal accelerations now also need to be taken into account.

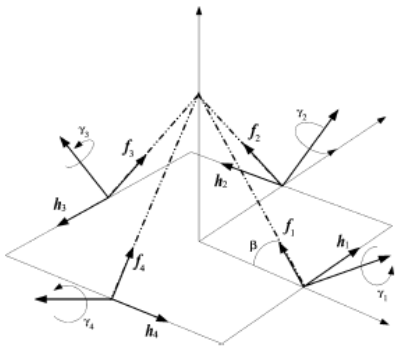

Figure 5-1: Pyramid configuration of four IMU sensors (Leeghim et al. (2009)).

Next to the proven use of IMUs in sensor fusion, it is also known that the IMU was already part of the sensor set in the design of Near Earth Asteroid Rendezvous (NEAR). As seen in Figure 5-1, redundancy for the sensor was incorporated by placing four IMU's in a pyramid configuration (McAdams et al., 2000). Should one of them fail, there is still coverage for all axes of the main spacecraft reference frame.

Two main outputs will be modelled. The model is simplified to provide one accelerometer output and one gyroscope output. Derived from the model of Li and Mourikis (2012), the measurement modelling for the gyroscope and accelerometer of the IMU can be computed using

$$\begin{aligned} \tilde{\boldsymbol{\omega}}_{B/I}^{B} &= \boldsymbol{\omega}_{B/I}^{B} + \mathbf{b}_g + \mathbf{n}_g, \quad \mathbf{n}_g \sim \mathcal{N}\left(0, \sigma_{n_g}^2 I_3\right), \\ \tilde{\mathbf{a}}_B &= \mathbf{a}_B + \mathbf{b}_a + \mathbf{n}_\mathbf{a}, \quad \mathbf{n}_a \sim \mathcal{N}\left(0, \sigma_{n_a}^2 I_3\right), \end{aligned} \tag{5-17}$$

where $\boldsymbol{\omega}_{B/I}^{B}$ is the rotation rate of the true state, $\mathbf{a}_B$ is the non-gravitational acceleration of the true state, $\mathbf{b}_g$ is the gyroscope bias error, $\mathbf{b}_a$ is the accelerometer bias error, $\mathbf{n}_g$ is the

gyroscope white noise, $\mathbf{n}_a$ is the accelerometer white noise, and I_3 is a 3-by-3 identity matrix. Hence, the measurement vector for the IMU is defined as

$$\tilde{\mathbf{y}}_{IMU} = \begin{bmatrix} \tilde{\boldsymbol{\omega}}^B_{B/I} \\ \tilde{\mathbf{a}}_B \end{bmatrix}. \tag{5-18}$$

A bias error is chosen for the sensor modelling as this type of error is most commonly found for inertial sensors (Haberberger, 2016). For the benchmark scenario, no bias is implemented yet. An overview of common values for the output and the errors of the sensors can be found in Table 5-1. Here, the settings for the measurement modelling of the benchmark scenario are also given.

Table 5-1: Properties of IMU sensor model, based on Li and Mourikis (2012), Thienel and Sanner (2003).

Accelerometer			Gyroscope		
Property	Range	Benchmark	Property	Range	Benchmark
Output rate	100-1024 [Hz]	100 [Hz]	Output rate	100-1024 [Hz]	100 [Hz]
White noise	n/a	$0.9 \cdot 10^{-3}$ [m/s^2]	White noise	n/a	$0.2 \cdot 10^{-4}$ [rad/s]
Bias	0.002-0.2[mg]	0 [m/s^2]	Bias	0.1-3 [deg/s]	0 [deg/s]

For the white noise settings, there are no common values that can be found in literature, as the white noise that is being modelled is usually a combination of scaling, misalignment and temperature errors.

5-3 Star Tracker Model

The working principle behind a star tracker is that attitude can be determined by recognising patterns in images of the stars. Each star tracker has a predefined map of all the stars available in their software, such as the Hipparcos catalogue (van Leeuwen, 2007). Irrespective of the position within the solar system, the stars in the catalogue are always positioned in the same direction. Based on the given map and using a model of the spacecraft motion, the software integrated into the micro-computer of the start tracker extrapolates the corresponding attitude (Buemi et al., 1999). For the images, the sensor comprises a camera with a wide field of view lens, as five stars need to be detected for attitude determination (Marin and Bang, 2020).

Although Sun sensors are also a common option for attitude determination, they can provide information for less degrees of freedom, and have a lower accuracy (Liebe, 1995). Furthermore, Rawashdeh and James E. Lumpp (2012) explains that 'maintaining attitude knowledge in eclipse, in the absence of the Sun vector measurement, is challenging and is often addressed by propagating rate information from the rate gyroscopes at the cost of drift'.

As previously mentioned, a star tracker consists of a pre-processing algorithm that translates an image to a star pattern, and then to a spacecraft attitude. It is assumed that this output is the measurement that will be integrated into the navigation filter. This was also the method for attitude determination within the navigation and control system of NEAR (Strikwerda et al., 1998).

For the measurement modelling, we start with defining the error angle as

$$\tilde{\boldsymbol{\Theta}} = \boldsymbol{n}_q, \quad \mathbf{n}_q \sim \mathcal{N}\left(0, \sigma_{n_q}^2 I_3\right), \tag{5-19}$$

for which the error quaternion becomes

$$\delta\tilde{\mathbf{q}}_k = \begin{bmatrix} \frac{\tilde{\boldsymbol{\Theta}}}{2} \\ 1 \end{bmatrix}. \tag{5-20}$$

With the error quaternion, a measured quaternion is computed by combining it with the quaternion of the true state simulation such that

$$\tilde{\mathbf{y}}_{ST} = \tilde{\mathbf{q}}_k = \mathbf{q}_k \otimes \delta\tilde{\mathbf{q}}_k^*, \tag{5-21}$$

where $\tilde{\mathbf{y}}_{ST}$ is the star tracker measurement vector.

Although it is possible to introduce more detailed models of the measurements of a star tracker, there are complete research papers dedicated to the simulation of star trackers. For instance, Marin and Bang (2020) introduces a model to simulate the star features as according to the database, coverage and optical performance of the camera, and a star detection algorithm. This is, however, beyond the time scope of the research. In Table 5-2, the settings for the star tracker model are presented. Contrary to the inertial sensor modelling, there is no bias incorporated into the model. Inertial sensors are most likely to suffer from drift due to bias instability, as argued by Sadeghzadeh-Nokhodberiz and Poshtan (2016). It is assumed that it is more likely that this sensor will suffer from temporary signal loss. This will be simulated for one of the result sets in Chapter 7.

Table 5-2: Properties of star tracker sensor model, based on Li and Mourikis (2012).

Output Parameter	$[q_1 \quad q_2 \quad q_3 \quad q_4]^T$	
Property	Range	Benchmark
Output rate	1-10[Hz]	10[Hz]
White noise	0.1-3 [arcsec]	$\begin{bmatrix}5 & 5 & 5\end{bmatrix}$ [arcsec]

5-4 LiDAR Model

The last presented sensor is the LiDAR, which provides information about the position of the spacecraft relative to the target asteroid. The working principle behind LiDAR technology is that a time-of-flight (ToF) is measured for a laser beam to travel from the spacecraft to a target and back. In order determine the ToF more accurately, a pseudo-random noise code is encoded on the emitted laser signal, which is then autocorrelated with the returning signal (Christian and Cryan, 2013). A main advantage to LiDAR according to Christian and Cryan (2013) is that it can provide accurate estimation of the ToF. Furthermore, as mentioned previously, the sensor is not dependent on the spacecraft and asteroid position with respect to the Sun.

In the previous research by Razgus (2016) and Bourgeaux (2020), it was assumed that both a navigation camera and a LiDAR are available in the sensor set. By introducing a landmark tracking algorithm, control angles are determined by the navigation camera pre-processing algorithm and send to the LiDAR to be added to the measured range as measurement outputs. For the measured range of the model by Bourgeaux (2020), it is assumed 'that the surface mapping of the asteroid was done earlier in the mission'. As this is not part of the current set of assumptions for the benchmark scenario, it is not possible to take into account a landmark tracking algorithm. The state space model assumes that only a gravitational constant estimate is known for the point-mass approximation of the asteroid.

Furthermore, this would mean that their navigation camera models would have to be incorporated and verified in the sensor simulation, or a new model has to be developed. This was beyond the time scope of the thesis. As it has already been demonstrated that a navigation filter can work in certain proximity operations around an asteroid, the research gap is larger for only considering a LiDAR sensor to be available.

We assume that, for an available range measurement, the control angles of the pointing of the LiDAR are known exactly beforehand. Therefore, the elevation, ϵ, and azimuth, ϕ, with respect to the asteroid are known as well. This is a simplification by combining the LiDAR pointing and the orientation of the spacecraft reference frame. This is similar to the method of Jung et al. (2012) where they assumed 'the azimuth and elevation angle corresponding to angles in a laser-based observation were obtained through the attitude of chief satellite'. Furthermore, for simplicity the shape of the asteroid is not taken into account. The measurement vector for the LiDAR sensor is thus defined as

$$\tilde{\mathbf{y}}_{Li} = \begin{bmatrix} \tilde{\rho} \\ \tilde{\epsilon} \\ \tilde{\phi} \end{bmatrix}, \tag{5-22}$$

where

$$\tilde{\rho} = \sqrt{r_x^2 + r_y^2 + r_z^2} + n_\rho, \quad n_\rho \sim \mathcal{N}\left(0, \sigma_{n_\rho}^2\right), \tag{5-23}$$

$$\tilde{\epsilon} = \arctan\left(\frac{r_y}{r_x}\right) + n_\epsilon, \quad n_\epsilon \sim \mathcal{N}\left(0, \sigma_{n_\epsilon}^2\right), \tag{5-24}$$

$$\tilde{\phi} = \arctan\left(\frac{r_z}{\sqrt{r_x^2 + r_y^2}}\right) + n_\phi, \quad n_\phi \sim \mathcal{N}\left(0, \sigma_{n_\phi}^2\right), \tag{5-25}$$

where r_x, r_y, and r_z are the components of the position of the true state simulation. Hence, the distance measured is from the spacecraft to the centre of volume.

Again, there is no bias implemented into the sensor modelling, but a temporary signal loss will be one of the test cases for the simulation results in Chapter 7. An overview of the settings for the benchmark and the commonly found values in literature are presented in Table 5-3.

Table 5-3: Properties of LiDAR sensor modelling, based on Markley and Crassidis (2014), Ilci and Toth (2020), Tsuno et al. (2006).

Output Parameters		$\begin{bmatrix}\rho & \alpha & \delta\end{bmatrix}$
Property	Range	Benchmark
Output Rate	0.1-20 [Hz]	1 [Hz]
White noise	0.02-10[m], 0.0035-0.01 [rad]	$\begin{bmatrix}0.1[\text{m}] & 2e-5[\text{rad}] & 2e-5[\text{rad}]\end{bmatrix}$

Chapter 6

State Estimation

In this chapter the navigation filter is presented. Beforehand, the general architecture of the complete navigation software model is presented to have an overview of the data flow. This can be found in Section 6-1. The previously discussed measurement modelling and dynamic model derivation then form the base to the navigation filter presented in Section 6-2. In this section, the implementation of a Kalman filter is discussed, including the measurement equations, tuning parameters and covariance settings.

6-1 Navigation Architecture

In Figure 6-1, the complete architecture of the software is visible. Both the simulation of the true states, the measurements of the sensor models, and the navigation filter parts are visible here. Based on the true state, the outputs of the different sensors can be modelled. Then, depending on their output rate, the measurements are sent to various blocks of the navigation filter.

As seen in Figure 6-1, the measurement update for the extended Kalman filter (EKF) is separated in two different blocks. For both the star tracker and the LiDAR, a separate measurement update is performed. Since the measurements by the IMU are considered as inputs, they are directly implemented in the time update. As McAdams et al. (2000) states, 'estimated attitude is propagated between star [tracker measurement] updates using IMU data'. Therefore, using the IMU measurements in the time update is in line to previous mission design of the NEAR mission.

The system is considered to be an overall loose integration, mainly due to the separate measurement updates for the star tracker and the LiDAR, and the presence of a pre-processing algorithm for the star tracker. It should be noted however that more loosely coupled systems are possible for the navigation architecture, such as for decentralised filters demonstrated by Sadeghzadeh-Nokhodberiz and Poshtan (2016). Although error estimation and compensation can be carried out beforehand, Cioffi and Scaramuzza (2020) argues that 'the use of a tightly-coupled approach allows exploiting the correlations amongst all the measurement'. Before

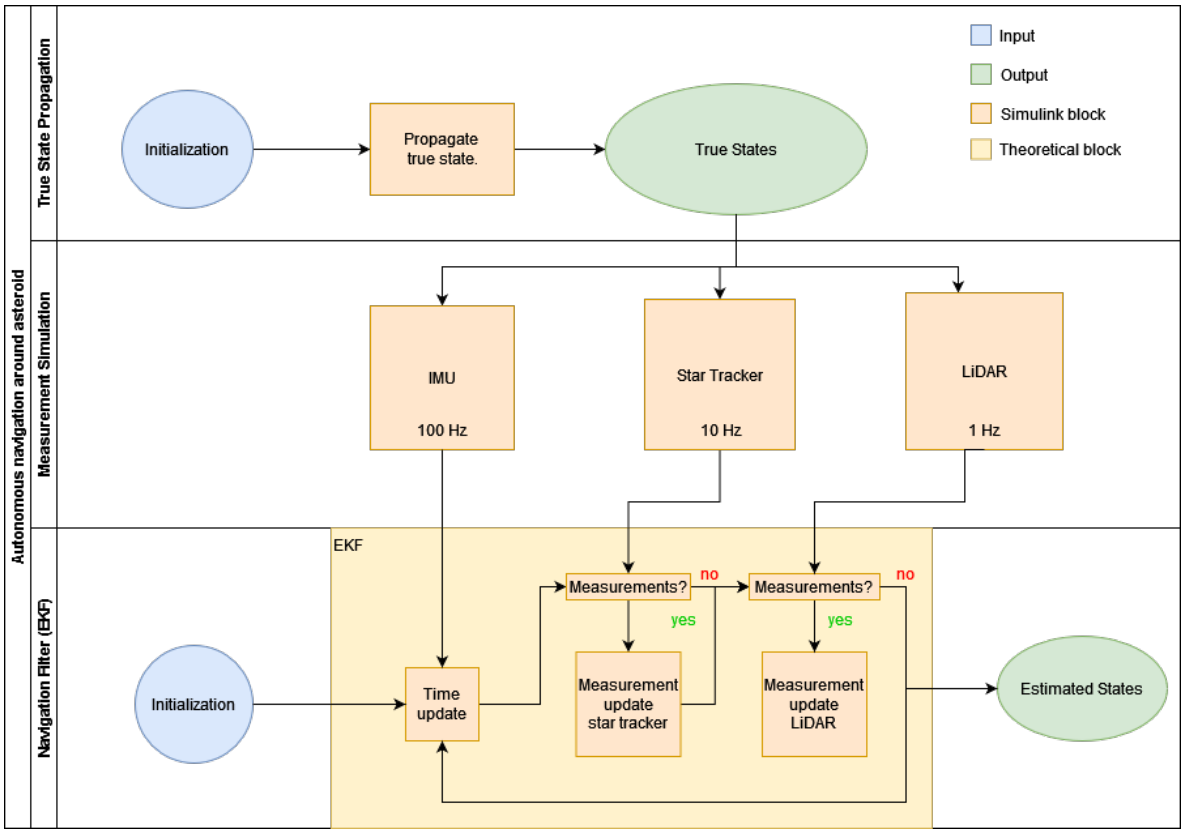

Figure 6-1: Navigation Simulation Architecture.

developing a model that is more tightly-coupled, it should first be demonstrated that for the given mission context and information from the sensor set, position and attitude determination is feasible. Hence, developing a more tightly coupled system would be a recommendation for future research depending on the results of this thesis.

The output rates of the sensors presented in Chapter 5 have been implemented in the throughput to the measurement updates. As the navigation filter can be simulated for different time step sizes, the output rates are adjusted accordingly: if the simulation time step is larger than the sensor output time step, the frequency is adjusted to match the smaller frequency. As the output frequency of the IMU corresponds to the smallest time step used in the simulations, it is assumed an IMU measurement is always provided during the time update.

6-2 Kalman filter

For navigation filtering, an EKF has been selected. Opromolla and Nocerino (2019) have demonstrated implementation of an unscented Kalman filter (UKF) for a loosely-coupled relative navigation system that estimates the relative position, velocity and attitude with respect to an uncooperative space target. In addition, Yang and Li (2016) concludes that 'the differences between the EKF and UKF [performance] become more significant when the nonlinearity increases. This was demonstrated with a model with fourth- and fifth-order functions

in the dynamic model. Bourgeaux (2020) demonstrated that UKF navigation slightly outperforms an EKF equivalent as well, however the motivation for using an UKF was largely due to easier implementation. When using spherical harmonics to estimate the gravitational acceleration, the Jacobian matrix becomes very large as all the spherical harmonic coefficients of the expansion order need to be in the state vector (Bourgeaux, 2020).

On the other hand, the mean computational time per time step, according to St-Pierre and Gingras (2004), is 0.0658 s for the UKF opposed to only 0.0028 s for the EKF for target tracking problems. They suggests that actual improvement of the UKF computational time with respect to the EKF would be more apparent when decentralising the navigation architecture and using the filters on each separate sensor. If not, 'potential linearisation errors of the extended Kalman filter are negligible'.

The basis of our navigation filter is thus an EKF. In order to cope with the quaternion error vector, $\boldsymbol{\Theta}$, the EKF is considered to be a multiplicative extended Kalman filter (MEKF) for those three states. There are multiple advantages for applying this method. As Madyastha et al. (2011) states, 'the orientation error-state is minimal, avoiding issues related to over-parameterisation (or redundancy) and the consequent risk of singularity of the involved covariances matrices'. The error-state values are thus smaller, avoiding the points where parameter singularity or gimbal lock, for Euler angle states, would normally occur.

Using the state space system that has previously been defined and the Kalman filter algorithm as defined by Kok et al. (2017), the set-up of the implemented Kalman filter time update is equal to

$$\mathbf{x}_{k+1|k} = \mathbf{x}_{k|k} + \mathbf{f}(\mathbf{x}_{k|k}, \mathbf{u}_k)\Delta t, \tag{6-1a}$$

$$\mathbf{P}_{k+1|k} = \mathbf{F}_{k|k}\mathbf{P}_{k|k}\mathbf{F}_{k|k}^T + \mathbf{G}_k\mathbf{Q}\mathbf{G}_k^T, \tag{6-1b}$$

where $\mathbf{f}(\mathbf{x}_{k|k}, \mathbf{u}_k)$ is as defined in Equation 5-5, $\mathbf{F}_{k|k}$ as defined in Equation 5-13, and $\mathbf{G}_k$ is equal to

$$\mathbf{G}_k = \begin{pmatrix} \mathbf{0}_{3\times3} & \mathbf{0}_{3\times3} \\ \mathbf{I}_{3\times3} & \mathbf{0}_{3\times3} \\ \mathbf{0}_{3\times3} & \mathbf{I}_{3\times3} \\ \mathbf{0}_{1\times3} & \mathbf{0}_{1\times3} \end{pmatrix}, \tag{6-2}$$

and

$$\mathbf{Q} = \begin{pmatrix} \sigma_{acc}^2 + \sigma_{n_a}^2 & \mathbf{0}_{3\times3} \\ \mathbf{0}_{3\times3} & \sigma_{n_g}^2 + \sigma_{\Theta}^2 \end{pmatrix}. \tag{6-3}$$

Here, σ_{acc}^2 and σ_{Θ}^2 are the covariances of the process noise of the acceleration and quaternion process noise, $\mathbf{n}_{acc}$ and $\mathbf{n}_{\Theta}$ respectively. In addition to the process noise covariances, we have the covariance of the measurement white noise of the accelerometer and gyroscope, as defined in Equation 5-17. Since they are considered to be control inputs, their measurement noise covariance are added to the process noise covariance matrix $\mathbf{Q}$.

The measurement update is equal to

$$\mathbf{K}_{k+1} = \mathbf{P}_{k+1|k}\mathbf{H}_{k+1}^T(\mathbf{H}_{k+1}\mathbf{P}_{k+1|k}\mathbf{H}_{k+1}^T + \boldsymbol{\Phi})^{-1}, \tag{6-4a}$$

$$\boldsymbol{\epsilon}_{k+1} = \tilde{\mathbf{y}}_{k+1} - \mathbf{h}(\mathbf{x}_{k+1|k}), \tag{6-4b}$$

$$\mathbf{x}_{k+1|k+1} = \mathbf{x}_{k+1|k} + \mathbf{K}_{k+1}\epsilon_{k+1}, \tag{6-4c}$$

$$\mathbf{P}_{k+1|k+1} = (\mathbf{I} - \mathbf{K}_{k+1}\mathbf{H}_{k+1})\mathbf{P}_{k+1|k}, \tag{6-4d}$$

where $\boldsymbol{\epsilon}_{k+1}$ is the measurement residual or innovation sequence, and $\boldsymbol{\Phi}$ is the measurement noise matrix, defined in either Equation 6-10 or Equation 6-17. After each measurement update, the quaternion is updated again using Equation 5-2 and Equation 5-3.

The relation between $\mathbf{x}_k$ and a measurement state can be defined as

$$\mathbf{z}_k = \mathbf{h}(\mathbf{x}_k) + \mathbf{v}_k \quad \mathbf{v}_k \sim \mathcal{N}(0, \boldsymbol{\Phi}), \tag{6-5}$$

where $\mathbf{v}_k$ is the measurement noise, and $\mathbf{h}(\mathbf{x_k})$ is a (nonlinear) measurement equation. The measurement equations can be linearised using

$$\mathbf{H}_k = \begin{bmatrix} \frac{\partial \mathbf{h}_1}{\partial \mathbf{x}_{k,1}} & \frac{\partial \mathbf{h}_1}{\partial \mathbf{x}_{k,2}} & \cdots & \frac{\partial \mathbf{h}_1}{\partial \mathbf{x}_{k,n}} \\ \frac{\partial \mathbf{h}_2}{\partial \mathbf{x}_{k,1}} & \frac{\partial \mathbf{h}_2}{\partial \mathbf{x}_{k,2}} & \cdots & \frac{\partial \mathbf{h}_2}{\partial \mathbf{x}_{k,n}} \\ \vdots & \vdots & \cdots & \vdots \\ \frac{\partial \mathbf{h}_m}{\partial \mathbf{x}_{k,1}} & \frac{\partial \mathbf{h}_m}{\partial \mathbf{x}_{k,2}} & \cdots & \frac{\partial \mathbf{h}_m}{\partial \mathbf{x}_{k,n}} \end{bmatrix}, \tag{6-6}$$

which we can use for the matrix multiplications in Equation 6-4.

The complete algorithm is summarised in Algorithm 1, where T is the total simulation time. Every time step, the time update is performed using the previously described Kalman equations. The measurement update is either performed once, twice or not at all: for each available star tracker or LiDAR measurement, a measurement update is performed. If both measurements are available, the star tracker measurement update is performed first.

If both measurements are available at an arbitrary time step, the outputs of the star tracker measurement update are considered as $\mathbf{X}_{k+1|k}$ and $\mathbf{P}_{k+1|k}$ for the next measurement update. As a baseline, the initialisation of the navigation filter is as summarised in Table 6-1.

6-2-1 Star Tracker Measurement Update

For the star tracker measurement update, we have the noisy quaternion as measurement output from the star tracker simulation. Since the state vector only contains the error state of the quaternion, the measured error quaternion is computed using

$$\delta\tilde{\mathbf{q}} = \tilde{\mathbf{q}}_{k+1} \otimes \hat{\mathbf{q}}^{-1}_{k+1|k}, \tag{6-7}$$

where $\tilde{\mathbf{q}}_{k+1}$ is the measured quaternion vector and $\hat{\mathbf{q}}^{-1}_{k+1|k}$ is the estimated quaternion after the time update. The measurement vector is then

$$\tilde{\mathbf{y}}_{\Theta,k+1} = \tilde{\boldsymbol{\Theta}}_k = 2[\delta\tilde{\mathbf{q}}_{k|1:3}]. \tag{6-8}$$

As the measurements are now the same as the parameters in the state vector, there is no linearisation of the measurement equation necessary since we already obtain

$$\mathbf{h}_{ST}(\mathbf{x}) = \mathbf{H}_{ST} = \begin{bmatrix} \mathbf{0}_{3\times3} & \mathbf{0}_{3\times3} & \mathbf{I}_{3\times3} & \mathbf{0}_{3\times1} \end{bmatrix}, \tag{6-9}$$

Algorithm 1: EKF algorithm with IMU input and Star tracker & Lidar Measurements.

Data: $\mathbf{x}_0$ & $\mathbf{P}_0$ (Table 6-1), $\mathbf{Q}$ (Equation 6-3), $\mathbf{\Phi}_{ST}$ (Equation 6-10), $\mathbf{\Phi}_{Li}$(Equation 6-17), $\tilde{\mathbf{y}}_{IMU}$ (Equation 5-18), $\tilde{\mathbf{y}}_{\tilde{\Theta}}$ (Equation 6-8), $\tilde{\mathbf{y}}_{Li}$ (Equation 5-22)

Result: $\mathbf{x}$, $\mathbf{P}$

for $\Delta t = 0$ *to* T **do**

- Compute $\mathbf{x}_{k+1|k}$ (Equation 6-1a)
- Compute $\mathbf{P}_{k+1|k}$ (Equation 6-1b)
- **if** $\mathbf{z}_{ST}$ *is available* **then**
  - Compute $\mathbf{K}_{k+1}$ (Equation 6-4a) for $\mathbf{H}_{k+1,ST}$ (Equation 6-9)
  - Compute $\boldsymbol{\epsilon}_{k+1}$ (Equation 6-4b) for $\mathbf{h}_{ST}(\mathbf{x}_{k+1|k})$ (Equation 6-9)
  - Compute $\mathbf{x}_{k+1|k+1}$ (Equation 6-4c)
  - Compute $\mathbf{P}_{k+1|k+1}$ (Equation 6-4d) for $\mathbf{H}_{k+1,ST}$ (Equation 6-9)
- **else**
  - forward $\mathbf{x}_{k+1|k}$ and $\mathbf{P}_{k+1|k}$ to next measurement update
- **end**
- **if** $\mathbf{z}_{Li}$ *is available* **then**
  - (Re)Compute $\mathbf{K}_{k+1}$ (Equation 6-4a) for $\mathbf{H}_{k+1,Li}$ (Equation 6-13)
  - (Re)Compute $\boldsymbol{\epsilon}_{k+1}$ (Equation 6-4b) for $\mathbf{h}_{k+1,Li}$ (Equation 6-12)
  - (Re)Compute $\mathbf{x}_{k+1|k+1}$ (Equation 6-4c)
  - (Re)Compute $\mathbf{P}_{k+1|k+1}$ (Equation 6-4d) for $\mathbf{H}_{k+1,Li}$ (Equation 6-13)
- **else**
  - $\mathbf{x}_{k+1|k+1}$=$\mathbf{x}_{k+1|k}$ and $\mathbf{P}_{k+1|k+1}$=$\mathbf{P}_{k+1|k}$, go to next time update
- **end**

end

Table 6-1: Initial conditions of estimating benchmark scenario.

$\mathbf{x}_0$ in EKF	value
$\mathbf{r}_{I,0}$ [km]	$\begin{bmatrix}51 & 1 & 1\end{bmatrix}^T$
$\mathbf{v}_{I,0}$ [m/s]	$\begin{bmatrix}1 & 3.961013552945929 & 1\end{bmatrix}^T$
$\mathbf{q}_{B/I,0}$ [-]	$\begin{bmatrix}0 & -0.7071 & 0 & 0.7071\end{bmatrix}^T$
$\mathbf{\Theta}_{B/I}$ [km]	$\begin{bmatrix}1\cdot10^{-7} & 1\cdot10^{-7} & 1\cdot10^{-7}\end{bmatrix}^T$
$\mathbf{P}_0$	$\begin{pmatrix}1000 & 0 & 0 & 0 & 0 & 0 & 0 & 0 & & \\ 0 & 1000 & 0 & 0 & 0 & 0 & 0 & 0 & 0 & 0 \\ 0 & 0 & 100 & 0 & 0 & 0 & 0 & 0 & 0 & 0 \\ 0 & 0 & 0 & 1 & 0 & 0 & 0 & 0 & 0 & 0 \\ 0 & 0 & 0 & 0 & 1 & 0 & 0 & 0 & 0 & 0 \\ 0 & 0 & 0 & 0 & 0 & 1 & 0 & 0 & 0 & 0 \\ 0 & 0 & 0 & 0 & 0 & 0 & 0.1 & 0 & 0 & 0 \\ 0 & 0 & 0 & 0 & 0 & 0 & 0 & 0.1 & 0 & 0 \\ 0 & 0 & 0 & 0 & 0 & 0 & 0 & 0 & 0.1 & 0 \\ 0 & 0 & 0 & 0 & 0 & 0 & 0 & 0 & 0 & 1\cdot10^{-10}\end{pmatrix}$
σ_{acc}	$\begin{bmatrix}5\cdot10^{-3} & 5\cdot10^{-3} & 1\cdot10^{-3}\end{bmatrix}^T$
σ_a	$\begin{bmatrix}1\cdot10^{-8} & 1\cdot10^{-8} & 1\cdot10^{-8}\end{bmatrix}^T$
σ_Θ	$\begin{bmatrix}1\cdot10^{-4} & 1\cdot10^{-4} & 1\cdot10^{-4}\end{bmatrix}^T$
σ_{gyro}	$\begin{bmatrix}1\cdot10^{-4} & 1\cdot10^{-4} & 1\cdot10^{-4}\end{bmatrix}^T$

for the measurement matrix, where the subscript ST denotes that this is the matrix for the star tracker. For the measurement noise of the star tracker update, $\mathbf{\Phi}_{ST}$ is initialised as

$$\mathbf{\Phi}_{ST} = \begin{pmatrix}(1\cdot10^{-4})^2 & 0 & 0\\ 0 & (1\cdot10^{-4})^2 & 0\\ 0 & 0 & (1\cdot10^{-4})^2\end{pmatrix}. \tag{6-10}$$

For computing the observability of the linear measurement matrix,

$$\begin{bmatrix}H & HF & HF^2 & HF^3 & ...\end{bmatrix}^T, \tag{6-11}$$

is used. When taking F_k as from Equation 5-14, and it was found that the observability matrix only has a rank of 3. For a fully observable matrix, the rank should be equal to the length of the state vector. This could mean that for 3 states the measurement matrix would provide sufficient control for convergence, which will have to be verified in the next chapter by testing the influence of only the star tracker measurement update in Subsection 7-1-1.

6-2-2 LiDAR Measurement Update

The three parameter outputs by the light detection and ranging (LiDAR) in the measurement vector defined in Equation 5-22 are the range, $\tilde{\rho}$, elevation, $\tilde{\epsilon}$, and azimuth, $\tilde{\phi}$, respectively.

The measurement equation equals

$$\mathbf{h}_{Li}(\mathbf{x}) = \begin{bmatrix} \sqrt{r_{I,x}^2 + r_{I,y}^2 + r_{I,z}^2} \\ \arctan\left(\frac{r_{I,y}}{r_{I,x}}\right) \\ \arctan\left(\frac{r_{I,z}}{\sqrt{{r_{I,x}}^2+{r_{I,y}}^2}}\right) \end{bmatrix}. \tag{6-12}$$

Linearising the measurement equation at point k gives the measurement matrix

$$\mathbf{H}_{k,Li} = \begin{bmatrix} \mathbf{B}_{k,1\times3} & \mathbf{0}_{1\times3} & \mathbf{0}_{1\times3} & \mathbf{0}_{1\times1} \\ \mathbf{E}_{k,1\times3} & \mathbf{0}_{1\times3} & \mathbf{0}_{1\times3} & \mathbf{0}_{1\times1} \\ \mathbf{D}_{k,1\times3} & \mathbf{0}_{1\times3} & \mathbf{0}_{1\times3} & \mathbf{0}_{1\times1} \end{bmatrix}, \tag{6-13}$$

where the subscript Li denotes that this is the matrix for the LiDAR measurement and

$$\mathbf{B}_{k,1\times3} = \begin{bmatrix} \frac{r_{I,x}}{\sqrt{r_{I,x}^2+r_{I,y}^2+r_{I,z}^2}} & \frac{r_{I,y}}{\sqrt{r_{I,x}^2+r_{I,y}^2+r_{I,z}^2}} & \frac{r_{I,z}}{\sqrt{r_{I,x}^2+r_{I,y}^2+r_{I,z}^2}} \end{bmatrix}, \tag{6-14}$$

$$\mathbf{E}_{k,1\times3} = \begin{bmatrix} -\frac{r_{I,y}}{r_{I,x}^2+r_{I,y}^2} & \frac{r_{I,x}}{r_{I,y}^2+r_{I,x}^2} & 0 \end{bmatrix}, \tag{6-15}$$

$$\mathbf{D}_{k,1\times3} = \begin{bmatrix} -\frac{r_{I,z}r_{I,x}}{\sqrt{r_{I,x}^2+r_{I,y}^2}\left(r_{I,x}^2+r_{I,z}^2+r_{I,y}^2\right)} & -\frac{r_{I,z}r_{I,y}}{\sqrt{r_{I,y}^2+r_{I,x}^2}\left(r_{I,y}^2+r_{I,z}^2+r_{I,x}^2\right)} & \frac{\sqrt{r_{I,y}^2+r_{I,x}^2}}{r_{I,z}^2+r_{I,y}^2+r_{I,x}^2} \end{bmatrix}, \tag{6-16}$$

which are all considerd for $\mathbf{r}_I$ at time step k. For the LiDAR noise, $\mathbf{\Phi}_{Li}$ is set to

$$\mathbf{\Phi}_{Li} = \begin{pmatrix} (1\cdot10^{-2})^2 & 0 & 0 \\ 0 & (1\cdot10^{-3})^2 & 0 \\ 0 & 0 & (1\cdot10^{-3})^2 \end{pmatrix}. \tag{6-17}$$

Again computing the observability of the measurement matrix gives a rank of 10, meaning that the system should be fully observable for this measurement update. However, as the state space system as well as the measurement matrix are linearised, this condition does not necessarily apply. Complete analysis of a nonlinear state space system requires a more in-depth analysis and is beyond the scope of this thesis. Results for only implementing the LiDAR sensor will be presented in Subsection 7-1-2.

Chapter 7

Experimental Results

In this chapter, all simulation results from the research are presented. The chapter starts with an analysis of the performance of the navigation filter for the benchmark scenario, as defined in Section 4-4, in Section 7-1. In the next section, Section 7-2, temporary losses of inputs by the star tracker and the LiDAR are considered, and the results are presented. Next, the influence of the time step on the state estimation accuracy of the navigation filter is analysed in Section 7-3. Then, the effect of orbital height is investigated. The navigation filter results for different orbital heights can be found in Section 7-4. In Chapter 8, my interpretation of the results is discussed.

7-1 Benchmark Scenario

In this section, the performance of the navigation filter for the benchmark scenario is presented. An overview of the parameter settings for the benchmark scenario is given in Table 7-1.

Table 7-1: Parameter settings for benchmark scenario.

	True State	Estimated State
$\mathbf{r}_I$ [km]	$\begin{bmatrix}50 & 0 & 0\end{bmatrix}^T$	$\begin{bmatrix}51 & 1 & 1\end{bmatrix}^T$
$\mathbf{v}_I$ [km]	$\begin{bmatrix}0 & 2.961 & 0\end{bmatrix}^T$	$\begin{bmatrix}1 & 3.961 & 1\end{bmatrix}^T$
$\mathbf{q}_{B/I}$ [km]	$\begin{bmatrix}0 & -0.707 & 0 & 0.707\end{bmatrix}^T$	$\begin{bmatrix}0 & -0.7071 & 0 & 0.7071\end{bmatrix}^T$
$\boldsymbol{\Theta}_{B/I}$ [km]	$\begin{bmatrix}0 & 0 & 0\end{bmatrix}^T$	$\begin{bmatrix}1\cdot10^{-7} & 1\cdot10^{-7} & 1\cdot10^{-7}\end{bmatrix}^T$

To start, both the star tracker and LiDAR are separately implemented into the navigation filter to analyse their influence on the filter performance. After the star tracker implementation in Subsection 7-1-1 and the LiDAR implementation in Subsection 7-1-2, the covariance and convergence results of the navigation filter are presented in Subsection 7-1-3 Subsection 7-1-4 and respectively.

7-1-1 Star Tracker Implementation

For this section, the star tracker sensor has been implemented into the navigation filter, using the measurement simulation from Section 5-3 and the measurement update equations as described in Subsection 6-2-1. In Figure 7-1, the effect of the star tracker measurement update on the position estimation is presented. In the left column, the propagation of the true state simulation, the navigation filter estimation with star tracker measurement update, and the navigation filter estimation without any measurement update are plotted. The navigation filter without any measurement update only consists of the state space update as described in Section 5-1, and is therefore referred to as the time update. As can be seen in the middle and right column, the error of the Kalman filter with star tracker measurement update is as large as the error of the time update. Hence, the Kalman and time update results in the left column overlap. It can be seen that the implementation of the star tracker measurement update does not improve the estimation of the spacecraft position, and the navigation filter is not able to estimate the spacecraft position.

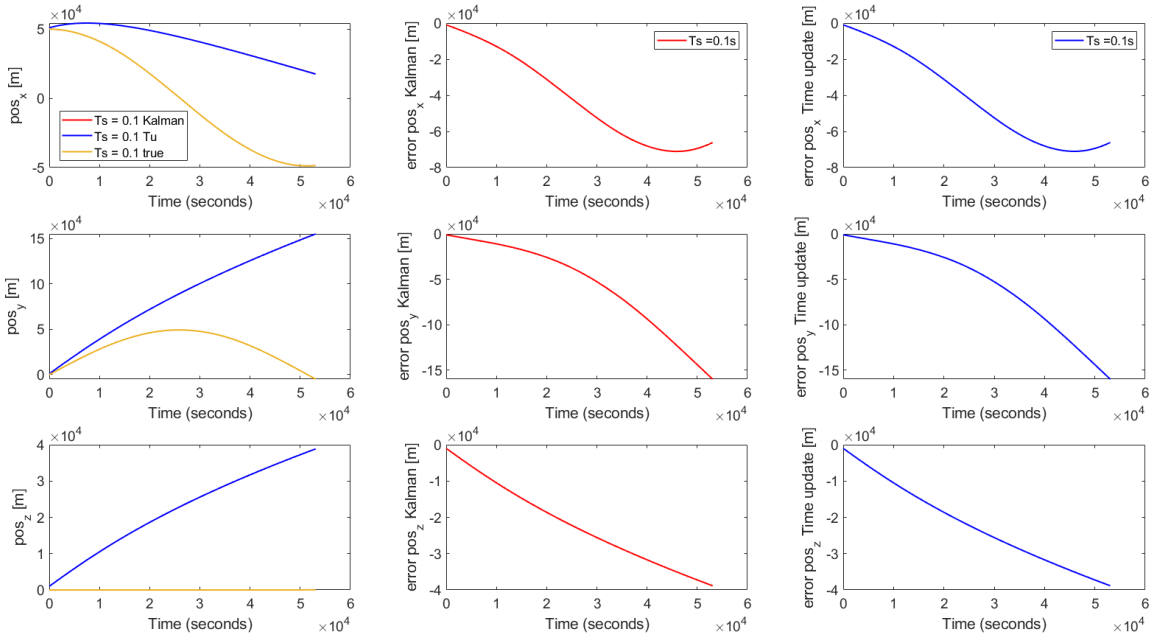

Figure 7-1: True state position propagation for time step of 0.1s [left column], error between true state simulation and Kalman results for star tracker measurement update only, [middle column], and error between true state simulation and time update results [right column].

Contrarily, improvement of the attitude estimation is visible for the star tracker measurement update, as seen in Figure 7-2. It can be seen that the error in the time update accumulates over time, whereas the errors for the star tracker measurement update are noisy, but have a constant error. Implementing the star tracker measurement is therefore necessary to estimate the spacecraft attitude.

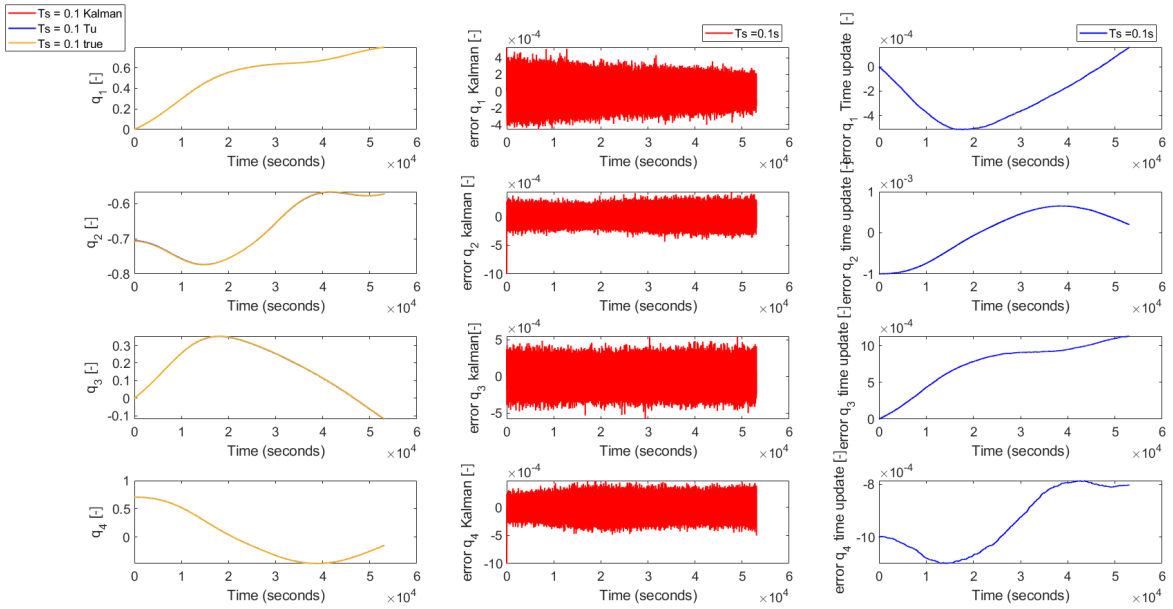

Figure 7-2: True state quaternion propagation for time step of 0.1s [left column], error between true state simulation and Kalman results for star tracker measurement update only, [middle column], and error between true state simulation and time update results [right column].

7-1-2 LiDAR Implementation

Similar to the previous section, the performance of implementing one sensor is presented. For the implementation of the LiDAR sensor, the measurement simulation from Section 5-4 and the measurement update equations as described in Subsection 6-2-2 have been used.

Again, the error of the navigation filter with the measurement update has been plotted in comparison to the error of the time update. The propagation of the position has a smaller error than for the time update, as presented in Figure 7-3. It can be seen that for the time update, the error grows larger over time. The errors for the navigation filter with the LiDAR measurement update included do not go over 15 m for each axis. Hence, the true state simulation and the navigation filter results overlap in the left column.

However, as can be seen in Figure 7-4, the quaternion estimation for the LiDAR measurement update shows the same performance as for the propagation of only the time update. Therefore, no influence of the LiDAR measurement update is detected on the performance of the attitude estimation of the navigation filter.

Based on the results on the position in Figure 7-3, it is visible that the implementation of the LiDAR is necessary for estimating the position of the spacecraft. The same result can be found for the velocity estimation, which can be found in Appendix D.

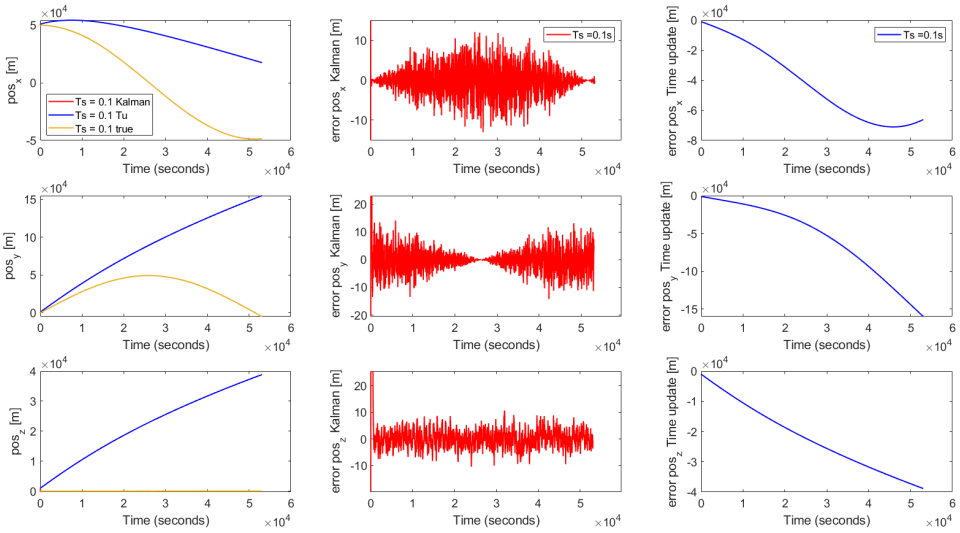

Figure 7-3: True state position propagation for time step of 0.1s [left column], error between true state simulation and Kalman results for LiDAR measurement update only, [middle column], and error between true state simulation and time update results [right column].

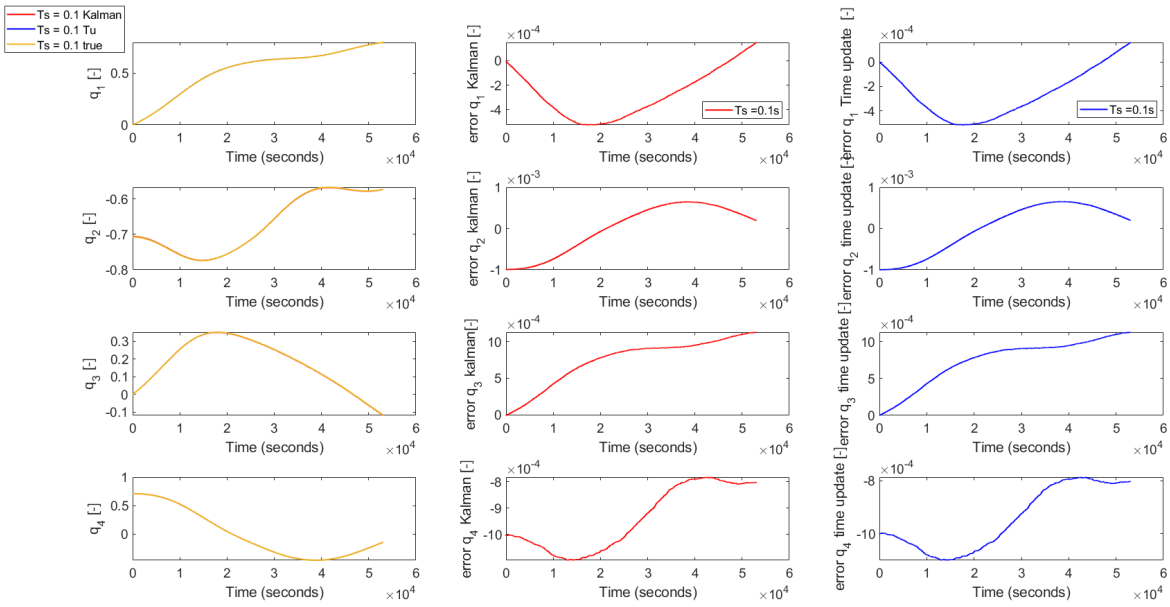

Figure 7-4: True state quaternion propagation for time step of 0.1s [left column], error between true state simulation and Kalman results for LiDAR measurement update only, [middle column], and error between true state simulation and time update results [right column].

7-1-3 Position Estimation Covariance

The results presented in this section are based on the estimation of the complete navigation filter described in Section 6-1, where both measurement updates have been implemented.

In Figure 7-5, the estimated and true state position have been plotted in the inertial reference frame in the left column. In the right column, the error between the true state and the estimated states are plotted. The variance of the position estimation, for 1σ and -1σ has been plotted in the right column as well. It can be seen that for all three axes, noise is present in the error between the true state and the navigation filter estimation.

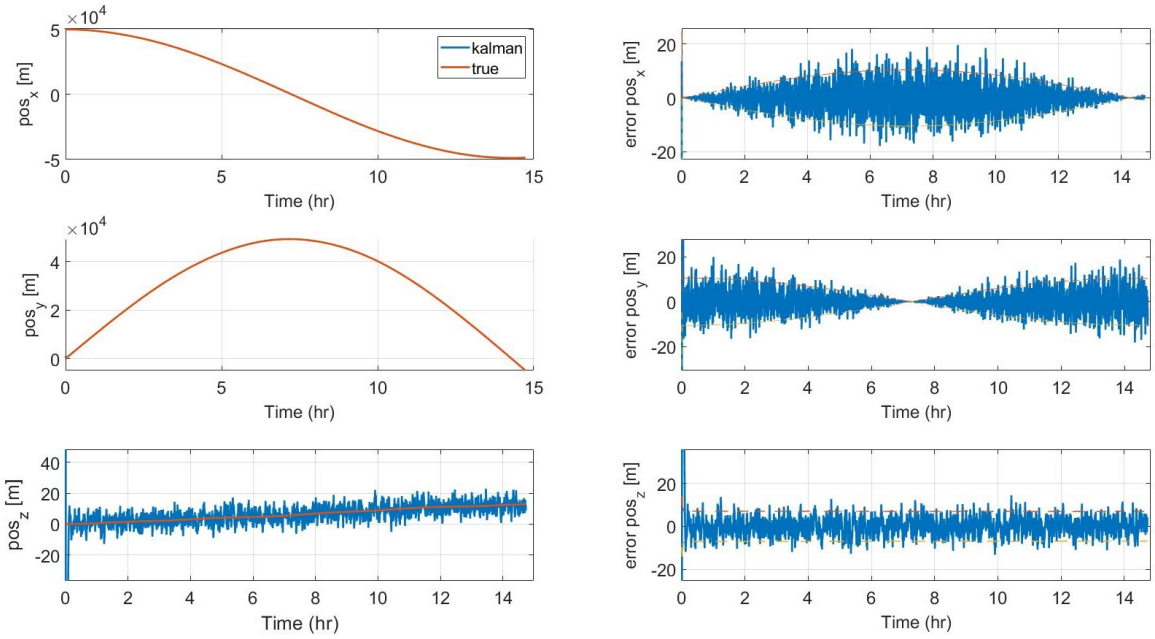

Figure 7-5: True and estimated position propagation, for time step = 0.01s, inertial frame.

The errors and the covariance for the position in the x- and y-axis display sinusoidal behaviour. A similar result is seen for the velocity estimation plot, shown in Figure 7-6. Contrary to the other axes, the covariance and the error of the position in the z-axis have an apparent constant level.

The covariance, and the size of the errors, is changing along with the direction of the orbital velocity. At the starting point of the orbit, the position in x-direction is aligning with the radial component of the spacecraft velocity. The tangential component of the velocity is in the y-direction of the inertial frame. Therefore, the navigation filter has a higher accuracy and confidence of the position estimate in the x-axis than for in the y-axis. This interchanges when the position has been propagated for a quarter orbit, int the middle of the position plot in Figure 7-5. Now, the velocity is tangent to the x-axis, and the accuracy and confidence of the position estimate is lower in the x-axis than in the y-axis.

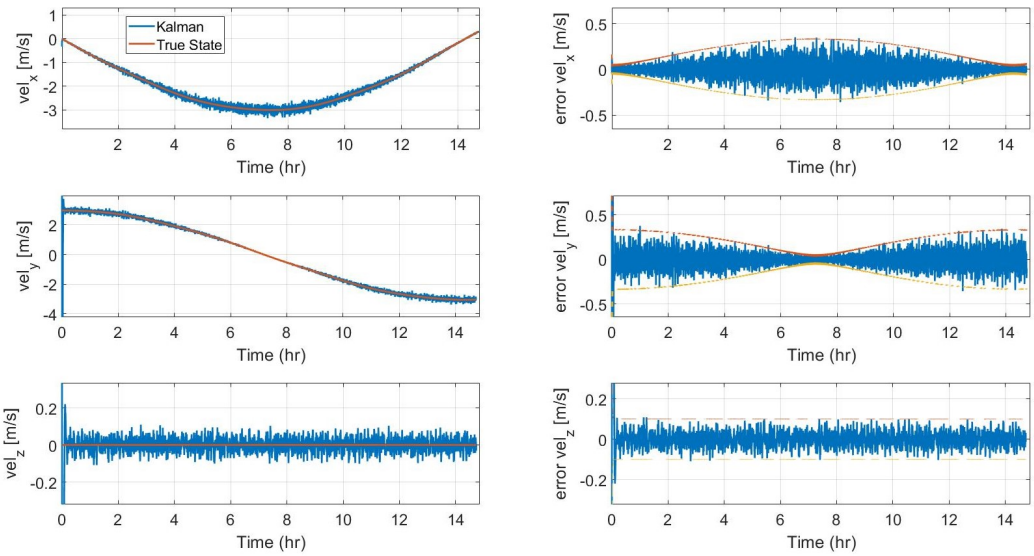

Figure 7-6: True and estimated velocity propagation, for time step = 0.01s, inertial frame.

7-1-4 Navigation Filter Convergence

In order to analyse the convergence time, the position propagation plots have been cut off near the point of convergence for each axis. This is plotted in the left column figures of Figure 7-7, where the right column shows the error between the true and estimated state. It can be seen that for all axes, there is an initial error of 1 km, corresponding to the initial estimated state.

In Figure 7-8, the convergence of the velocity states is shown. The convergence for the velocity states is the same as compared to the position convergence, except for the velocity in the x-direction. Here, the convergence of the velocity estimate takes 100 s to become stable, instead of 0.01 s before the position estimate in the x-direction becomes stable.

In addition, the convergence of the innovation sequences of the LiDAR are shown in Figure 7-9. In the top figure, the innovation sequence for the range is shown, the azimuth and elevation in the middle figure, and the quaternion errors in the bottom figure. The x-coordinate converges at the same time as the range (top figure), whereas the y- and z-coordinates converge with a similar time to the control angles (bottom two figures). The range innovation sequence is already converging for one time step which is very fast, especially compared to the innovation sequence convergence of the control angles which is in the order of 300 s.

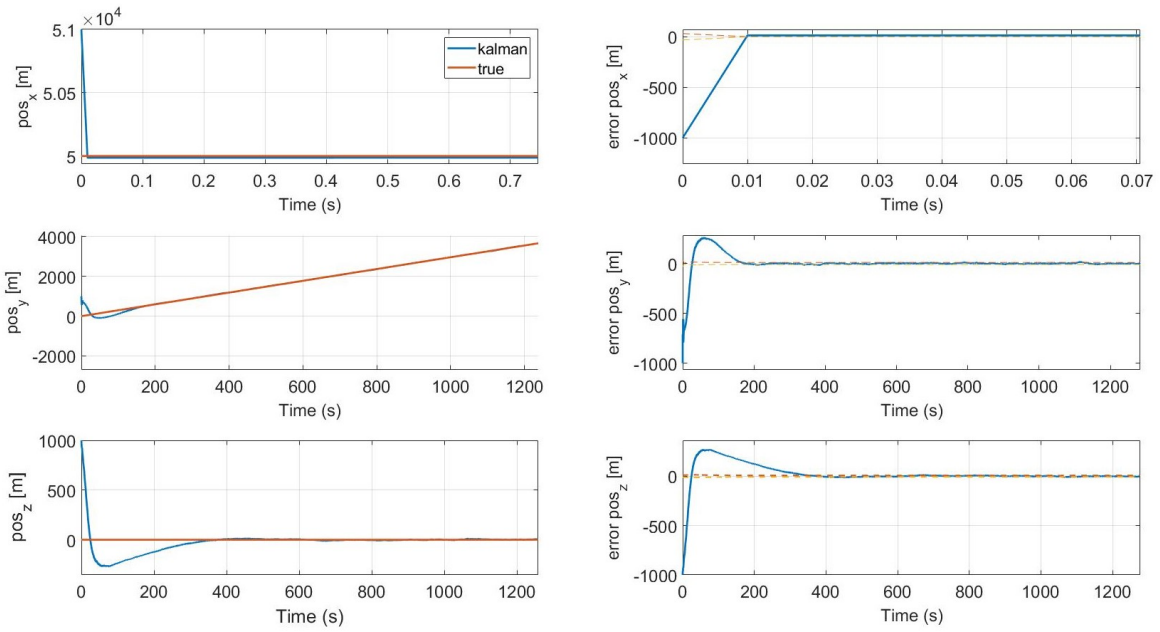

Figure 7-7: Convergence for position estimation, 0.01s time step.

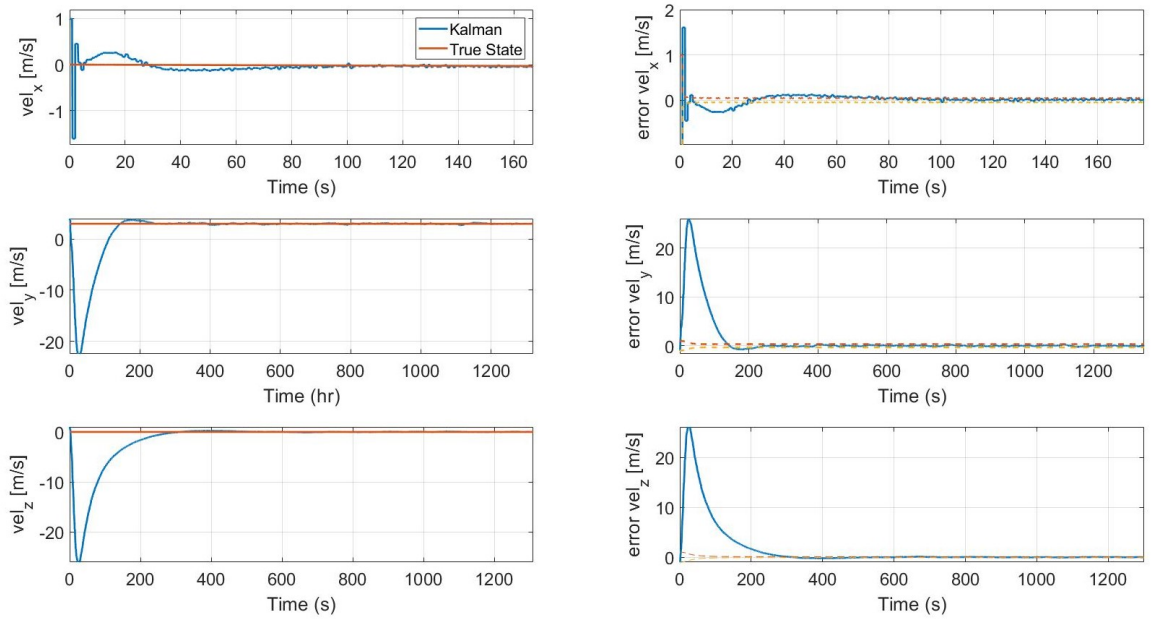

Figure 7-8: Convergence for velocity estimation, 0.01s time step.

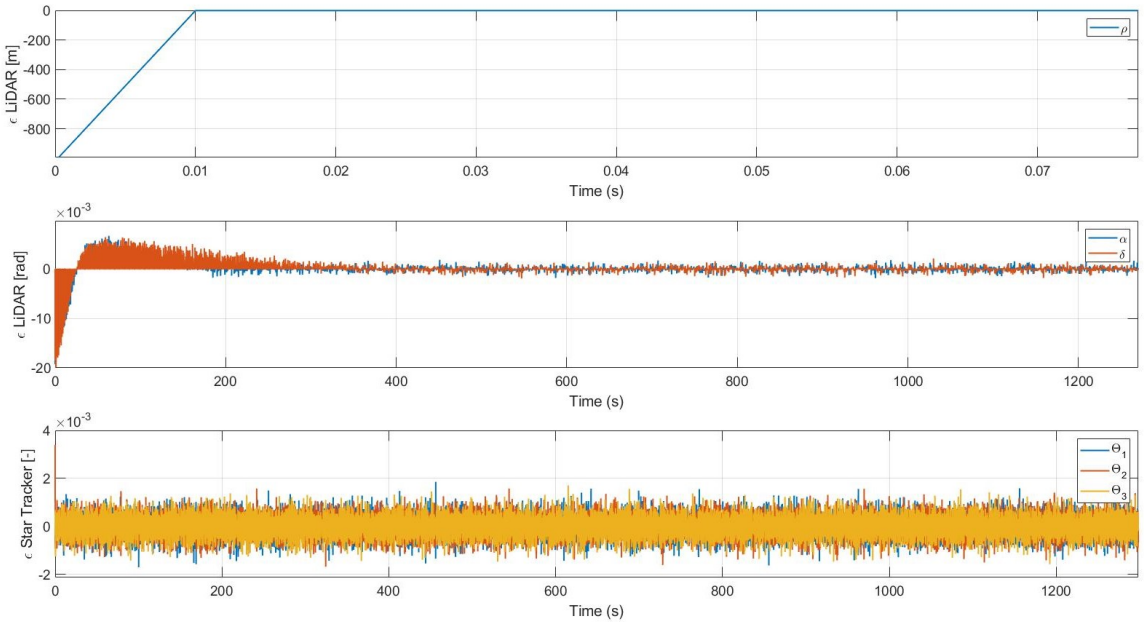

Figure 7-9: Innovation sequence convergence, 0.01s time step.

7-2 Sensor Loss

The last set of results is based on a scenario where there is a temporary loss for two of the sensors. At 30% of the simulation time, the star tracker sensor experiences a 'loss' for 2000 seconds, and no measurement is send to the navigation filter. Similarly, at 60%, the same happens to the LiDAR sensor, for the same amount of time. Beyond a loss of 2000 s, the navigation filter was not able to overcome the accumulated covariance values to have convergence of the position or attitude estimation. Hence, 2000 s was set as the maximum possible loss duration. The results for the position estimation is plotted in Figure 7-10. It can be seen that during the loss of the LiDAR measurement, the error as well as the covariance (dotted) of the position grows exponentially. When regaining the position measurement, the errors decrease to their nominal state.

It can be seen that for the computation of the innovation sequence values in Figure 7-11, the value drops for the range estimation at the same time that the measurement update is performed after the LiDAR loss. This corresponds to the position offset that is seen in Figure 7-10. Because of the time update steps performed during the loss of the LiDAR, the position estimate has drifted from the true state simulation. Upon regaining signal from the LiDAR, an error of 14 m for the range is found, which is visible in the upper plot of the innovation sequence in Figure 7-11.

It can also be derived from the innovation sequence plot for the star tracker measurement update that there is temporarily no computation of the innovation sequence for the star tracker loss. However, there appears to be no error accumulating for the quaternion estimation, based on the results shown in Figure 7-12.

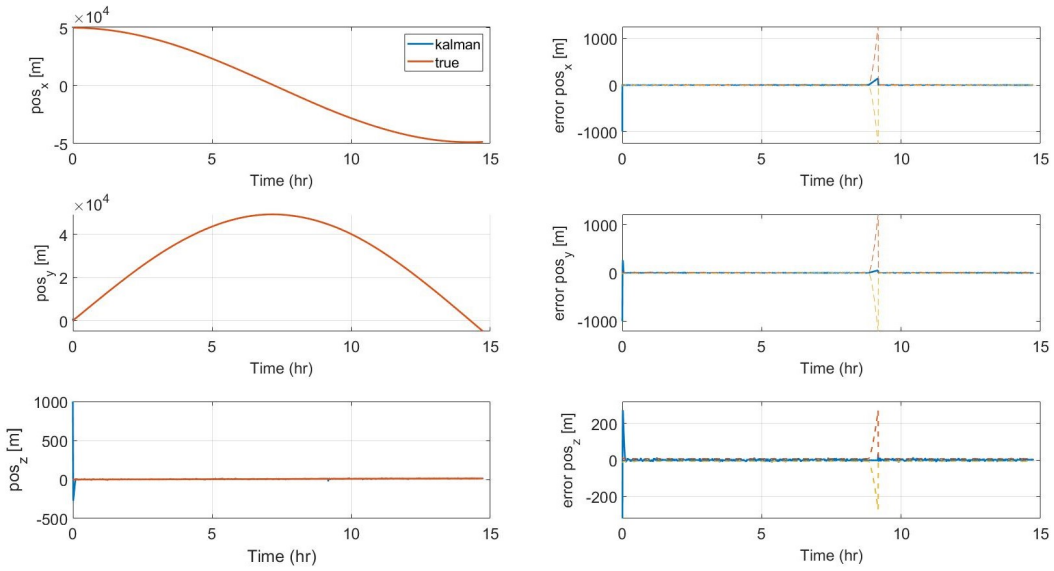

Figure 7-10: True and estimated position propagation with sensor loss, for time step = 0.01s, inertial frame.

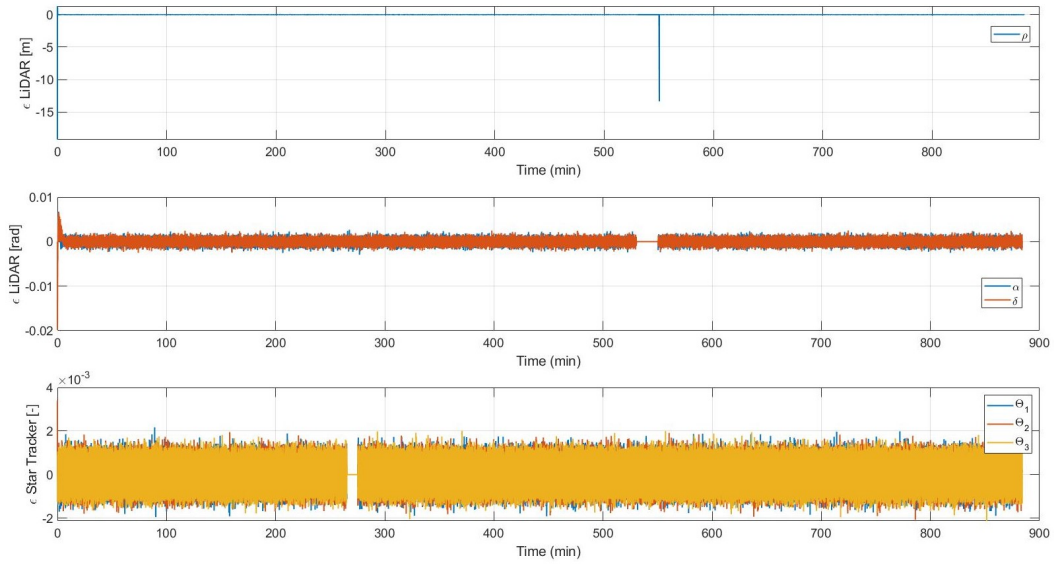

Figure 7-11: Innovation sequences for propagation with sensor loss for time step = 0.01s, inertial frame.

The results for the root-mean-square error (RMSE) computation for the position estimation has been summarised in Table 7-2. It can be seen that a significant increase in accuracy is obtained when reducing the time step of the navigation filter computation from 1 s to 0.1 s. The results for decreasing the time step from 0.1 s to 0.01 s are not improving for the accuracy. This is due to the increased error for the x-coordinate of the position.

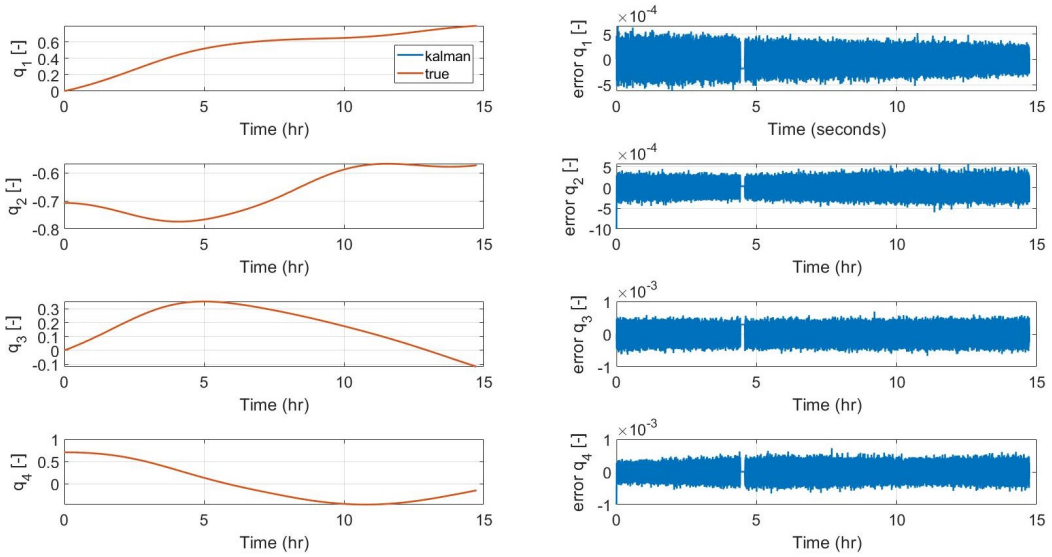

Figure 7-12: True and estimated quaternion propagation with sensor loss, for time step = 0.01s, inertial frame.

Table 7-2: RMSE values for position in sensor loss scenario.

Time step	RMSE r_x	RMSE r_y	RMSE r_z	RMSE $\mathbf{r}$
1s	222.9260	147.7388	2.4260	267.4484
0.1 s	0.9921	0.2437	0.8989	1.3607
0.01 s	1.2693	0.8873	0.1613	1.5571

7-3 State Estimation Accuracy for Multiple Step Sizes

For this section, the benchmark scenario has been propagated with different step sizes for the navigation filter. As a measure of accuracy, the RMSE has been computed using

$$\text{RMSE} = \left[\sum_{i=1}^{N} \frac{(d_i - \hat{d}_i)}{N}\right]^{\frac{1}{2}} \tag{7-1}$$

where N is the amount of data points, d_i is a true state value and $\hat{d}_i$ is the corresponding estimated value by the KF. The resulting values are visible in Figure 7-13. For the benchmark scenario, a time step of 0.01 s was taken. It is taken into account that the simulation of the true state has been performed with the same time step of the benchmark. The same true state data of the benchmark scenario is thus given to all navigation filters. The RMSE values appear to be the lowest for the position estimation in the z-direction. However, as shown in Figure 7-5, the values of the z-component are much smaller than as for the components in the other two axes, as we are dealing with an equatorial orbit. Given that the maximum value of the z-coordinate is no larger than 20 m, an RMSE value of 12 m for a time step of 1000 s is an offset of more than 50%. Compared to the position estimates in x- and y-direction, the offset is never more than 2.25%, irrespective of the selected time step.

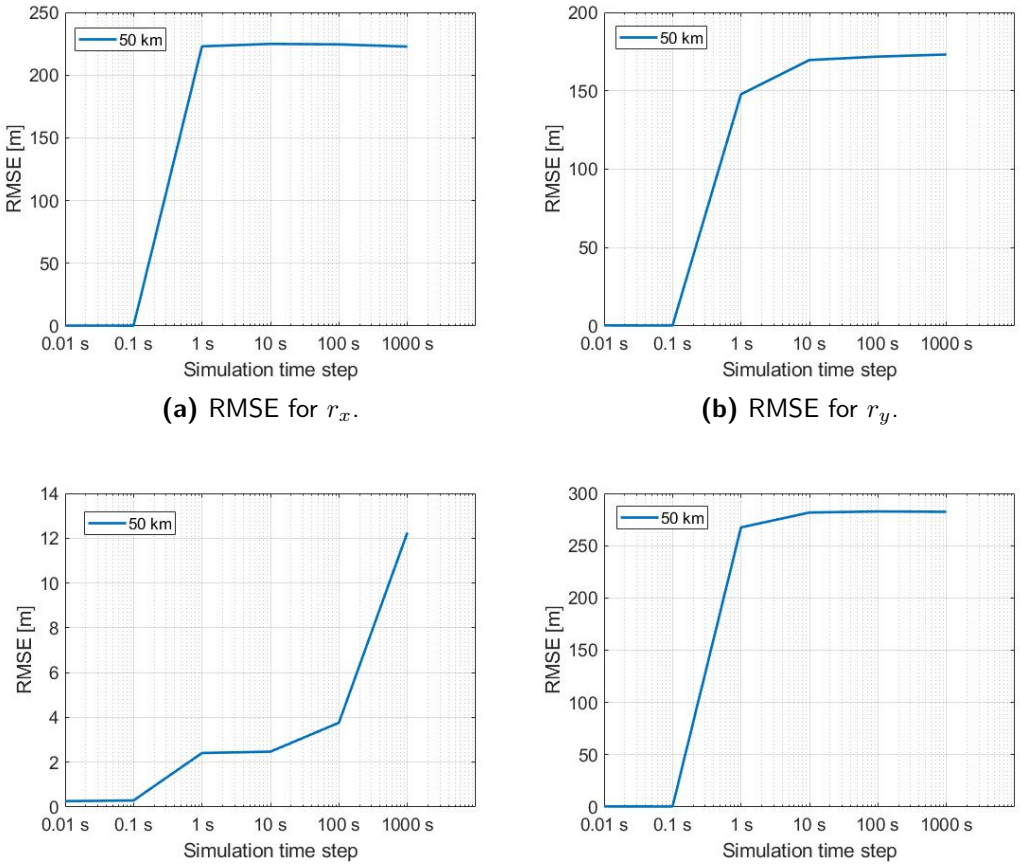

(a) RMSE for r_x.

(b) RMSE for r_y.

(c) RMSE for r_z.

(d) RMSE for $\mathbf{r}$.

Figure 7-13: RMSE values for propagation of the benchmark scenario, for time steps 1000, 100, 10, 1, 0.1, and 0.01 s.

Next to the RMSE values of the position, the RMSE has also been computed for the velocity and the quaternion attitude of the benchmark scenario. The plots are shown in Figure 7-14. Again, a drop in RMSE values can be seen from the 1s to 0.1 s time step for both the velocity as well as the attitude estimation.

In addition to the RMSE figures, the RMSE values have been summarised in Table 7-3, together with the measured computational time of one arbitrary simulation of the benchmark for each time step. Based on the position error plots with respect to the time step of the navigation, it could be seen that the best improvement of accuracy performance is when decreasing the time step from 1s to 0.1 s. The difference in error between the 0.1 and 0.01 s time step is the smallest, 0.07 m, while the computational effort of the navigation filter increases the most. The computation time becomes 24 times larger for decreasing the time step from 0.1 s to the 0.01 s.

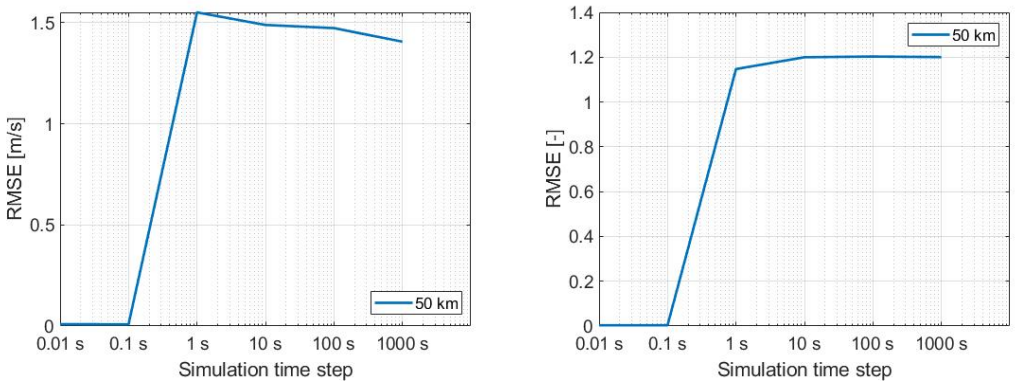

(a) RMSE for velocity.

(b) RMSE for quaternion.

Figure 7-14: RMSE values for the velocity and quaternion propagation of the benchmark scenario, for time steps 1000, 100, 10, 1, 0.1, and 0.01 s.

Table 7-3: Simulation results for different time steps

Time step	RMSE position [m]	RMSE attitude [-]	Computation time [s]
1000	282.3709	1.2004	2.6521
100	282.7010	1.2029	2.3000
10	281.6756	1.1997	8.65125
1	267.4513	1.1470	71.1188
0.1	0.5289	0.003531	692.8675
0.01	0.5889	0.003490	16933.3309

7-4 Orbit Proximity

Next to the benchmark scenario, two other scenarios have been simulated, where the orbital height has been adjusted. Different orbital heights of 35 km and 100 km have been simulated, for which the initialisation settings are summarised in Table 7-4. For both the 35 km and 100 km altitude orbit, the offsets of the Kalman filter have been kept the same. Furthermore, the values of the covariance, process noise, and measurement noise matrices have been kept the same as for the benchmark scenario.

The orbit trajectories have been visualised in Figure 7-15. In the left figure, the propagation of the orbit of 35 km is plotted for a simulation time of 53050 s, with the spacecraft enlarged by 200 times. The same settings are used for the trajectory of the 100 km orbit, which is shown in the right figure.

In Figure 7-16, the RMSE values have been plotted with respect to different simulation time steps, for the three different orbital heights. For clarification, only the three smallest time steps have been plotted in Figure 7-16b. It can be seen that for the smallest time steps, the orbital height of 50 km has the lowest RMSE values. It is noticeable that from the 1s to 0.1 second time step, the plots of the 35 and 50 km orbit cross each other. For the larger time steps, the 35 km orbit has lower RMSE values than for the 50 km orbit.

For comparison, the position RMSE values for the three different orbital heights have been summarised in Table 7-5. Irrespective of the orbital height, only the simulations with a time

Table 7-4: Initial conditions of estimating benchmark scenario

	True State	Estimated State
	35 km orbit	
$\mathbf{r}_I$ [km]	$\begin{bmatrix}35 & 0 & 0\end{bmatrix}^T$	$\begin{bmatrix}36 & 1 & 1\end{bmatrix}^T$
$\mathbf{v}_I$ [km]	$\begin{bmatrix}0 & 3.539 & 0\end{bmatrix}^T$	$\begin{bmatrix}1 & 4.539 & 1\end{bmatrix}^T$
$\mathbf{q}_{B/I}$ [km]	$\begin{bmatrix}0 & -0.707 & 0 & 0.707\end{bmatrix}^T$	$\begin{bmatrix}0 & -0.7071 & 0 & 0.7071\end{bmatrix}^T$
$\mathbf{\Theta}_{B/I}$ [km]	$\begin{bmatrix}0 & 0 & 0\end{bmatrix}^T$	$\begin{bmatrix}1\cdot10^{-7} & 1\cdot10^{-7} & 1\cdot10^{-7}\end{bmatrix}^T$
	100 km orbit	
$\mathbf{r}_I$ [km]	$\begin{bmatrix}100 & 0 & 0\end{bmatrix}^T$	$\begin{bmatrix}101 & 1 & 1\end{bmatrix}^T$
$\mathbf{v}_I$ [km]	$\begin{bmatrix}0 & 2.094 & 0\end{bmatrix}^T$	$\begin{bmatrix}1 & 3.094 & 1\end{bmatrix}^T$
$\mathbf{q}_{B/I}$ [km]	$\begin{bmatrix}0 & -0.707 & 0 & 0.707\end{bmatrix}^T$	$\begin{bmatrix}0 & -0.7071 & 0 & 0.7071\end{bmatrix}^T$
$\mathbf{\Theta}_{B/I}$ [km]	$\begin{bmatrix}0 & 0 & 0\end{bmatrix}^T$	$\begin{bmatrix}1\cdot10^{-7} & 1\cdot10^{-7} & 1\cdot10^{-7}\end{bmatrix}^T$

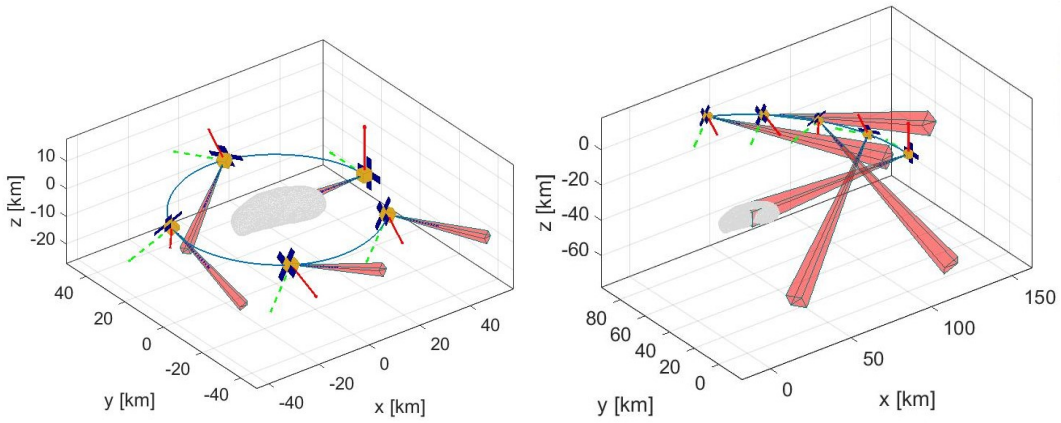

(a) 35km km orbit. **(b)** 100 km orbit.

Figure 7-15: Proximity operation orbits for 53050 s, time step - 0.01 s.

step of 0.1 or 0.01 s are able to achieve a position error below 1 m. The difference in error between 0.1 s and 0.01 time step simulation increases slightly with larger orbital height, as the difference comes down to 0.02 m, 0.06 m, and 0.16 m for 35 km, 50 km and the 100 km orbit respectively. Based on this data set, the increase in error is however not proportionate to the increase in orbital height .

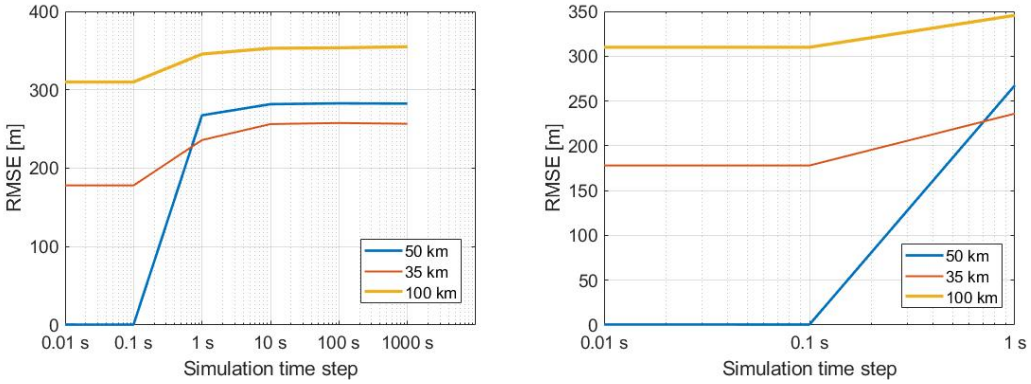

(a) Time steps 0.01, 0.1, 1, 10, 100, and 1000 s.

(b) Time steps 0.01, 0.1, and 1 s.

Figure 7-16: Position RMSE over propagation for different computation time steps, for an orbit of 35, 50 and 100 km.

Table 7-5: Simulation results RMSE position [m] for different time steps for an orbit of 35 km, 50 km, and 100 km.

Time step	35 km orbit	50 km	100 km orbit
1000	259.5937	282.3709	265.3527
100	257.9264	282.7010	262.4526
10	256.2722	281.6756	261.4934
1	235.8991	267.4513	251.4264
0.1	0.4025	0.5289	0.5165
0.01	0.4253	0.5889	0.6715

Chapter 8

Discussion

This chapter presents the discussion that is based on the results presented in the previous chapter. To begin with, Section 8-1 presents a discussion on the limitations of the implemented sensor set. In Section 8-2, the interpretations on the performance of the navigation filter for the benchmark scenario are discussed. Next, the effect of the simplifications of the true state simulation are discussed in Section 8-3. After, the findings of the proximity operations for different orbital heights are discussed in Section 8-4. The last section, Section 8-5, discusses what the results of the simulations for different time steps impose on the performance of the state estimation.

8-1 Sensor Implementation

In this section, various aspects of the chosen sensor set and the error modelling are discussed. To start, the limitations of the sensor set is discussed in Subsection 8-1-1. Next, the results for the sensor loss are discussed in Subsection 8-1-2. Similar to the assumptions for the true state model, assumptions have been made for each sensor model. Especially simplifications of the error characteristics per sensor can make the outcomes of the navigation filter unrealistic. The explicit limitations for each sensor type are discussed in Subsection 8-1-3.

8-1-1 Sensor Set Selection

In total, three sensors and their respective measurement outputs are simulated for the navigation filter. With 433 Eros as the target asteroid, it was known beforehand that there was no magnetic field found in the proximity of the asteroid, which posed limitations on the available sensors. Compared to the sensor set of Razgus (2016) and Bourgeaux (2020), the IMU sensor model is now more complete as both the accelerometer and the gyroscope have now been implemented. Additionally, the implementation of different output rates was not encountered in the sensor models described by Bourgeaux (2020), Spee (2022) and Razgus

(2016). Implementing the lower output rates for the measurement updates does imply a more realistic sensor output.

As could be derived from the comparison of the Kalman filter (KF) with and without measurement updates, the star tracker and the light detection and ranging (LiDAR), and their respective the measurement updates, are necessary to compensate for initial offsets in the state estimation. The rank for the LiDAR measurement update was checked for the implementation of the measurement matrices, which resulted in a rank of 10. This result caused the expectation that coupling occurs between the attitude estimates and the position and velocity estimates. However, as was seen Figure 7-4, the influence of the LiDAR measurement update on the attitude estimation is negligible. Since the LiDAR measurement update contains a measurement matrix that is based on the position, it is no surprise that the position is converging first in Figure 7-7, after which the velocity follows. It could be seen that the convergence of the position in all axes is corresponding with the innovation sequence of the LiDAR in Figure 7-9.

8-1-2 Sensor Loss

For the simulated sensor loss, a constant loss of either the star tracker or the LiDAR for the same amount of time but at different points in the trajectory, was simulated and presented in Figure 7-10 and Figure 7-11. It could be deduced from the results that the dynamic model is able to propagate the dynamics and kinematics when either the LiDAR or star tracker is unable to provide measurements for about half an hour. For longer interruptions, the system is not able to overcome the large error and large uncertainty of the time step propagation. This conclusion is of course only applicable to the benchmark scenario, and could be subjected to different orbital scenarios. Especially for unstable orbits, it would be interesting to know whether the previously made conclusion is still true.

Furthermore, it was seen that the error for sensor loss was larger for the time step of 0.01 s than for a time step of 0.1 sec. One possible explanation for the lower performance is that for the time step of 0.1, the output rate of the IMU is now equal to 10 Hz instead of 100 Hz. Although the accuracy for those time steps is similar, the 0.01 s updates the time step more often in between star tracker or LiDAR measurements. Per time update, more uncertainty can accumulate in the covariance matrix. Although the values in the covariance matrix are influenced by the time step size, it is not certain whether this is a linear relation. To know for sure, more analysis of the size of the covariance matrix for different time steps is needed, as well as the influence of the output rates for a navigation filter with a time step of 0.1s.

Another critical point for the sensor error scenario is whether the scenario is realistic to happen for actual sensors. Now, a loss of the sensor has been simulated, which is not necessarily equal to what can happen during a mission. It is more likely that the sensor measurements are faulty, such as what happened for the Rosetta star tracker when flying close to the debris of the tail of a comet (Siddiqi, 2018).

8-1-3 Inertial Measurement Unit Simulation Limitations

It is expected that for real sensors, the measurements contain more distinctive errors, or at least deviating more from classical white noise errors. Only incorporating two error types

for the IMU has been shown to be realistic to a certain extent, but can be improved when comparing to the error characterisation on IMU fact sheets (Systems, 2014), (Sensors and Power AG, 2021), (Corporation, 2012). There are various studies that have implemented more detailed IMU models. The integration and verification of these type of models were, however, beyond the time scope of this thesis research. By incorporating more errors in the measurement simulation, the performance of the navigation filter can decrease. This is because Kalman filters work optimally for white noise errors. However, this allows for introducing additional states in the state space vector that estimate the error for the IMU measurements. This can then increase the performance of the navigation filter again.

8-1-4 Star Tracker Simulation Limitations

As expected, the star tracker measurement update in combination with the gyroscope output ensures that the quaternion states are propagated with minimal errors, and that for initial offsets, the star tracker measurement update is able to account for those. Thus, the real-life necessity of IMU calibration can be solved with the use of a star tracker.

However, it has been concluded from other literature that tightly-coupled systems perform better than loosely coupled ones. Star trackers automatically come with a pre-processing algorithm that detects the star based on an onboard map. One of the example star tracker model extensions discussed was from Marin and Bang (2020). As was mentioned in Chapter 5, further development of the star tracker measurement model was beyond the scope of the research.

These findings suggest that the filter could have been more tightly coupled and thus providing more accurate estimates, but on the other hand the filter would also be handling more erroneous measurements for the star tracker. Similar to the IMU model, more detailed measurement simulation is expected to cause more errors for the state estimation.

8-1-5 LiDAR Simulation Limitations

There is a limitation to the LiDAR model in the sense that the control angles of the LiDAR are assumed known, such that the range is accompanied by the azimuth and elevation angle. This is of course a simplified model, which also does not into account that the distance between the geometric centre of the asteroid and the point where the laser hits should be subtracted from the range. Although Bourgeaux (2020) also included control angles as measurements in their measurement update, they are not used in the measurement equations, but only for pre-processing of the LiDAR measurement. Implementing this method however makes the navigation filter less tightly coupled, which is not desired. Using only the range measurement, $\tilde{\rho}$ from the LiDAR does not give enough information about the position, as the rank for the observability of the measurement update decreases to 8. Therefore, the control angle measurements cannot be omitted. It could be researched whether the control angles can be expressed differently or if different information from the LiDAR can be used in measurement matrices, and what the effect of the new implementations are.

Furthermore, it can very well happen that there is not always a clear view on the asteroid such that there is no information about the range at that point, as well as the control angles.

It is therefore of importance to know how long the model can operate without input from the LiDAR. It could be seen that for a sensor loss of 2000 s, the navigation filter was able to overcome the accumulated error of the position.

In the research of Razgus (2016) or Bourgeaux (2020), landmark tracking by use of a navigation camera combined with LiDAR sensing is used to map the surface of a target asteroid. Although the model of the LiDAR in my case is more simple, it has been proven that only one sensor for position estimation is necessary for the navigation filter to function. Still, the measurement simulation has to deal with the offset between the centre of the asteroid and where the LiDAR beam hits the surface of the asteroid. For this, an approximation of the asteroid surface height is needed for the measurement update in the navigation filter.

8-2 Navigation for the Benchmark Scenario

In this section, the performance of the navigation filter used to estimate the states in a benchmark scenario is discussed. The findings based on the results in Section 7-1 will be discussed through three main topics. First, the coupling of the states for the state space model are discussed in Subsection 8-2-1. Second, the covariance characteristics of the navigation filter are interpreted and explained in Subsection 8-2-2. Third, the accuracy of the navigation estimates are discussed in Subsection 8-2-3.

8-2-1 Coupling of the State Space Equations

Since the state space matrix derived in Section 5-1 was equal to

$$\mathbf{F}_k = \begin{bmatrix} \mathbf{0}_{3\times3} & \mathbf{I}_{3\times3} & \mathbf{0}_{3\times3} & \mathbf{0}_{3\times1} \\ \frac{\partial \dot{\mathbf{v}}_{I,k}}{\partial \boldsymbol{r}_{I,k}} & \mathbf{0}_{3\times3} & [\tilde{\boldsymbol{\omega}}^B_{B/I,k}]_\times \tilde{\mathbf{a}}_k & \frac{\partial \dot{\mathbf{v}}_{I,k}}{\partial \mu_k} \\ \mathbf{0}_{3\times3} & \mathbf{0}_{3\times3} & [\tilde{\boldsymbol{\omega}}^B_{B/I,k}]_\times & \mathbf{0}_{3\times1} \\ \mathbf{0}_{1\times3} & \mathbf{0}_{1\times3} & \mathbf{0}_{1\times3} & \mathbf{0}_{1\times1} \end{bmatrix}_{x_k}, \tag{8-1}$$

it can be deduced that coupling takes place for the derivation of the velocity, which is dependent on the measured accelerations by the IMU. These accelerations are converted to the inertial frame using the quaternion attitude, and thus also dependent on the error states.

For measurements simulation without white noise, the measured accelerations would even decrease to the order of 10^{-8}, as the SRP acceleration is of this magnitude. Although the method of defining the state space matrix equations in the inertial reference frame such that the accelerations are converted using the spacecraft orientation, the effect of the coupling is not as influential as was previously expected. Although defining the state space equations in the asteroid reference frame did make the equations and their derivatives more complicated, the coupling was more evident for the navigation filter by Razgus (2016). If it is desired to keep the more simple state space equation in the inertial reference frame, the coupling could become more apparent if larger non-gravitational forces would be present in the simulation environment. This can for instance be obtained by introducing accelerations due to thruster force of the spacecraft control system.

It is also noticed that the general performance of the navigation filter provides converging results for all states as seen in Figure 7-7 and Figure 7-8, despite of the scaling of the filter. Only for the quaternion state, a MEKF was implemented, as this was necessary to avoid issues with the unit property of the quaternions. However, it is likely that there is bad scaling in the state transition matrix. At the moment, the values for the position state are very large, especially compared to the error states of the quaternion.

8-2-2 Covariance Behaviour

One of the peculiar observations of the performance of the benchmark scenario is the sinusoidal behaviour of the errors and covariance of the position in the x- and y-axis. Where for the x-axis, the error increases and decreases when passing half of the trajectory (thus, a quarter of the orbit), the error in the y-axis starts with a larger value, decreases, and increase at the same pivotal point. This was due to the high confidence in the radial aspect of the position and velocity, and the low confidence in the tangential aspect of the position and velocity of the spacecraft. When changing the benchmark orbit by setting the inclination to 90 degrees, such that the trajectory follows an orbit along the zx-plane, the error and covariance of the z-coordinate also appears to be sinusoidal. Thus, the error and covariance again grow due to the larger uncertainty in the tangential direction of the orbit trajectory. The figure to analyse the behaviour of the position error and covariance can be found in Appendix E.

8-2-3 Accuracy of the Navigation Filter

The resulting errors for the position and attitude estimation for the benchmark scenario can be compared to the results obtained in previous thesis researches. As for previous theses the simulation time step was set at 1s, the error values for these simulations are considered first.

Spee (2022) was able to obtain errors in position in the order of 1 to 15 m, which is well below the results as seen in Table 7-3. However, they introduced measurement states by adding white noise to the position coordinates of the true state simulation. Furthermore, the orientation states were not estimated, and a transformation matrix was assumed available from the inertial to the asteroid reference frame. It is therefore not surprising that it is possible for Spee (2022) to have a higher accuracy for similar settings of orbital height. In addition, by estimating the gravitational field of the asteroid in more detail for the navigation filter, it should be possible to have more accurate estimates of the position and velocity as well. This is also seen in comparison to Bourgeaux (2020) with the implementation of a spherical harmonics estimation in the navigation filter. They were able to estimate the spacecraft position with a precision below 0.5 m for every axis at an orbital distance of 30 km for an EKF.

Furthermore, there are less uncertainties in the navigation filter of Bourgeaux (2020). The SRP is already given as a term to be added in the state space equations, and the third body acceleration computation is also added to the state space equations as well. On the other hand, although it is assumed for this research that the disturbance forces are not known, and thus not in the state space equations of the navigation filter, these disturbances are still relatively small. The offset due to the third body perturbation as demonstrated in Subsection 4-5-3 is

only in the order of 2 to 3 m. For the SRP, the disturbing acceleration is even smaller than for the third body disturbance.

Nonetheless, the current unpredictable forces are predominantly caused by the asteroid gravity field. The true state and measurement states are both simulated, and we can exactly know the difference between the true state and the computed states of the navigation filter. This is different from reality as there is not such as distinctive difference between true and estimated state. As we know every force that is simulated in the true state, the errors can be accounted for and the tuning of the filter corresponds to the dimension of the errors that we chose to simulate.

8-3 True State Simulation

The true state simulation model has several constraints, of which the most important are

- a simplified polyhedron model is taken for the gravity acceleration computation;
- only the SRP and Sun third body are introduced as disturbance forces;
- a constant rotation of the asteroid about its z-axis is assumed;
- the density distribution of the asteroid is assumed to be homogeneous.

Although the volume of the polyhedral only deviated by 0.02% for the simplified model, even minor changes in the shape of the asteroid can cause different accelerations exerted on the spacecraft. Moreover, by having multiple simplifications of the asteroid and its gravity field, the accumulation of deviations from the actual values can cause a significant deviation for the true asteroid environment. It is not exactly known what the error in true state simulation is between this simplified model and a model where the aforementioned simplifications have not been applied. Of course, a real true asteroid model can never be obtained as everything we know about the asteroid is also based on measurements with a certain accuracy. However, the currently implemented true state model could certainly become more detailed.

Next to the simplified asteroid model, there are two disturbing forces that are considered in the true state model: the third-body disturbance and the SRP. Beforehand, it was assumed that gravity gradient torque has a negligible influence on the propagation of the spacecraft orbit. However, it could be concluded from the magnitude of the aforementioned disturbance force accelerations that the magnitude for the gravity gradient torque is in the same range as was simulated by Razgus (2016). Trying to simulate an environment with with the magnitude of the SRP for disturbance models is therefore now incomplete. Therefore, for future simulation of true state results, gravity gradient torque should be included as well.

The influence of the SRP could not be measured by the IMU with the current noise level. Additionally, it was found that the values are smaller compared to the gravitational forces by the asteroid body and the Sun. This means that the effect of smaller asteroid bodies, such as for an orbit in the proximity of 101955 Bennu, poses a different influence by the smaller forces that are exerted on the spacecraft. Likewise, other forces such as those caused by firing thrusters have not been simulated yet. Hence, proximity operations for smaller asteroids or firing of the spacecraft thrusters are expected to notably change the true state.

8-4 Proximity Operations

The fact that the accuracy of the different orbits increases with decreasing the time step can be deduced from different RMSE results. However, the fact that the performance of the 35 and 50 km orbit with respect to each other is dependent on the time step, is something new. Since all the optional tuning parameters of the KF were not adjusted for running the other orbits, it can be argued that the initial tuning had a certain influence on the performance per orbital height. It could very well be that the chosen tuning parameters described in Table 7-1 perform better for the 35 km orbit for higher time step intervals.

Furthermore, for different orbits, the worst accuracy is obtained for the orbit farthest from the target asteroid. This opposes the findings of Spee (2022), where the orbit farthest from the asteroid had the highest accuracy in position estimation. Although it is argued that the offset of the state estimates has been adjusted accordingly with the orbital height, it is not clear whether the other tuning parameters of the KF were adjusted for the different scenarios. The different findings by Spee (2022), as well as the different performance of the 50 and 35 km orbit with respect to the other, are thought to be caused by the tuning of the filter. In case that Spee (2022) tuned additional parameters of the KF for different orbital heights, the resulting filters could be too different from those used in this research to make a proper comparison.

The type of filter (autonomous or not) also plays a role in the autonomy of the navigation filter. In order to obtain a navigation filter that works well for different orbital heights, a trade-off between the tuning parameters can be made.

8-5 Navigation Time step

It was previously recommended by Spee (2022) to investigate the effect of simulation time step on the performance of the filter. When comparing the results of Bourgeaux (2020) and Spee (2022), the accuracy is considered similar or better respectively when my own navigation filter is simulated using a smaller time step. We can assume that the filter can perform with a similar accuracy as with detailed gravity field approximations when a time step of either 0.1 or 0.01 seconds is used. Being able to provide estimates with the same accuracy but for more uncertainties is beneficial for space navigation. Demonstrating that it is possible to handle unpredictable accelerations can increase the mission safety. However, the question remains how the navigation filter would perform if both a smaller time step, as well as a more detailed approximation of the gravity field would be implemented in the navigation filter.

According to Sheikh et al. (2009), using the DSN it was possible to accurately estimate position of a spacecraft with an error of 0.3 km at a distance of 1 AU from Earth. It can be safely said that for the benchmark scenario, this accuracy is obtained for all time steps of the navigation filter. Still, it was clear from the results Section 7-3 that the time step of 0.1 s and 0.01 s have the best performance in terms of accuracy. If that is compared to the computational effort as presented in Table 7-3, a mere 0.06 m improvement on the accuracy requires 24 times more computational time. It is therefore concluded that a time step of 0.1s is the best trade-off between accuracy and computational time.

The best performing simulation time step imposes some conclusions for the hardware design of the spacecraft as well. First, an example can be taken from the flight computer that was on the NEAR-Shoemaker spacecraft. As described by Lee and Santo (1996), 'the flight computer is used to perform the computationally intensive processing. Once each second, the outputs of the attitude sensor suite are processed to provide a filtered estimate of the S/C state (attitude and body rates)'. The processing for the spacecraft attitude was thus performed once every second. Considering the technology for computer hardware has considerably improved since the launch of the NEAR-shoemaker, it can be assumed that an time step of 0.1 s should be no problem for a modern flight computer.

Chapter 9

Conclusions and Recommendations

In Chapter 8, a discussion was presented based on the results in Chapter 7. From the discussion and the results, conclusions are drawn, which are presented in Section 9-1. The main research question as well as the sub-questions as introduced in Section 1-2, will be answered. Furthermore, recommendations can be derived from the discussion as well, which are given in Section 9-2.

9-1 Conclusions

Before addressing the conclusions of the main research question, the final answers to sub-questions are given. To start with, the first sub-questions were

- What sensor set is necessary to estimate position and orientation of the spacecraft?
- How can the selected sensors be configured and simulated in the navigation system?

In order to estimate both the position and orientation of the spacecraft, the chosen sensor set of a star tracker, IMU and LiDAR sensor suffices. The accelerometer of the IMU is necessary for measuring any non-gravitational accelerations, and the gyroscope measurements are needed to approximate the orientation changes of the spacecraft. To be able account for initial offsets of the position, velocity or attitude, a measurement update is needed.

The sensors were fused within an EKF. Each sensor measurement was simulated with their respective output rate that was found in literature. The measurements of the IMU were introduced as noisy control inputs in the time update of the navigation filter. For the star tracker and the LiDAR, they each had their own measurement update. The star tracker measurement update is necessary to account for offsets of the orientation estimation, as well as process errors for the orientation computation in the time update. The LiDAR measurement update is necessary to account for the offset in either position or velocity estimation, as well as for errors in their computation. Although it was proven that the system was coupled between

the position and orientation states of the filter, the covariance was negligible, and the system behaved in general as an uncoupled system.

Each sensor was simulated with its own error characteristic. Although the error values were corresponding to values found in literature, the models could be more accurate. The effect of a temporary sensor loss for the star tracker as well as the LiDAR was also analysed. This concluded that for convergence of the navigation filter, the star tracker and the LiDAR are necessary to have convergence for the attitude and position estimation respectively. If either one of the two sensor measurements temporarily suffered from loss, the time update was able to propagate the states accurate enough for up to 2000 s for the navigation filter to regain the nominal errors after the sensor were recovered.

Next, we had

- To what extent can the navigation filter improve the accuracy of the state estimation?

The position can be estimated with an RMSE of 0.5 m for a time step of either 0.1 or 0.01 s for navigation of the benchmark scenario. This outperforms the current accuracy of estimation through the DSN. The navigation filter can obtain similar results for the simulation of scenarios with a different orbital height. Overall, an RMSE no higher than 1.5 m can be found for orbital heights between 35 km and 100 km.

Furthermore, one of the sub-questions was

- What is the role of the estimation frequency in the accuracy performance of the navigation filter?

From the results it was derived that using either a time step of 0.1 or 0.01 s for the update rate of the navigation filter gives the most accurate results, with an error of 1.5 m for the given orbital height range. It was also concluded that updating the navigation filter with 0.01 s time step instead of the 0.1 s time step requires 24 times more computational time. As the little improvement of the state estimation does not weigh against the much larger computational time, a time step of 0.1 s is recommended for implementing the navigation filter in a GNC.

Finally, the last sub-question was

- To what extent can the autonomous navigation system improve the response time when orbital correction manoeuvres are required?

It is concluded that the response time is improved as well, as the navigation filter converges for the position within five minutes. This would mean that after five minutes, a control input can be given to the GNC to adjust the orbit or attitude of the spacecraft. This is four times faster than sending a command through the DSN which can only be executed by the spacecraft 20 minutes later.

Having summarised an answer for all sub-questions, the conclusion on the main research question can be given.

"How can sensor fusion applied in autonomous navigation for deep space spacecraft contribute to improving safety and accuracy during proximity operations?"

It has been demonstrated that a sensor fusion model of a star tracker, IMU and a LiDAR sensor can estimate the position and attitude of a spacecraft in proximity operations around 433 Eros with an accuracy of 0.5 m RMSE for the estimated position and $3{\cdot}10^{-3}$ RMSE for the attitude of the spacecraft relative to the asteroid.

For a trade-off between accuracy and computational effort, it is concluded that a time step of 0.1 seconds for the navigation filter is the best option. Increasing the time step decreases the accuracy significantly for different scenarios. Decreasing the time step significantly increases the computational effort and does not improve the accuracy.

With a time step of 0.1 s, an accuracy of 1.5 m can be obtained for the position for orbital heights ranging from 35 to 100 km for the proximity operation. Regarding safety, it is concluded that the navigation system can converge within five minutes for the position estimation and should be able to exert control commands faster than through DSN communication. Furthermore, the navigation system handle sensor loss of at least half an hour for either the star tracker or the LiDAR sensor.

The implemented model is a step in the right direction, but we are not there yet. More measurement errors, disturbance forces, and the implementation of the control demands can provide more insight into the future of autonomous GNC for deep space asteroid missions. Still, having a navigation filter with the described characteristics, it is possible to estimate the position and orientation in a timely frame with enough accuracy that it should be possible to design autonomous navigation system for a spacecraft in proximity operation around an asteroid.

9-2 Recommendations

In this section, recommendations on future research are given. The recommendations are based on the constraints and assumptions that have been made throughout the research. They have been categorised into three main parts: the true state simulation, the sensor measurement simulation and the GNC system.

9-2-1 True State Simulation

In addition to the true state simulation as described in Section 3-4, it is recommended to

- simulate the true state simulation for different time steps to investigate the effect of the time step on the simulation accuracy;
- introduce the gravity gradient torque in the true state simulation model to have a more complete model of the disturbance forces;
- simulate the proximity operations around 433 Eros for a heterogeneous density model for the detailed polyhedron surface model to have a more realistic model of the gravitational force exerted by the asteroid;

- simulate the proximity operations for different target asteroids to investigate the robustness of the navigation filter;
- simulate star orientation around the spacecraft for star tracker measurements in order to be able to design a more detailed model of the star tracker measurement simulation.

9-2-2 Sensor Measurement Simulation

For the sensors, the measurement simulation was presented in Section 5-2, Section 5-3, and Section 5-4. For the sensor measurement simulations, additional research options are listed below.

- Introduce a star tracker measurement model that can simulate the pre-processing algorithm of a star tracker. This allows to investigate whether a navigation filter can be designed that is more tightly coupled.
- Introduce an IMU measurement model with more detailed error characteristics, and consider the mounting of the sensors on the spacecraft and simulate the misalignment errors. This makes the measurement simulation more realistic.
- As mentioned in Section 5-2, there are usually multiple IMUs integrated into the navigation architecture of spacecraft. By extending the model to have more sensors of the same type, the fusion could have been more realistically demonstrated. In this case, the configuration of the sensors onto the spacecraft body need to be determined first, as these indicate how the reference frames of the sensors are placed with respect to the main spacecraft body. If multiple IMU sensors and their placement are assumed, it would have made more sense to also incorporate scaling and misalignment errors in the measurement simulations.
- It is now demonstrated that measurements from a magnetic field are not necessary to obtain estimations of the position and attitude of the spacecraft. On the other hand, it could be tested whether the navigation filter would benefit from magnetometer measurements for a target asteroid with a magnetic field. In addition, this poses the question whether the absence or presence of a magnetic field can be autonomously detected and determined by a navigation filter;
- By incorporating landmark tracking algorithms, a SLAM algorithm can be developed to generate a landmark field in-orbit. This gives the opportunity to simulate the LiDAR measurements with more detail.

9-2-3 Guidance Navigation & Control

In Chapter 5 and Chapter 6, the state space design and the navigation filter design are presented, respectively. For the further design of the GNC of the spacecraft, it is recommended to

- run the navigation filter with a time step of 0.1 s. This time step is the best trade-off between computational effort and estimation accuracy;

- extend the GNC with a SLAM algorithm to map the surface and gravity field of a target asteroid;
- add error states to the state space system of the navigation filter. By estimating the error for measurements, the navigation filter can improve;
- introduce control forces exerted on the spacecraft. The coupling of the attitude to the position and velocity states is considered negligible. For the coupling to be more significant, larger non-gravitational accelerations should be present in the true state simulation;
- investigate orbit stability using control forces and a target trajectory. Here, the controllability of the GNC can be tested.

Appendix A

Spacecraft Design Requirements Overview

Here, an overview is given of all the requirements set throughout the literature study. They appear in the same order as in the chapters.

A-1 Mission Requirements

- R-MIS-010 The mission shall demonstrate feasibility of sensor fusion for autonomous navigation of the vehicle during asteroid observation.
- R-MIS-020 The navigation system shall be able to perform orbital corrections without the aid of ground stations or other network communication.
- R-MIS-030 The mission environment for autonomous navigation has an orbital radius of 50 km, around planetoid 433 Eros.

A-2 Navigation System Requirements

- R-NAV-SYS-01 The navigation system and payload bus are connected such that the data output of the payload is directly transmitted to the navigation system.
- R-NAV-SYS-02 The navigation system shall be able to estimate both the attitude and relative positioning of the spacecraft during the proximity operations.
- R-NAV-SYS-03 The navigation system shall be able to autonomously stabilise an orbit during proximity operations.
- R-NAV-SYS-04 The navigation system shall be able to perform stability corrections at least once per orbit around 433 Eros.

- R-NAV-SYS-05 The navigation system shall have a system response shorter than 20 minutes.
- R-NAV-SYS-06 The navigation system computer shall perform sensor fusion algorithms between the navigation sensor outputs.
- R-NAV-SYS-07 During orbital observation around 433 Eros, continuous observations shall be carried out by the navigation sensors.
- R-NAV-SYS-08 The navigation sensors shall include redundancy at least per sensor type.

A-3 Dynamics Estimation Requirements

- R-DYN-010 The forces exerted on 433 Eros by the Sun are neglected.
- R-DYN-020 The gravity model of 433 Eros will be approximated using spherical harmonic expansions.
- R-DYN-030 A constant rotational rate of for 433 Eros is assumed at 1639.38922 degrees per (Earth) day.
- R-DYN-040 The forces considered in the dynamic model of the spacecraft are either gravitational or caused by solar radiation pressure.
- R-DYN-050 The forces exerted by the Sun on the spacecraft body are assumed to be only due to the solar radiation pressure.
- R-DYN-060 The main reference frame considered is a rotating asteroid-fixed reference frame.
- R-DYN-070 The secondary reference frame considered is the spacecraft reference frame.
- R-DYN-071 The z-axis of the spacecraft reference frame is in line with the navigation camera.
- R-DYN-072 The navigation camera should be continuously pointed towards the asteroid during observation.

A-4 Sensor Selection Requirements

- R-NAV-SENS-01 The navigation system shall be equipped with a three-axis star tracker.
- R-NAV-SENS-02 The navigation system shall be equipped with a light detection and ranging (LiDAR) sensor.
- R-NAV-SENS-03 The system shall be equipped with a four-axis inertial measurement unit (IMU).
- R-NAV-SENS-04 The IMU consists of a gyroscope and an accelerometer.

- R-NAV-SYS-05 The navigation system shall be able to point the ranging sensor towards the asteroid during orbit.

Appendix B

Kepler Coordinate Equations

In this chapter, the equations describing various relations between the orbital elements of a Kepler orbit are given, as well as the conversion between the Keplerian and Cartesian coordinate systems.

B-1 Orbit parameter relations

$$r = \frac{a(1-e^2)}{1+e\cos\theta} = \frac{p}{1+e\cos\theta} \tag{B-1}$$

$$r_p = a(1-e) \tag{B-2}$$

$$r_a = a(1+e) \tag{B-3}$$

$$E_{tot} = E_{kin} + E_{pot} = \frac{V^2}{2} - \frac{\mu}{r} = -\frac{\mu}{2a} \tag{B-4}$$

$$V^2 = \mu(\frac{2}{r} - \frac{1}{a}) \tag{B-5}$$

$$V_{circ} = \sqrt{\frac{\mu}{r}} = \sqrt{\frac{\mu}{a}} \tag{B-6}$$

$$V_{esc} = \sqrt{\frac{2\mu}{r}} \tag{B-7}$$

$$T = 2\pi\sqrt{\frac{a^3}{\mu}} \tag{B-8}$$

$$\tan\frac{\theta}{2} = \sqrt{\frac{1+e}{1-e}}\tan\frac{E}{2} \tag{B-9}$$

$$M = E - e\sin E \tag{B-10}$$

$$M = M_0 + n(t-t_0) \tag{B-11}$$

$$n = \sqrt{\frac{\mu}{a^3}} \tag{B-12}$$

$$E_{i+1} = E_i + m\frac{M - E_i + e\sin E_i}{1 - e\cos E_i} \tag{B-13}$$

$$r = a(1 - e\cos E) \tag{B-14}$$

$$\begin{aligned} \tan\frac{\theta}{2} &= \sqrt{\frac{e+1}{e-1}}\tanh\frac{F}{2} \\ M &= e\sinh F - F \\ M &= n\,(t - t_0) \\ n &= \sqrt{\frac{\mu}{(-a)^3}} \\ r &= a(1 - e\cosh F) \end{aligned} \tag{B-15}$$

B-2 Kepler to Cartesian Conversion

$$\begin{pmatrix} \xi \\ \eta \end{pmatrix} = \begin{pmatrix} r & \cos\theta \\ r & \sin\theta \end{pmatrix}; \quad \begin{pmatrix} x \\ y \\ z \end{pmatrix} = \begin{pmatrix} l_1 & l_2 \\ m_1 & m_2 \\ m_1 & n_2 \end{pmatrix} \begin{pmatrix} \xi \\ \eta \end{pmatrix} \tag{B-16}$$

where

$$\begin{aligned} l_1 &= \cos\Omega\cos\omega - \sin\Omega\sin\omega\cos i \\ l_2 &= -\cos\Omega\sin\omega - \sin\Omega\cos\omega\cos i \\ m_1 &= \sin\Omega\cos\omega + \cos\Omega\sin\omega\cos i \\ m_2 &= -\sin\Omega\sin\omega + \cos\Omega\cos\omega\cos i \\ n_1 &= \sin\omega\sin i \\ n_2 &= \cos\omega\sin i \end{aligned} \tag{B-17}$$

$$\begin{aligned} H &= \sqrt{\mu a\,(1 - e^2)} \\ \dot{x} &= \frac{\mu}{H}\left[-l_1\sin\theta + l_2(e + \cos\theta)\right] \\ \dot{y} &= \frac{\mu}{H}\left[-m_1\sin\theta + m_2(e + \cos\theta)\right] \\ \dot{z} &= \frac{\mu}{H}\left[-n_1\sin\theta + n_2(e + \cos\theta)\right] \end{aligned} \tag{B-18}$$

B-3 Cartesian to Kepler conversion

$$
\begin{aligned}
&r = \|\mathbf{r}\|; \quad V = \|\mathbf{V}\|; \quad \mathbf{h} = \mathbf{r} \times \mathbf{V}; \quad \mathbf{N} = \begin{pmatrix} 0 \\ 0 \\ 1 \end{pmatrix} \times \mathbf{h} \\
&a = 1/\left(\tfrac{2}{r} - \tfrac{V^2}{\mu}\right) \\
&\mathbf{e} = \tfrac{\mathbf{V}\times\mathbf{h}}{\mu} - \tfrac{\mathbf{r}}{r}; \quad e = \|\mathrm{e}\| \\
&i = \operatorname{acos}\left(\tfrac{h_Z}{\|\mathbf{h}\|}\right) \\
&N_{xy} = \sqrt{N_x^2 + N_y^2}; \quad \Omega = \operatorname{atan}2\left(\tfrac{N_y}{N_{xy}}, \tfrac{N_x}{N_{xy}}\right) \\
&\omega = \operatorname{sign} * \operatorname{acos}(\hat{\mathbf{e}} \cdot \hat{\mathbf{N}}) \quad (\operatorname{sign} = +1 \text{ if } (\hat{\mathbf{N}} \times \mathbf{e}) \cdot \mathbf{h} > 0; \quad -1 \text{ otherwise }) \\
&\theta = \operatorname{sign} * \operatorname{acos}(\hat{\mathbf{r}} \cdot \hat{\mathbf{e}}) \quad (\operatorname{sig} n = +1 \text{ if } (\mathbf{e} \times \mathbf{r}) \cdot \mathbf{h} > 0; \quad -1 \text{ otherwise })
\end{aligned}
\tag{B-19}
$$

Appendix C

Benchmark Simulation Verification

Complementary to the visualisation of the benchmark scenario, the position and velocity propagation of the trajectory have been plotted in Figure C-1.

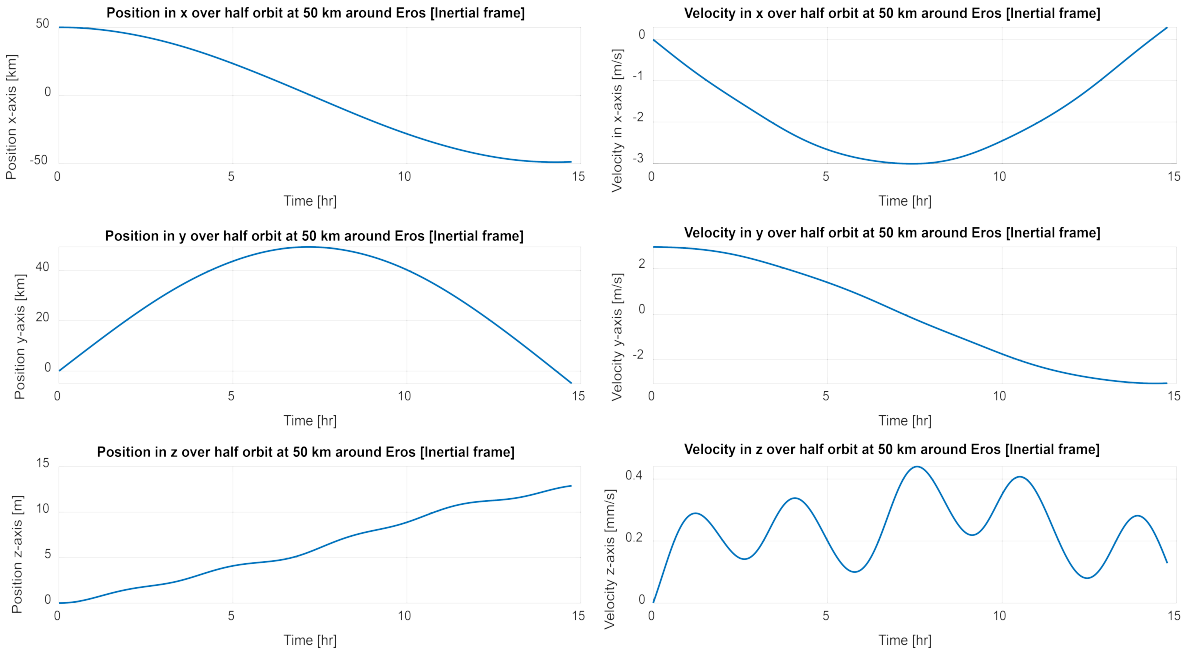

Figure C-1: Position and velocity propagation of the benchmark scenario in the inertial frame.

The results are visible in Figure C-2 and Figure C-3. Here, the propagation as well as the error between the two models are plotted for the three smallest time steps.

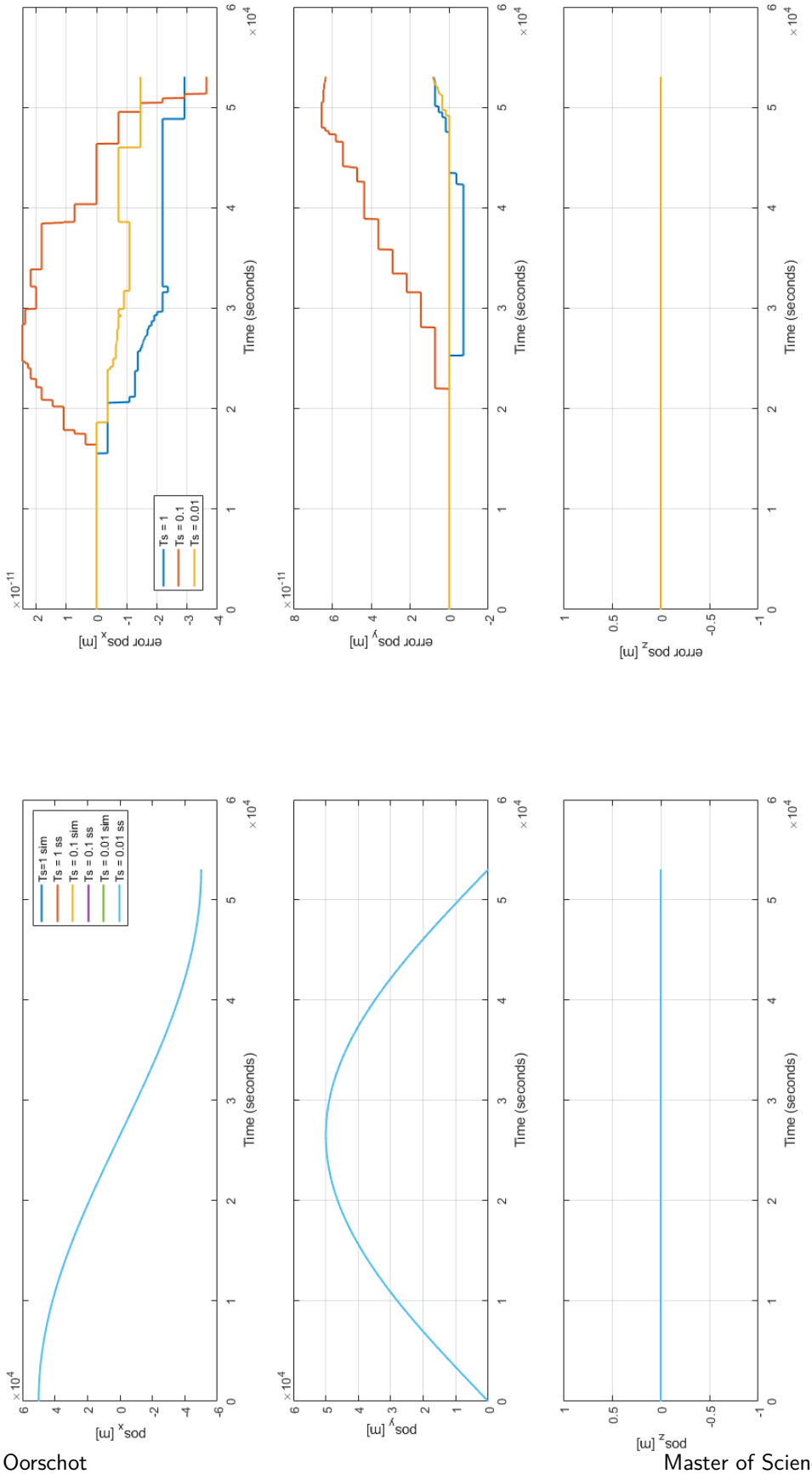

Figure C-2: Propagation of position and error between true state simulation and state space update with point mass asteroid models for time steps 1s, 0.1s, 0.01 in the inertial frame.

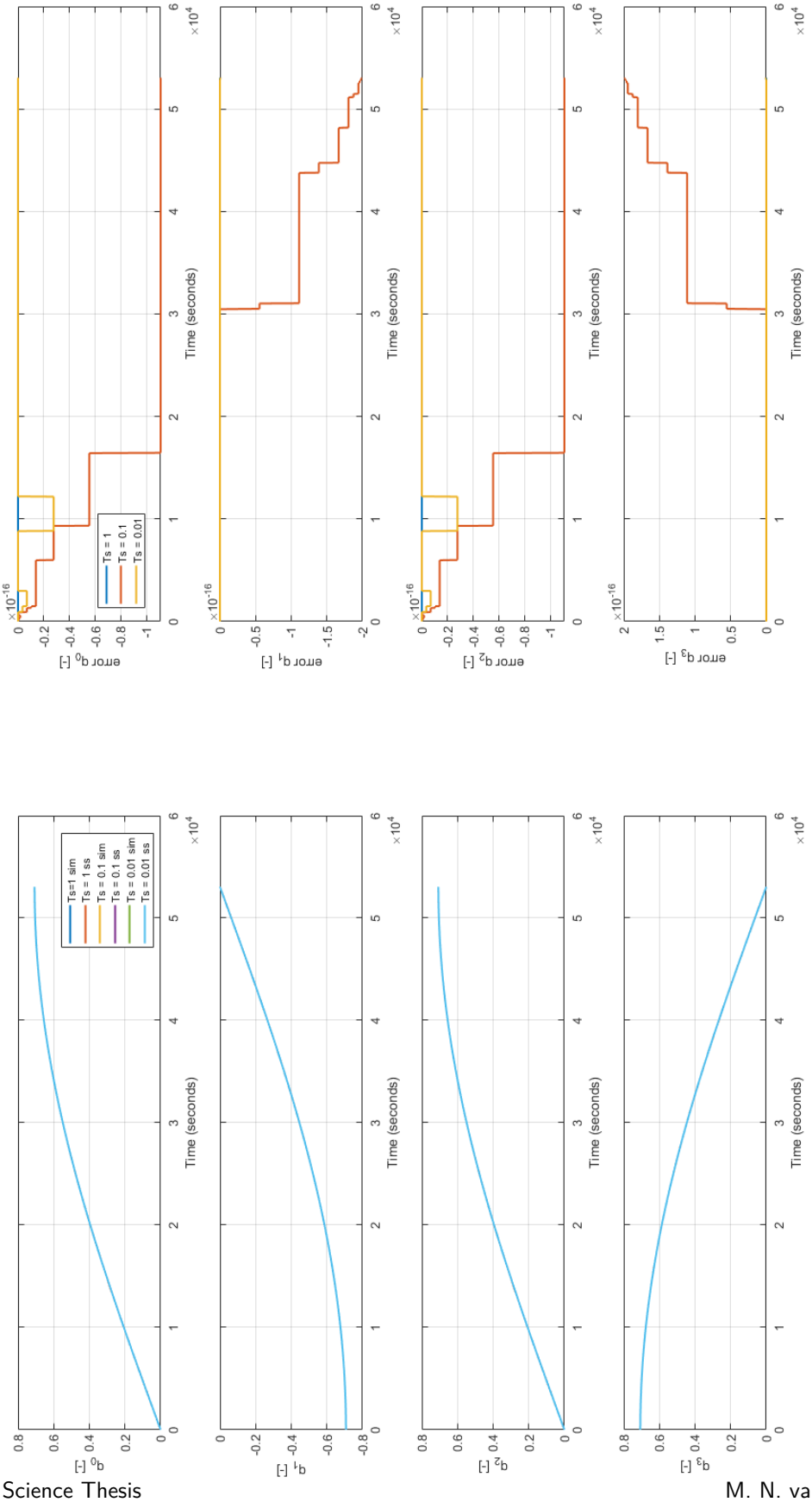

Figure C-3: Propagation of quaternion and error between true state simulation and state space update with point mass asteroid models for time steps 1s, 0.1s, 0.01 in the inertial frame.

The position with respect to the asteroid reference frame in all axis directions has been plotted in Figure C-4, and the angular rate of the spacecraft reference frame with respect to the inertial reference frame has been plotted in Figure C-5.

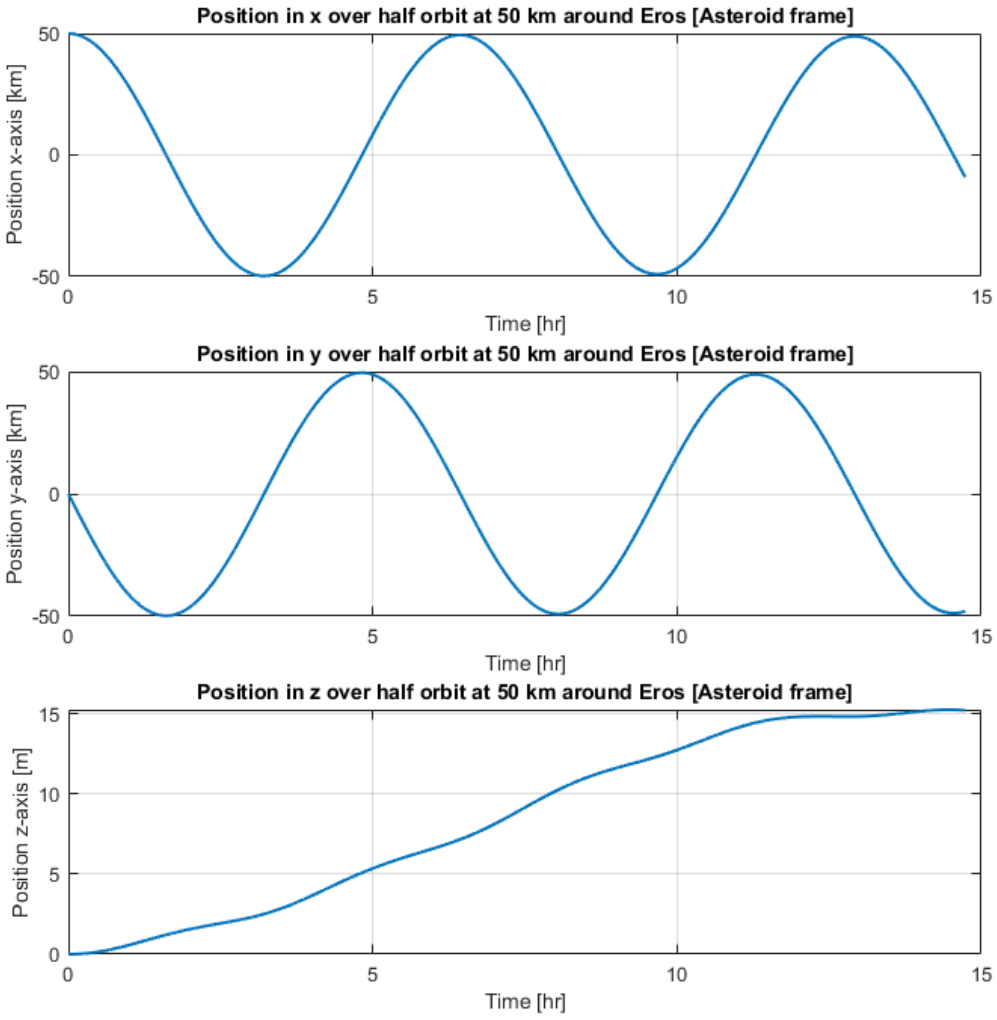

Figure C-4: Position for half orbit at 50 km around Erosfor the asteroid reference frame.

For the polyhedron verification , the additional figures for the propagation of the true state simulation position and attitude are presented in Figure C-6 and Figure C-7.

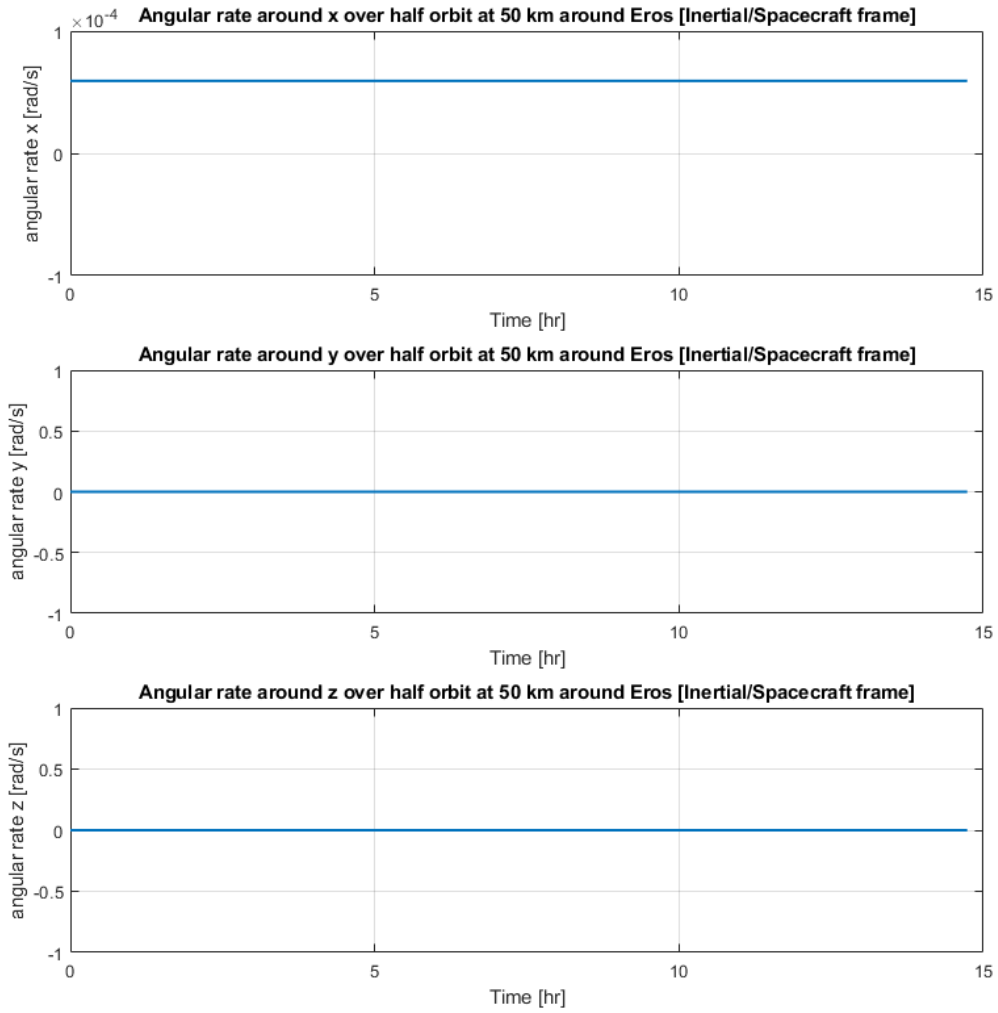

Figure C-5: Angular rates of spacecraft reference frame around inertial reference frame for simulation of half orbit around Eros at 50km.

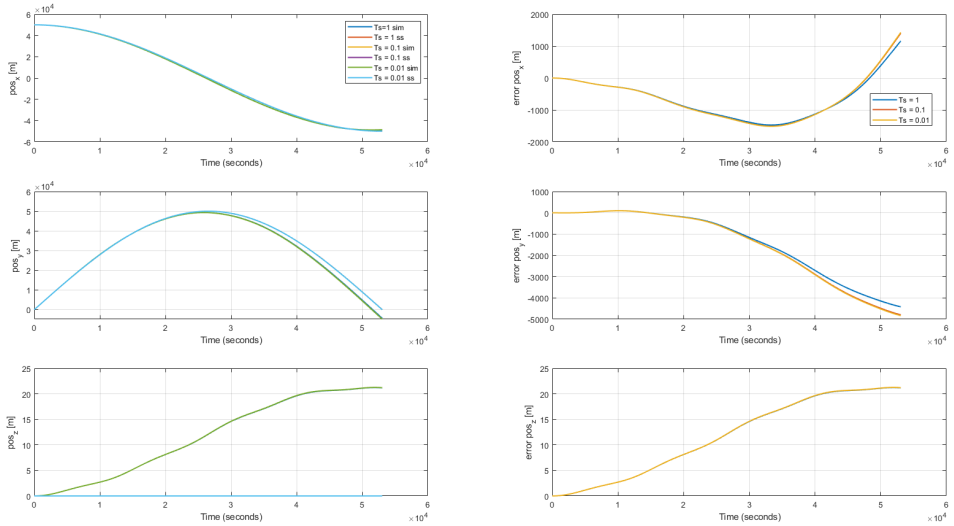

Figure C-6: Propagation of position and error between true state simulation with polyhedron model and state space update for time steps 1s, 0.1s, 0.01 in the inertial frame.

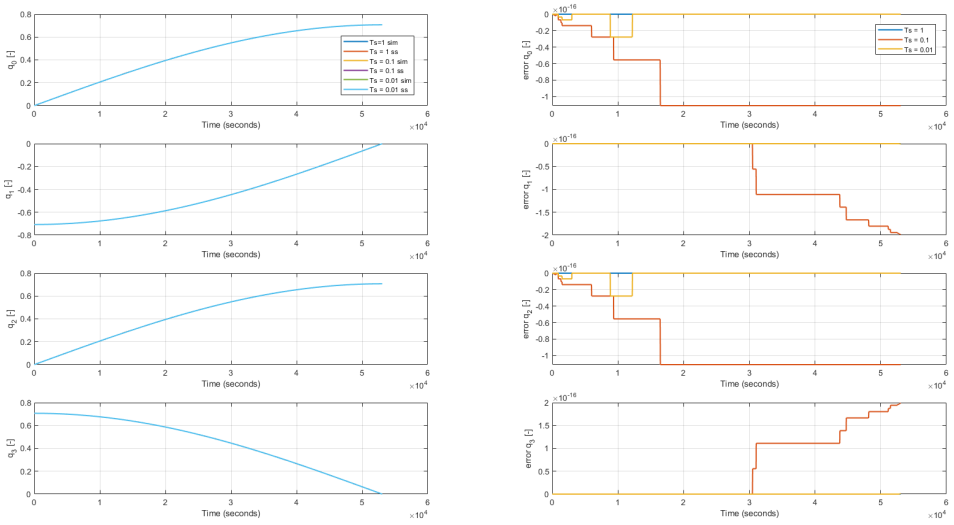

Figure C-7: Propagation of quaternion and error between true state simulation with polyhedron model and state space update for time steps 1s, 0.1s, 0.01 in the inertial frame.

Appendix D

Sensor Set Implementation

In addition to the position and quaternion results, the propagation of the velocity for star tracker implementation has been plotted in Figure D-1. Similar to the position estimation, the star tracker measurement is not able to ensure convergence for the velocity estimation.

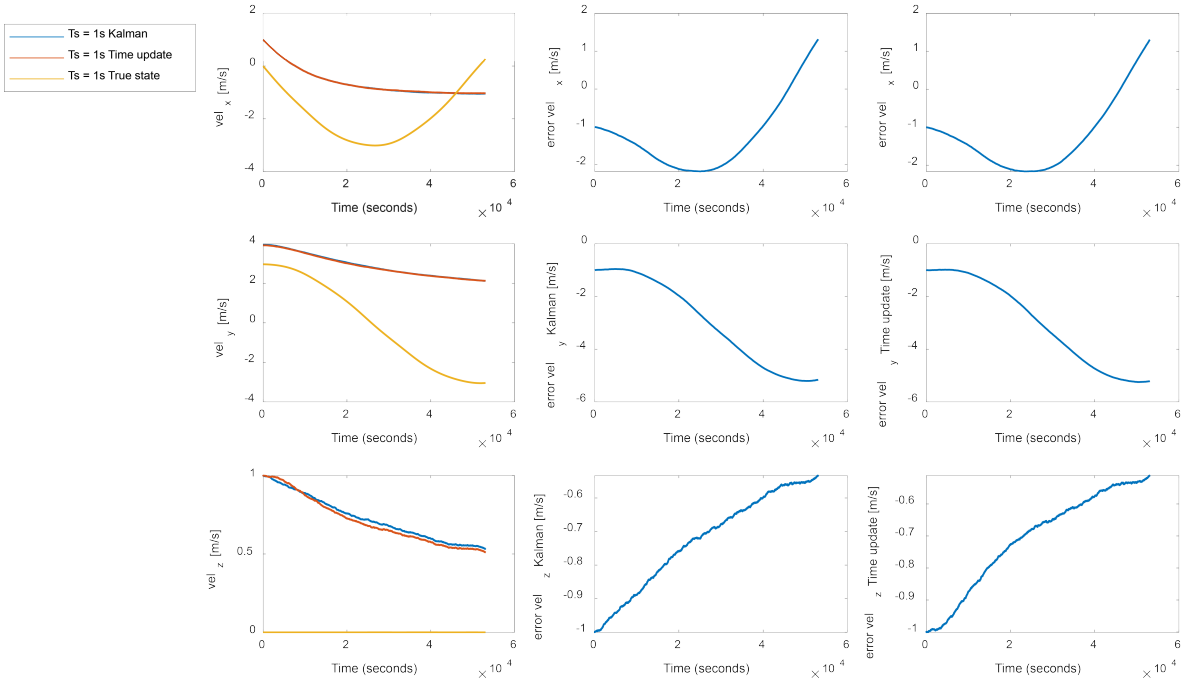

Figure D-1: Velocity propagation for star tracker measurement only, time step of 1s.

In Figure D-2, the velocity has been plotted for the implementation of the LiDAR sensor into the navigation filter. Similar to the result of the position estimation, it is seen that the sensor implementation improves the estimation of the velocity estimation compared to the time update.

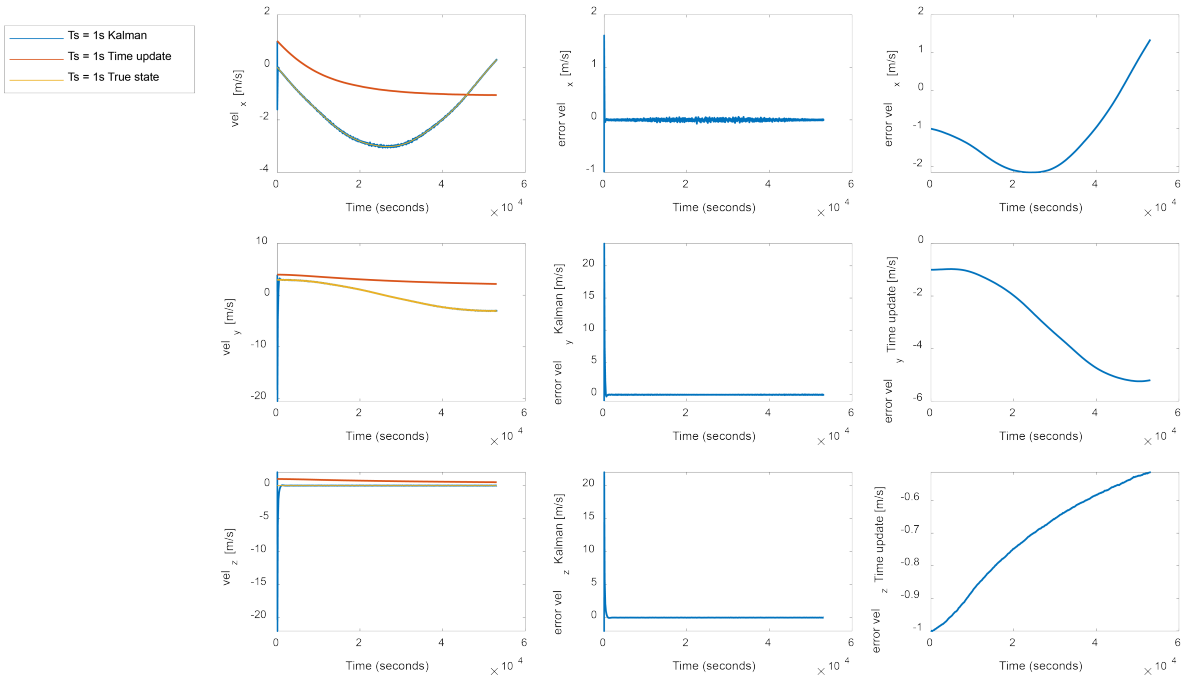

Figure D-2: Velocity propagation for LiDAR measurement only, time step of 1s.

The sensor implementation results have also been presented for the implementation of both sensors to the system. These the results of the filter with and without both measurement updates are presented here. Where the implementation of the separate measurement updates was done for a time step of 0.1 s, the complete navigation filter has also been verified for the benchmark setting of 0.01s time step. Visible in Figure D-3, Figure D-4, and Figure D-5, the propagation results of the position, velocity, and quaternion respectively are plotted.

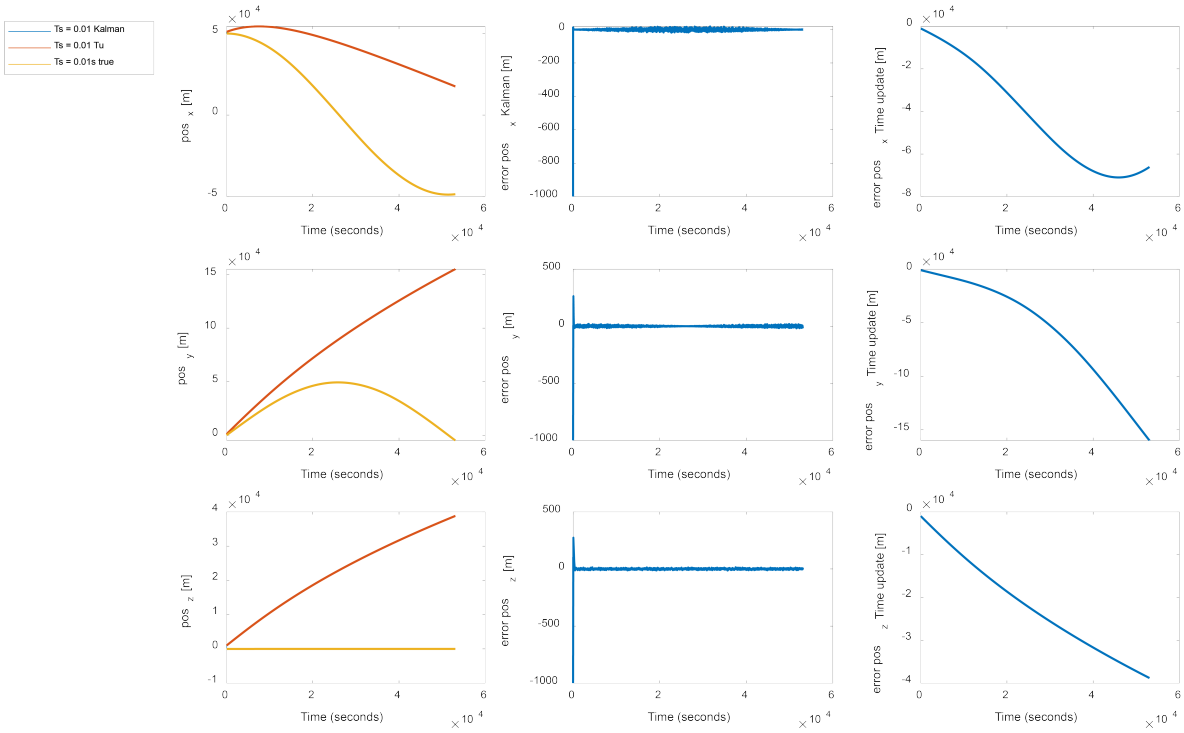

Figure D-3: Spacecraft position propagation and errors of the EKF and the time update of the EKF for 0.01 s timestep

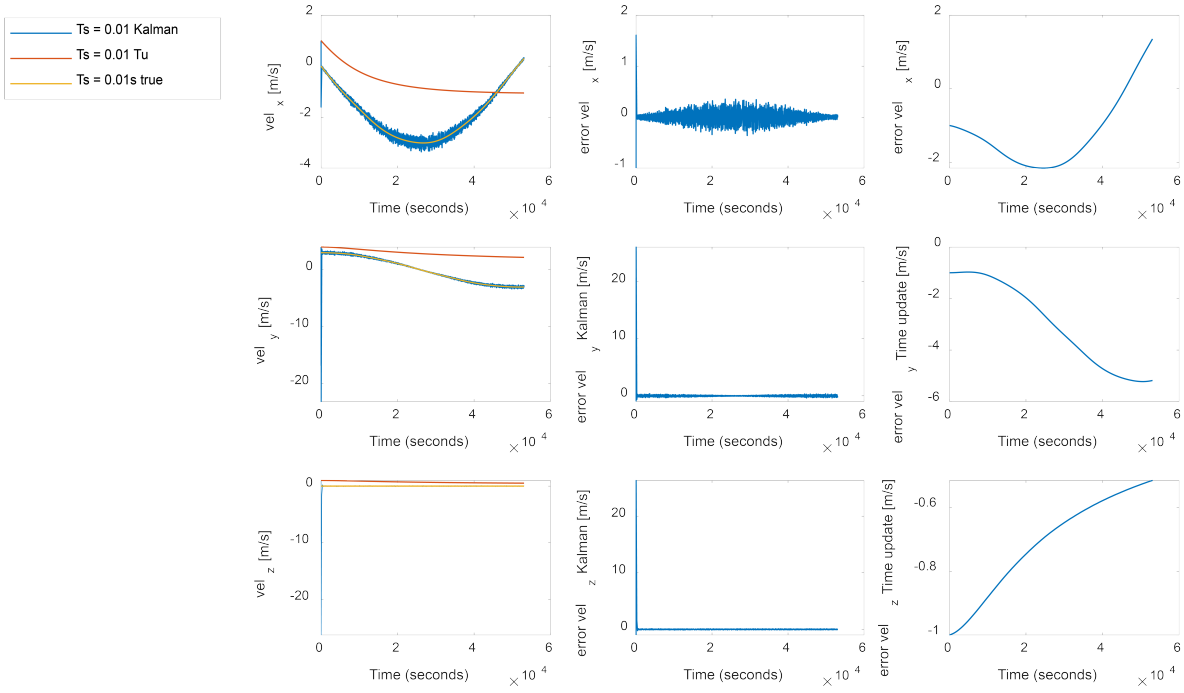

Figure D-4: Spacecraft velocity propagation and errors of the EKF and the time update of the EKF for 0.01 s timestep

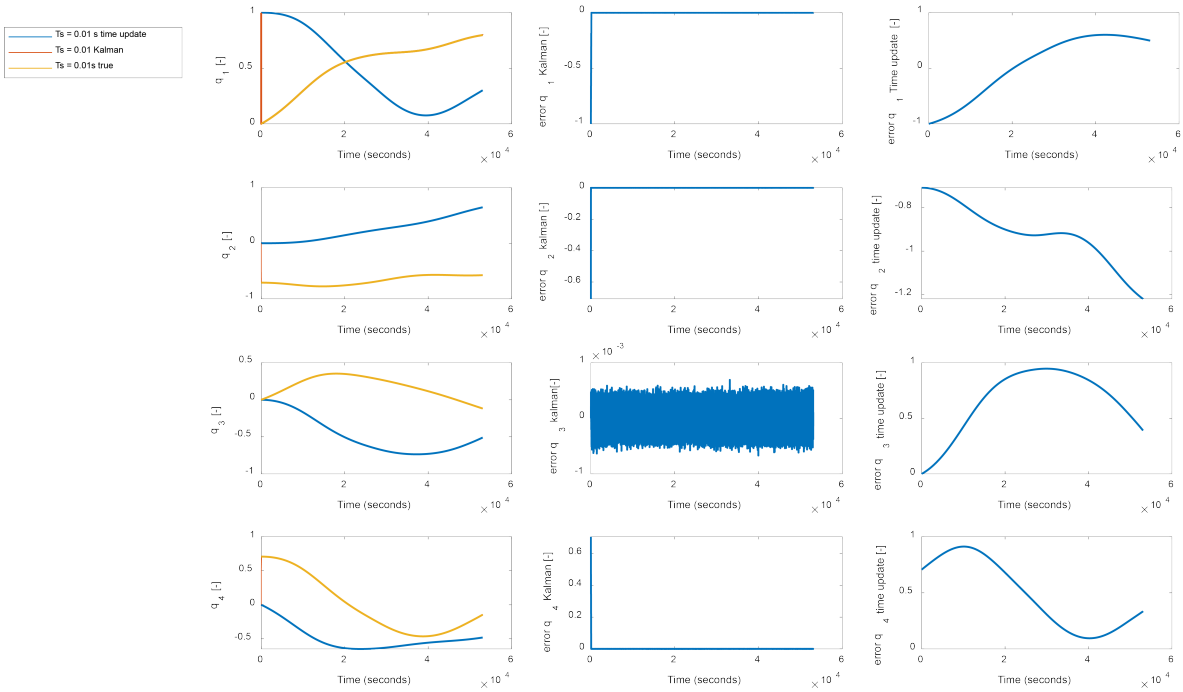

Figure D-5: Spacecraft attitude propagation and errors of the EKF and the time update of the EKF for 0.01 s timestep

Appendix E

Covariance Results

In Figure E-1, the average covariance of the navigation filter over the simulation time is presented.

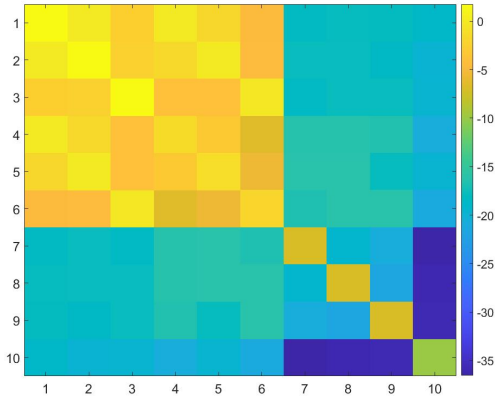

Figure E-1: Average of log function of covariance matrix P for 0.01s timestep.

In the figure, the numbers correspond to the rows and columns of the covariance matrix. Therefore, the order of the states is considered as: position (1-3) , velocity (4-6), quaternion error (7-9) and gravitational constant (10). Based on Figure E-1, it can be seen that the diagonal values are largest for the position, velocity and quaternion errors. Furthermore, the covariance between the position and velocity, have relatively higher values as well.

For checking the behaviour of the covariance for the position estimation, the orbit of the benchmark scenario has been adjusted. First, the orbit is now starting at $r_y = 50$ km, and simulated for the same time at a time step of 1 s. The results for the position is shown in Figure E-2.

Secondly, the orbit has been adjusted to have an inclination of 90 deg. The starting point is still the same as for the benchmark scenario. These results are shown in Figure E-3.

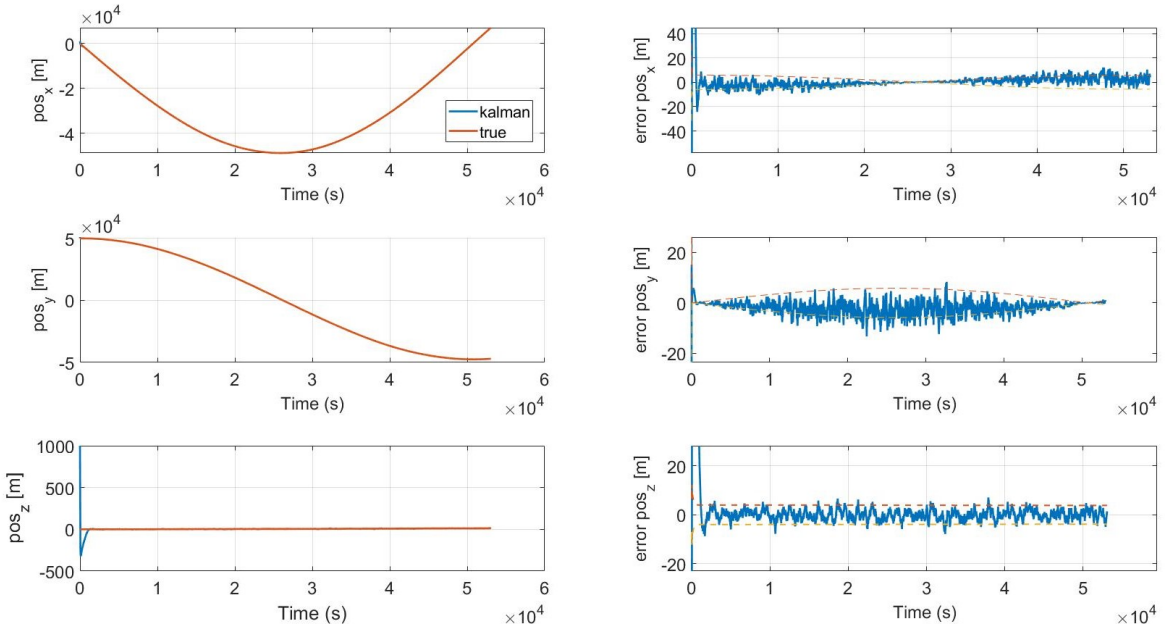

Figure E-2: Position propagation and position error, starting at r_y= 50 km, time step is 1s.

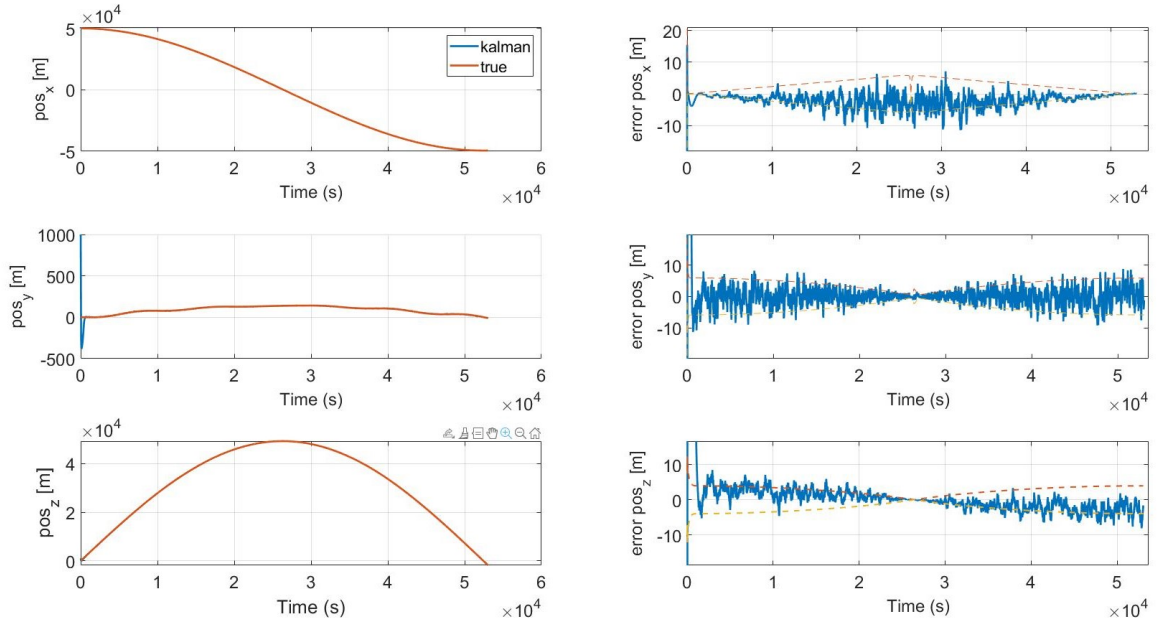

Figure E-3: Position propagation and position error, starting at i= 90 deg, time step is 1s. time step is 1s.

Appendix F

Velocity Estimation Results

For the propagation of the orbit for different orbital heights, the RMSE values of the velocity and quaternion results are shown in Figure F-1

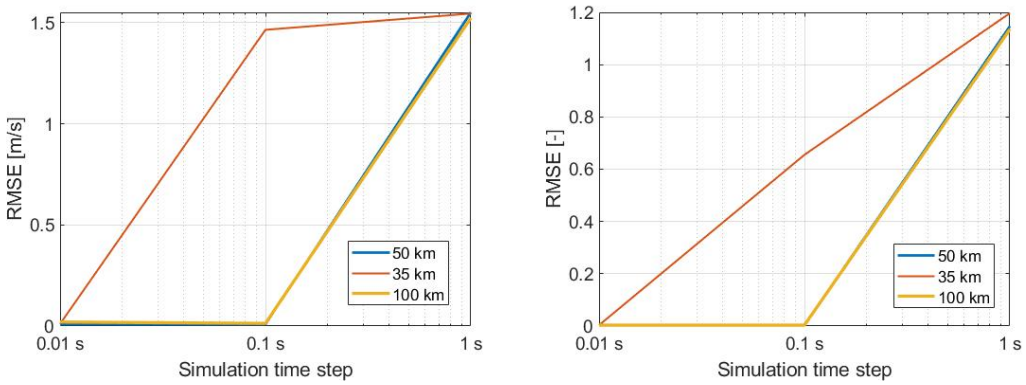

(a) RMSE for velocity propagation.

(b) Time steps 0.01, 0.1, and 1 s.

Figure F-1: RMSE over propagation for different computation time steps, for an orbit of 35, 50 and 100 km.

For the sensor loss scenario described in Section 7-2, the propagation of the velocity and the error between the true and estimated state is shown in Figure F-2.

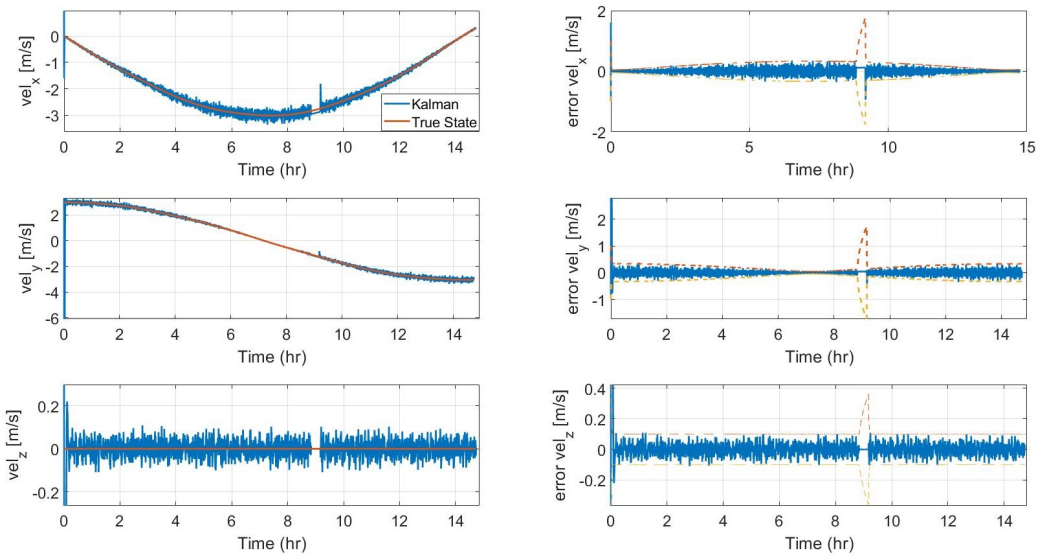

Figure F-2: True and estimated velocity propagation with sensor loss, for time step = 0.01s, inertial frame.

Bibliography

Ballester, M. T. (2018). Asteroid mission guidance and control using dual quaternions. *TU Delft Msc Thesis, TU Delft Repository, Netherlands.*

Bavel, H. (2022). Development of a 2d lidar slam algorithm for localization on the building construction site. *TU Delft Msc Thesis, TU Delft Repository, Netherlands.*

Bourgeaux, A. (2020). Autonomous estimation of the gravity field for asteroid missions. *TU Delft Msc Thesis, TU Delft Repository, Netherlands.*

Britt, D. T., Guy Consolmagno, S. J., and Lebofsky, L. (2014). Chapter 26 - main-belt asteroids. In Spohn, T., Breuer, D., and Johnson, T. V., editors, *Encyclopedia of the Solar System (Third Edition)*, pages 583–601. Elsevier, Boston, third edition edition.

Buemi, M., Landi, A., and Procopio, D. (1999). Autonomous star tracker for rosetta. *4th International ESA Conference on Guidance, Navigation and Control Systems, ESTEC, Noordwijk, The Netherlands.*

Chan, D. M. and Agha-mohammadi, A. (2019). Autonomous imaging and mapping of small bodies using deep reinforcement learning. *2019 IEEE Aerospace Conference*, pages 1–12.

Chanut, T. G. G., Winter, O. C., and Tsuchida, M. (2014). 3d stability orbits close to 433 eros using an effective polyhedral model method. *Monthly Notices of the Royal Astronomical Society*, 438:2672–2682.

Cheng, A. (2002). Near-earth asteroid rendezvous: Mission summary. *Asteroids III*, 1:351–366.

Christian, J. A. and Cryan, S. (2013). A survey of lidar technology and its use in spacecraft relative navigation. *AIAA Guidance, Navigation, and Control (GNC) Conference.*

Cioffi, G. and Scaramuzza, D. (2020). Tightly-coupled fusion of global positional measurements in optimization-based visual-inertial odometry. *CoRR*, abs/2003.04159.

Clerc, S., Martella, P., Durrant, D., Bertsch, N., and Dussy, S. (2009). Development of the european imu for space applications. *AIAA Guidance, Navigation, and Control Conference.*

Corporation, S. E. (2012). G362 high performance inertial measurement unit.

Daly, M. G., Barnouin, O. S., Dickinson, C., Seabrook, J., Johnson, C. L., Cunningham, G., Haltigin, T., Gaudreau, D., Brunet, C., Aslam, I., Taylor, A., Bierhaus, E. B., Boynton, W., Nolan, M., and Lauretta, D. S. (2017). The osiris-rex laser altimeter (ola) investigation and instrument. *Space Science Reviews*, 212:899–924.

Ding, W. and Gao, Y. (2020). A quaternion based error state kalman filter for attitude estimation using low-cost mems marg sensors. *2020 IEEE 92nd Vehicular Technology Conference (VTC2020-Fall)*, pages 1–5.

Dymock, R. (2010). *Asteroids and Dwarf Planets, and how to observe them*. Springer, New York.

Gaskell, R. (2008). Eros shape model v1.0. near-a-msi-5-erosshape-v1.0. *NASA Planetary Data System*.

Groÿekatthöfer, K. and Yoon, Z. (2012). Introduction into quaternions for spacecraft attitude representation. *Technical University of Berlin*.

Guha, S. (2015). *Computer Graphics Through Open GL: From Theory to Experiments*. CRC Press, Boca Raton.

Gustafsson, F. (2012). *Statistical Sensor Fusion*. Studentlitteratur AB, Lund.

Haberberger, S. J. (2016). An imu-based spacecraft navigation architecture using a robust multi-sensor fault detection scheme. *Curtis Laws Wilson Library Student theses*.

Harris, A. W., Drube, L., McFadden, L. A., and Binzel, R. P. (2014). Chapter 27 - near-earth objects. In Spohn, T., Breuer, D., and Johnson, T. V., editors, *Encyclopedia of the Solar System (Third Edition)*, pages 603–623. Elsevier, Boston, third edition edition.

Hashimoto, T., Kubota, T., Kawaguchi, J., Uo, M., Shirakawa, K., Kominato, T., and Morita, H. (2010). Vision-based guidance, navigation, and control of hayabusa spacecraft- lessons learned from real operation. *IFAC Proceedings Volumes*, 43, Issue 15:259–264.

Hemingway, E. G. and O'Reilly, O. M. (2018). Perspectives on euler angle singularities, gimbal lock, and the orthogonality of applied forces and applied moments. *Multibody System Dynamics*, 44:31–56.

Hesar, S. G., Scheeres, D. J., McMahon, J. W., and Takahash, Y. (2016). Surface proximity gravitational field analysis of the asteroid 433 eros. *The 39th Annual Guidance and Control Conference*.

Heyler, G. A. and Harch, A. P. (2002). Making near work: Cooperative modeling and simulation with an advanced guidance and control system. *Johns Hopkins APL Technical Digest*, 23 No. 1:46 – 57.

Ilci, V. and Toth, C. (2020). High definition 3d map creation using gnss/imu/lidar sensor integration to support autonomous vehicle navigation. *Sensors (Switzerland)*, 20.

Jean, I., Ng, A., and Misra, A. K. (2019). Impact of solar radiation pressure modeling on orbital dynamics in the vicinity of binary asteroids. *Acta Astronautica*, 165:167–183.

Jet Propulsion Laboratory (2011). Microsoft powerpoint lecture 10.1 dsn present and future.

Jet Propulsion Laboratory (2014). Nasa's mission operations and communications services. *NASA*.

Jet Propulsion Laboratory (2019). Jet propulsion laboratory 2019 strategic technologies.

Jonsson, A., Morris, R., and Pedersen, L. (2007). Autonomy in space exploration: Current capabilities and future challenges. *IEEE Aerospace Conference Proceedings*, pages 1–12.

Jung, S., Park, S. Y., Park, H. E., Park, C. D., Kim, S. W., and Jang, Y. S. (2012). Real-time determination of relative position between satellites using laser ranging. *Journal of Astronomy and Space Sciences*, 29:351–362.

Kok, M., Holy, J. D., and Schonz, T. B. (2017). Using inertial sensors for position and orientation estimation. *Foundations and Trends in Signal Processing*, 11:1–153.

Lam, Q. M. and Crassidis, J. L. (2007). Precision attitude determination using a multiple model adaptive estimation scheme. *IEEE Aerospace Conference Proceedings*.

Lee, S. C. and Santo, A. G. (1996). Near earth asteroid rendesvous (near) spacecraft safing design. *Elsevier Science Ltd*, 39:197–206.

Leeghim, H., Bang, H., and Park, J.-O. (2009). Singularity avoidance of control moment gyros by predicted singularity robustness: Ground experiment. *IEEE Transactions on Control Systems Technology*, 17(4):884 – 891.

Li, M. and Mourikis, A. I. (2012). Improving the accuracy of ekf-based visual-inertial odometry. In *2012 IEEE International Conference on Robotics and Automation*, pages 828–835.

Liebe, C. C. (1995). Star trackers for attitude determination. *IEEE Aerospace and Electronic Systems Magazine*, 10(06):10–16.

Lissauer, J. J. and de Pater, I. (2013). *Fundamental Planetary Science*. Cambridge University Press, New York.

Lyzhoft, J. and Wie, B. (2019). Ti - new image processing algorithm for terminal guidance of multiple kinetic-energy impactors for disrupting hazardous asteroids. *Astrodynamics*, 3:45–59.

Ma, W., Qiu, J., Liang, J., and Chen, B. (2019). Linear kalman filtering algorithm with noisy control input variable. *IEEE Transactions on Circuits and Systems II: Express Briefs*, 66:1282–1286.

Machuca, P. and Sánchez, J. P. (2021). Cubesat autonomous navigation and guidance for low-cost asteroid flyby missions. *Journal of Spacecraft and Rockets*, 58:1858–1875.

Madyastha, V. K., Ravindra, V. C., Mallikarjunan, S., and Goyal, A. (2011). Extended kalman filter vs. error state kalman filter for aircraft attitude estimation. *AIAA Guidance, Navigation, and Control Conference*.

Marin, M. and Bang, H. (2020). Design and simulation of a high-speed star tracker for direct optical feedback control in adcs. *Sensors (Switzerland)*, 20.

Markley, F. L. and Crassidis, J. L. (2014). *Fundamentals of Spacecraft Attitude Determination and Control*. Springer, Space Technology Library.

McAdams, J. V., Dunham, D., Mosher, E., Ray, J., Antreasian, P. G., Helfrich, C. E., and Miller, J. K. (2000). Maneuver history for the near mission: Launch through eros orbit insertion. *Astrodynamics Specialist Conference*, pages 351–366.

Michel, P., Froeschle, C., and Farinella, P. (1996). Dynamical evolution of two near-earth asteroids to be explored by spacecraft: (433) eros and (4660) nereus. *Astronomy and Astrophysics*, 313(3):993–1007.

Miller, J. K., Konopliv, A. S., Antreasian, P. G., Bordi, J. J., Chesley, S., Helfrich, C. E., Owen, W. M., Wang, T. C., Williams, B. G., and Yeoman, D. K. (2002). Determination of shape, gravity, and rotational stateof asteroid 433 eros. *Icarus*, 155:3–17.

Miller, P. A., Farrell, J. A., Zhao, Y., and Djapic, V. (2010). Autonomous underwater vehicle navigation. *IEEE Journal of Oceanic Engineering*, 35:663–678.

Montenbruck, O. and Gill, E. (2000). *Satellite Orbits : models, methods, applications*. Springer, Oberpfaffenhofen.

Mudgway, D. J. (2013). *Uplink-Downlink: A History of the Deep Space Network, 1957-1997 (The NASA History Series)*. CreateSpace Independent Publishing Platform.

Nesnas, I. A., Hockman, B. J., Bandopadhyay, S., Morrell, B. J., Lubey, D. P., Villa, J., Bayard, D. S., Osmundson, A., Jarvis, B., Bersani, M., and Bhaskaran, S. (2021). Autonomous exploration of small bodies toward greater autonomy for deep space missions. *Frontiers in Robotics and AI*, 8:270.

Opromolla, R. and Nocerino, A. (2019). Uncooperative spacecraft relative navigation with lidar-based unscented kalman filter. *IEEE Access*, 7:180012–180026.

Pineau, J. P., Parker, J. W., Steffl, A. J., Schindhelm, E., Medina, R., Stern, S. A., Birath, E. M., and Versteeg, M. (2019). Flight operations and lessons learned of the rosetta aliceultraviolet spectrograph. *Journal Of Spacecraft and Rockets*, 56:3.

Poulose, A., Eyobu, O. S., and Han, D. S. (2019). An indoor position-estimation algorithm using smartphone imu sensor data. *IEEE Access*, 7:11165–11177.

Rawashdeh, S. A. and James E. Lumpp, J. (2012). A stellar gyroscope for small satellite attitude determination. *Small Satellite Conference*.

Razgus, B. (2016). Relative navigation in asteroid missions dual quaternion approach",. *TU Delft Msc Thesis, TU Delft Repository, Netherlands.*

Sadeghzadeh-Nokhodberiz, N. and Poshtan, J. (2016). Loosely coupled fusion of camera and inertial sensors for distributed error compensation in strapdown inertial navigation system. *Transactions of the Institute of Measurement and Control*, 38:1283–1297.

Santo, A., Kee, S. C., and Gold, R. E. (1995). Near spacecraft and instrumentation. *Journal of Astronautical Sciences*, 43:373–398.

Sensors, A. and Power AG, S. S. (2021). Dmu41 high performance inertial measurement unit.

Serio, G. F., Astronomico, O., Brera, D., and Sicoli, P. (2002). Asteroids iii, giuseppe piazzi and the discovery of ceres a. manara. *University of Arizona Press*, pages 17–24.

Sheikh, S., Hanson, J., Collins, J., and Graven, P. (2009). Deep space navigation augmentation using variable celestial x-ray sources. *Proceedings of the Institute of Navigation, National Technical Meeting*, 1:34–48.

Siddiqi, A. A. (2018). *Beyond Earth: A Chronicle of Deep Space Exploration.* National Aeronautics and Space Administration, Washington.

Spee, S. (2022). Asteroid gravity field estimation below the brillouin sphere. *TU Delft Msc Thesis, TU Delft Repository, Netherlands.*

St-Pierre, M. and Gingras, D. (2004). Comparison between the unscented kalman filter and the extended kalman filter for the position estimation module of an integrated navigation information system. *IEEE Intelligent Vehicles Symposium, Proceedings*, pages 831–835.

Strikwerda, T. E., Ray, J. C., and Haley, D. R. (1998). The near guidance and control system. *John Hopkins APL Technical Digest*, 19 (2).

Systems, L. C. M. S. (2014). Product datasheet the 3dm-gx3-15 miniature inertial measurement unit and vertical gyro.

Takahashi, S. and Scheeres, D. (2022). Autonomous proximity operations at small neas. *Conference: 33rd International Symposium on Space Technology and Science (ISTS).*

Thienel, J. and Sanner, R. M. (2003). A coupled nonlinear spacecraft attitude controller and observer with an unknown constant gyro bias and gyro noise. *IEEE Transactions on Automatic Control*, 48:2011–2014.

Thomas, P., Joseph, J., Carcich, B., Veverka, J., Clark, B., Bell, J., Byrd, A., Chomko, R., Robinson, M., Murchie, S., Prockter, L., Cheng, A., Izenberg, N., Malin, M., Chapman, C., McFadden, L., Kirk, R., Gaffey, M., and Lucey, P. (2002). Eros: Shape, topography, and slope processes. *Icarus*, 155, issue 1:18–37.

Tsuno, K., Okumura, E., Katsuyama, Y., Yuasa, H., and Nakayama, M. (2006). Lidar on board asteroid explorer hayabusa. *ICSO 2006.*

Urrea, C. and Agramonte, R. (2021). Kalman filter: Historical overview and review of its use in robotics 60 years after its creation. *Journal of Sensors*, 2021:9674015.

van Leeuwen, F. (2007). *Hipparcos, the new reduction of the raw data.* Springer, New York.

Vermeulen, J. G. P. (2022). Identification of near-earth asteroids using multi-spacecraft systems. *TU Delft Msc Thesis, TU Delft Repository, Netherlands.*

Wakker, K. F. (2015). *Fundamentals of Astrodynamics.* Institutional Repository Library, Delft University of Technology, Delft.

Werner, R. and Scheeres, D. (1997). Exterior gravitation of a polyhedron derived and compared with harmonic and mascon gravitation representations of asteroid 4769 castalia. *Celestial Mechanics and Dynamical Astronomy*, page 313–344.

Werner, R. A. and Scheeres, D. (1996). Exterior gravitation of a polyhedron derived and compared with harmonic and mascon gravitation representations of asteroid 4769 castalia. *Celestial Mechanics and Dynamical Astronomy*, 65:313–344.

Wie, B. (2008). *Space Vehicle Dynamics and Control*. American Institute of Aeronautics and Astronautics, Inc, ProQuest Ebook Central.

Williams, B. (2002). Technical challenges and results for navigation of near shoemaker. *Johns Hopkins APL Technical Digest*, 23(1):34–45.

Woicke, S. (2018). Hazard relative navigation towards safe autonomous landings in unknown hazardous terrain. *TU Delft Msc Thesis, TU Delft Repository, Netherlands.*

Yang, S. and Li, H. (2016). Application of ekf and ukf in target tracking problem. *2016 8th International Conference on Intelligent Human-Machine Systems and Cybernetics.*

Yang, Y. (2012). Spacecraft attitude determination and control: Quaternion based method. *Annual Reviews in Control*, 36:198–219.

Zhou, Z. and Colgren, R. (2005). A non-linear spacecraft attitude tracking controller for large non-constant rate commands. *International Journal of Control*, 78(5):311–325.